UNIVERSITÀ
DEGLI STUDI
DI BRESCIA

DOTTORATO DI RICERCA IN INGEGNERIA MECCANICA E INDUSTRIALE

settore scientifico disciplinare: ING-IND21 (Metallurgy)

CICLO: XXXVI

TITOLO di TESI

Experimental material compatibility analysis for innovative CO_2 blends to be adopted as working fluid in high-efficiency CSP Power Plants

DOTTORANDA
Lorenza Putelli
Matricola: 706476

Relatori
Prof. Iora Paolo Giulio – UniBS
Prof. Gelfi Marcello Giuseppe - UniBS

Correlatore
Prof. Di Marcoberardino Gioele – UniBS

Anno Accademico 2023-2024

INDEX

ABSTRACT (ITALIAN LANGUAGE)

La presente tesi si inserisce nell'ambito della transizione energetica, con un focus specifico sulle energie rinnovabili e in particolare sull'energia solare utilizzata nella tecnologia Concentrated Solar Power (CSP). Nonostante i significativi progressi compiuti nel perfezionamento dei CSP (minor complessità delle turbomacchine e miglioramento dell'efficienza), il costo dell'elettricità prodotta rimane ancora un ostacolo alla competitività sul mercato. Un approccio innovativo per abbattere i costi coinvolge l'uso di miscele di anidride carbonica supercritica (sCO_2) come fluido di lavoro, in luogo dei più tradizionali vapor d'acqua o anidride carbonica supercritica pura.

La ricerca si propone di affrontare le sfide legate alla compatibilità dei materiali metallici, come le leghe di Fe e Ni, con le miscele di CO_2, concentrandosi sulla loro resistenza a corrosione ad alta temperatura; un ulteriore obiettivo è quello di esplorare nuovi dopanti da mescolare con la CO_2 per ottenere miscele efficienti e termicamente stabili.

È bene ricordare che, sebbene la corrosione in presenza di sCO_2 ad alta temperatura sia ampiamente discussa in letteratura, le ricerche specifiche sulle miscele di sCO_2 sono ancora limitate.

Nel corso dello studio, attraverso l'utilizzo del software Aspen Plus, è stata effettuata un'analisi preliminare dell'efficienza di diverse miscele di CO_2, contenenti dopanti come C_6F_6, C_4F_{10}, $TiCl_4$, $SiCl_4$, SO_2 e Novec4710, per valutarne la possibile applicabilità come fluidi di lavoro nei cicli di potenza.

L'apparato sperimentale per le prove di corrosione a caldo è stato perfezionato nel corso del tempo e la sua versione finale è consistita in un recipiente in pressione realizzato in Inconel 625 flangiato (e quindi smontabile), che ha permesso di rimuovere periodicamente i campioni e misurare lo stato di avanzamento della corrosione, permettendo così, di valutare le cinetiche di corrosione dei diversi materiali testati in contatto con le miscele di sCO_2. La procedura di prova è consistita nel riempimento del vessel con la miscela di sCO_2 e l'inserimento di un'asta di allumina su cui sono stati inseriti dischetti forati realizzati con i diversi materiali oggetto d'analisi. Tra i dischetti sono stati interposti distanziali anch'essi in allumina allo scopo di prevenire interazioni indesiderate tra i materiali testati. L'intero sistema è stato poi sottoposto a riscaldamento mediante l'uso di un forno a muffola.

Questo approccio ha consentito lo studio della stabilità termica del fluido e in particolare della corrosione ad alta temperatura dei materiali. Le temperature selezionate per queste analisi sono state scelte per identificare i materiali più idonei destinati a diverse parti dell'impianto CSP pilota, che possono variare da un minimo di 120°C (es. pompa) a un massimo di 550°C (es. ingresso turbina).

La caratterizzazione degli strati di ossido formati sulla superficie dei campioni è stata realizzata utilizzando diverse tecniche di analisi tra cui la microscopia ottica e la microscopia elettronica (SEM-EDS). Per le miscele contenenti $SiCl_4$ e SO_2, sono stati identificati materiali e rivestimenti caratterizzati da una buona resistenza a corrosione dopo un test di 2000 ore.

Infine, è importante ricordare che questa ricerca è inclusa nei progetti europei H2020 Scarabeus e Desolination e che i risultati ottenuti hanno dato un contributo notevole alla comprensione dei meccanismi di corrosione che avvengono nelle miscele di sCO_2 e alla scelta dei migliori materiali utilizzabili nella nuova tecnologia CSP.

INTRODUCTION

This thesis delves into the critical imperative of sustainable energy solutions in the face of the escalating global climate crisis. It centers on the pressing need for an energy transition, a shift from fossil-fuel-based systems to low-carbon alternatives, as a pivotal response to the profound environmental concerns associated with climate change [1-2]. The primary objective of the energy transition is clear: substantially reduce CO_2 and greenhouse gas emissions associated with energy production and consumption. This goes beyond merely substituting fossil fuels with low-carbon alternatives; it entails a comprehensive approach that involves improving energy efficiency across various sectors. While the environmental imperative is the driving force behind the energy transition, the associated benefits extend beyond that realm. The adoption of cleaner energy sources brings about positive outcomes such as reduced air pollution, improved public health, enhanced energy security, and job creation [3-5]. Moreover, it fosters innovation and economic growth by opening up new markets and opportunities in renewable energy technology development. However, this transition is not without its challenges. Existing energy infrastructure, dominated by fossil fuel-based technologies, poses obstacles to the widespread integration of renewable energy sources. Complex issues, including technological limitations, intermittency of certain renewable sources, and the need for large-scale energy storage solutions, must be addressed [6]. Within the myriad facets constituting the energy transition [7-13], renewable energies play a pivotal role. This thesis is inherently situated within this broader context, focusing specifically on the realm of solar energy. The annual average of direct horizontal radiation is around 170 W/m^2, yielding a yearly integrated value of 5.4 GJ, equivalent to the energy content of one barrel of oil, 200 kg of coal, or 140 cubic meters of natural gas. The exploration of global energy consumption reveals that in 2023, the world's total energy consumption reached almost 14500 million tons of oil equivalent (MTOE), translating to a continuous power demand of 19.25 terawatts (TW). Interestingly, this colossal power requirement could theoretically be supplied by a mere 1.4% of the Great Saharan Desert [14-17]. This underlines the potential of renewable resources to play a pivotal role in addressing the energy challenges faced by the world. As early as 1994, Sheer recognized the potential of solar technology, underlining its significance in the evolving landscape of sustainable energy solutions [18-19]. Since that time, solar technology has become a pervasive force across a spectrum of applications, among which Concentrated Solar Power (CSP) stands out prominently. This technology dates back to the late 20th century and holds promise in addressing the energy crisis due to its clean, reliable, and environmentally friendly power. CSP systems utilize mirrors or lenses to concentrate sunlight and generate heat, applicable for various purposes, including electricity generation and diverse industrial applications ranging from water desalination to mineral processing. A CSP system is illustrated in the Figure 1 [20-22]:

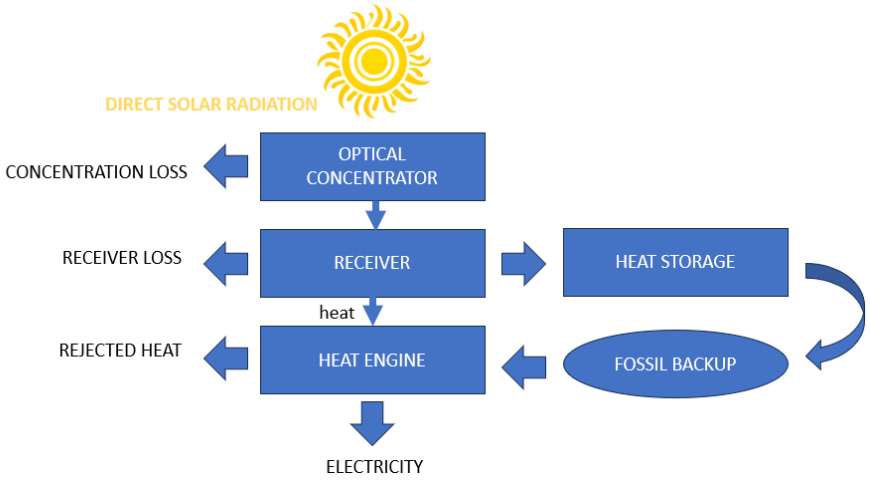

Figure 1 – General flow diagram of CSP plant

The International Energy Agency (IEA) recently released a report on Concentrated Solar Power (CSP), outlining key findings and projections. By 2050, with adequate government support, CSP has the potential to contribute 11.3% of global electricity demand, with 9.6% from solar energy and 1.7% from backup fossil or biomass fuels. North America is projected to be the largest producer and consumer of CSP electricity, followed by Africa, India, and the Middle East. Northern Africa, with high solar irradiance, could become a significant electricity exporter to Europe [23]. The global concentrating solar thermal power capacity, by country, is shown in Figure 2:

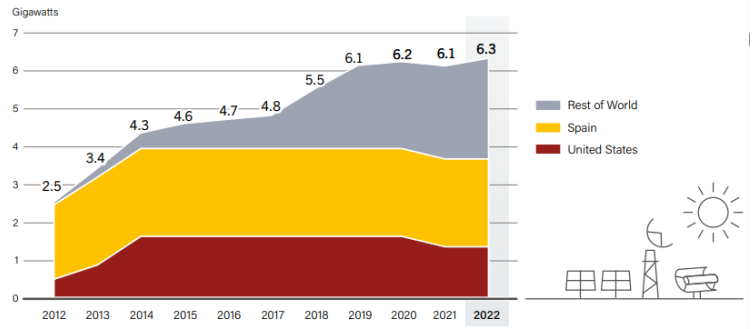

Figure 2 - Concentrating Solar Thermal Power Global Capacity, by Country and Region, 2012-2022 [24]

Especially since 2015, the global Concentrated Solar Power (CSP) market has encountered challenges, including land use and habitat loss, potential use of harmful materials, noise pollution affecting wildlife, regulatory changes, project failures, and competition from solar photovoltaic technology [24]. CSP expansion in hot arid areas faces obstacles such as the need for cooling water, distance from consumption centers impacting technical and economic considerations. Key concerns encompass also heat transfer fluids (HTF), energy storage (ES) technologies, water management, and high Levelized Cost of Electricity (LCOE) [25-27]. To address these environmental concerns, the Sustainable Development Goals (SDGs) framework encourages environmentally friendly renewable energy development. It emphasizes responsible land use, water-saving practices, reduction of harmful substance usage, and mitigation of noise pollution. Moreover, ongoing research and development efforts explore novel designs, materials, and enhanced efficiency, aiming to make CSP plants more economically viable and competitive in the realm of renewable energy solutions. In the context of advancing Concentrated Solar Power (CSP) technology, the thesis aims to address some of the previously mentioned challenges: reducing the Levelized Cost of Electricity (LCOE) and enhancing cycle efficiency.

Even for an IRENA report, significant cost reductions of 30-35% in CSP technology are projected by 2025 due to ongoing technological advancements. The driving force behind this reduction is the higher operational temperature, which contributes to increased overall efficiency, resulting in a smaller solar field footprint, reduced primary energy demand, and subsequently lowered capital costs (typically comprising about 40% of the total). Additionally, the implementation of higher operating temperatures enables a greater temperature differential across the thermal energy storage system. This translates to reduced heat transfer fluid requirements, predominantly molten salts, and smaller storage tank sizes, leading to a decreased plant footprint. Given that the cost of the storage system accounts for approximately 10-15% of the total plant cost, harnessing these elevated temperatures could lead to a considerable reduction in these associated expenses. Furthermore, the potential integration of supercritical cycles, alongside the utilization of higher operating temperatures, stands to enhance the overall cost-saving potential within the realm of concentrated solar power technology [28].

In the ambit of renewable energy, another method of harnessing solar energy is through photovoltaics (PV). Both technologies share the goal of reducing carbon emissions and addressing energy challenges, but they do so through distinct mechanisms. PV technology operates by directly converting sunlight into electricity

using semiconductor materials. In contrast, as previously mentioned, CSP technology involves focusing sunlight onto a receiver to generate high temperature working fluids that operate into a power block [29].

Energy storage is different as well. PV systems often require additional battery storage solutions to provide electricity during periods of low sunlight. On the other hand, CSP systems often come equipped with built-in thermal energy storage systems (TES), enabling the continuous generation of electricity even when the energy from sun is not available. This aspect significantly enhances CSP's reliability and flexibility. Moreover, CSP's efficiency is higher due to concentrated sunlight generating elevated temperatures. This makes it adapt for large-scale power generation, delivering more energy per sunlight unit compared to PV [29-30].

In terms of cost, photovoltaic (PV) systems have the advantage of lower installation costs and scalability. However, they do incur additional expenses for energy storage. Concentrated Solar Power (CSP) systems, on the other hand, have higher initial costs due to complex components, but they often include integrated thermal storage, which can eliminate the need for costly energy storage solutions [31]. Based on these considerations, CSP excels for several reasons. It ensures continuous power allowing for consistent power generation day and night and addressing sunlight's intermittence. Its efficiency suits larger energy production.

Therefore, as PV technology dominates daylight hours, CSP has the capability to supply solar energy before sunrise, after sunset, and even throughout the night. This unique capability, positions PV and CSP not as rivals but as counterparts that complement each other. In fact, CSP could be utilized to provide uninterrupted electricity from late afternoon to mid-morning, allowing PV to cover the remaining time. This arrangement is already in practice at the Mohammed bin Rashid Al Maktoum Solar Park operated by the Dubai Electricity and Water Authority [32].

The CSP System comprises three main components (as shown in the Figure 3):

- Solar Field: This part transforms sunlight into heat energy.
- Heat Storage: It stores thermal energy by utilizing molten salt as a medium for heat storage.
- Power Block: This unit produces electricity by utilizing a steam turbine, with the steam generated by harnessing solar energy.

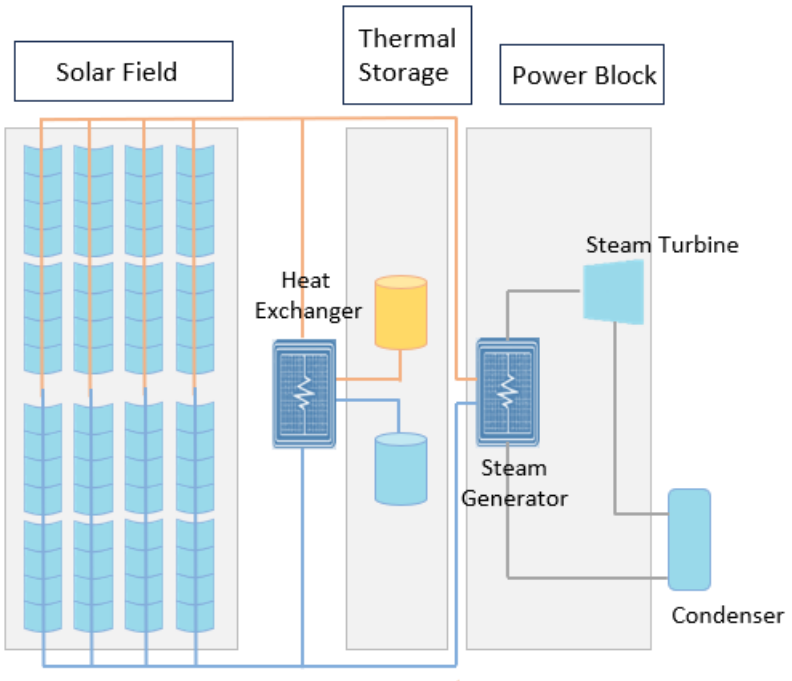

Figure 3 – CSP main components

The solar field uses four types of concentrating systems: Parabolic Trough, Linear Fresnel, Solar Tower, and Parabolic Dish Systems, each offer distinct advantages and have seen deployment worldwide [21].

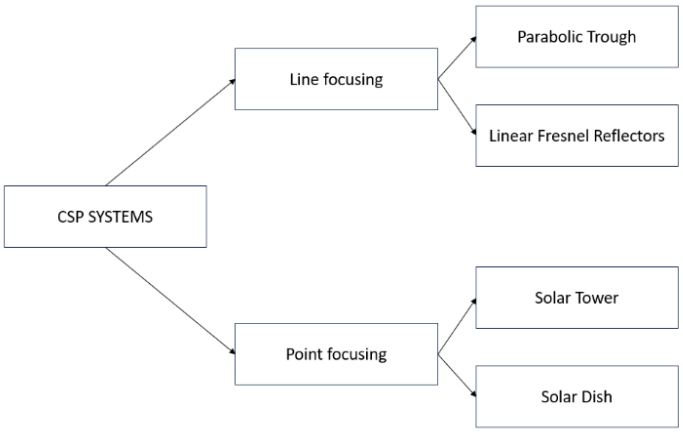

Figure 4 – Classification of CSP systems

Table 1 summarizes technology descriptions, yearly efficiency, operating temperature range, and costs [21]:

Technology	Short description	Electricity efficiency	Storage	Temperature (°C)	Cost ($/W)
Parabolic trough	Long curved mirror. Parabolic sheet of reflective material	12-15%	Molten salt	300-550	4.0-2.7
Linear Fresnel	Flat mirror instead of curved mirror in parabolic trough	8-10%	Storage has not been perfected	250-500	2.2
Parabolic dish	Parabolic mirror is used to focus heat directly on a Stirling engine	20-30%	Does not accommodate thermal storage	400-1500	12.6-1.3
Solar tower	It contains large heliostat field with tall tower in its center	20-30%	Molten salt	300-1000	4.4-2.5

Table 1 – Technological comparison

Among these, the noteworthy technology is the solar tower system, which will be considered in the thesis. In particular, this system utilizes heliostats, which are mirrors that track the sun and direct its energy to a receiver at the top of a tower. The first modern power tower, Solar One, was commissioned in 1982 in California, USA. It had a capacity of 10 MW and used steam as the heat transfer fluid [33].

The heat storage system plays a crucial role in the CSP system by allowing it to manage high-demand periods and counter the challenges posed by unpredictable weather patterns. When there's ample direct sunlight, the extra heated fluids can be stored in a hot tank. Then, during times of reduced sunlight, these stored fluids can be released to prevent system shutdown and maintain a steady power output. On the other hand, the power block's primary function is to convert thermal energy into electricity. The heated fluid from the heat storage system warms up the circulating fluid in the power block. This, in turn, stimulates the turbine generators to produce electricity [34].

Storage is key to addressing solar intermittency and boosting CSP plant efficiency [35]. Extensive research reviews storage technologies for CSP, emphasizing high energy density, stable medium properties, low heat loss, eco-friendliness, and cost-effectiveness [36]. Mao examines CSP thermal storage design [37]. Gil et al. detail advanced high-temperature thermal storage, covering concepts, materials, models, and real cases enhancing reliability and profits [38-39]. Mohan et al. review sensible energy storage for CSP above 600°C [40]. Alva et al. comprehensively explore CSP with Parabolic Trough Collectors (PTCs), discussing theoretical frameworks, concentration ratios, Heat Transfer Fluid (HTF) progress, thermal enhancement methods,

receiver control, and commercial PTC-based CSP plants. Storage's role in overcoming intermittency and boosting CSP efficiency is highlighted [41].

The power block within a Concentrated Solar Power (CSP) plant plays a crucial role in converting thermal energy into electricity. By conducting in-depth assessments of power block performance, CSP technology can enhance its ability to maintain stable power generation, improve operational efficiency, and effectively optimize control strategies, especially when facing varying operational conditions. The CSP power block consists of four integral subsystems: Solar Collector System (SGS), turbines, recuperative heaters, and the cold-end condenser [42-43]. This configuration is illustrated in Figure 5 in case of typical steam plant application[44]:

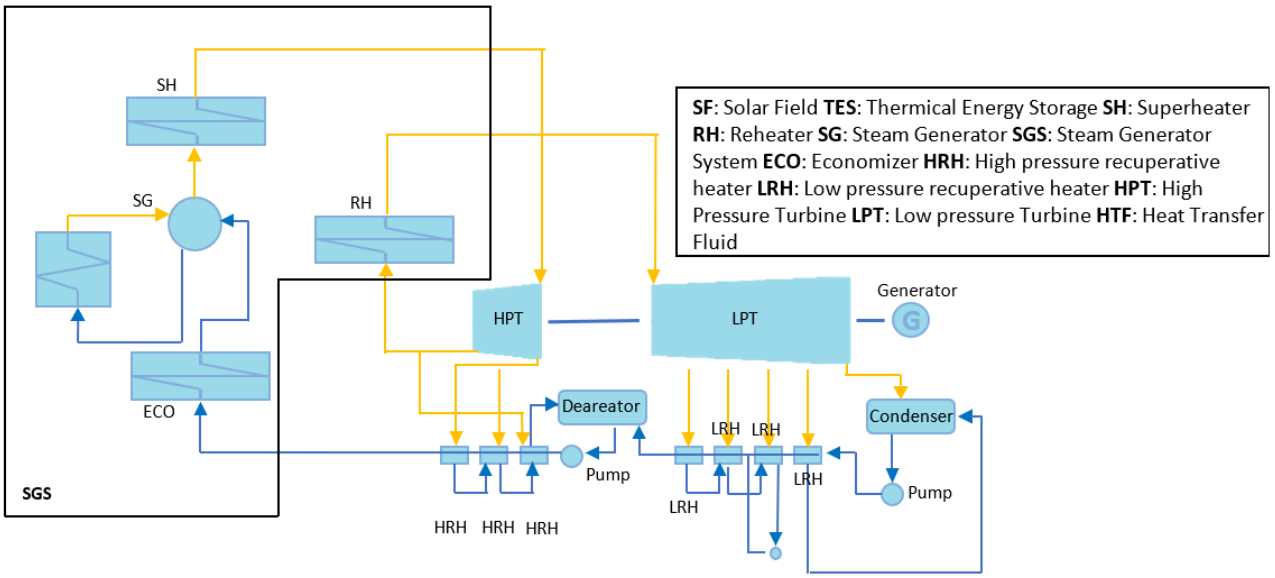

Figure 5 – Diagram of CSP

Concentrated Solar Power (CSP) systems can employ various thermodynamic cycles, including steam Rankine, organic Rankine, Stirling, simple recuperative or recompression Brayton, or combined [45-47]. There are approximately 104 operational CSP plants worldwide. Among these, steam Rankine cycles are the most prevalent, while only four demonstration Organic Rankine Cycle (ORC) plants exist. Despite the variety of cycles used, CSP plant power block efficiency typically falls in the range of 30% to 40%, which is lower than that of supercritical coal-fired power plants, exceeding 42% [42 - 48].

Improving the efficiency of CSP power blocks is a critical area for cost reduction in CSP systems. Achieving higher conversion efficiencies would significantly bolster CSP's standing within the alternative energy landscape. In a review conducted by Dunham [49], various high-efficiency thermodynamic cycles suitable for CSP systems were assessed. The choice of the most suitable thermodynamic cycle depends on the operating temperature. For lower temperatures, steam Rankine systems appear to offer superior thermal efficiencies. However, their effectiveness is constrained by the current capabilities of steam components, which are generally limited to around 600°C. Beyond this temperature limit, the CO_2 recompression Brayton cycle emerges as a robust contender for achieving higher efficiency in CSP systems.

Considering these factors, it's not surprising that the most common approach for operational concentrated solar power plants worldwide involves using a traditional steam cycle (SC) to turn heat into electricity. However, in this plant setup, the properties of water, such as its high critical pressure and temperature, along with its relatively low molecular weight require the use of large-scale turbomachinery with many stages. This, in turn, results in significant upfront investment cost [50].

In recent times, a groundbreaking advancement known as supercritical CO_2 (sCO_2) technology has emerged in the realm of Concentrated Solar Power (CSP). This innovation holds the promise of significantly reducing the costs associated with generating solar thermal electricity. One of the key advantages of sCO_2 technology lies in the simplified design of turbomachinery. It necessitates fewer stages and smaller diameters compared to traditional systems. Additionally, this technology requires only a single primary heat exchanger, as opposed to the multiple heat exchangers required in conventional steam cycles. This streamlined design not only reduces complexity but also enhances the potential for cost reduction.

So, over the past two decades, there has been a growing interest in utilizing supercritical CO_2 (sCO_2) as a working fluid due to its favorable properties, including high thermal efficiency at medium to high temperatures and minimal environmental impact as well. For these benefits, several power plants using sCO_2 technology have been built to prove the concept's feasibility. These facilities primarily follow the Simple Recuperative [Figure 6] and Recompression [Figure 7] cycle designs, as indicated in the Table 2 listing the main sCO_2 facilities currently in operation or under construction:

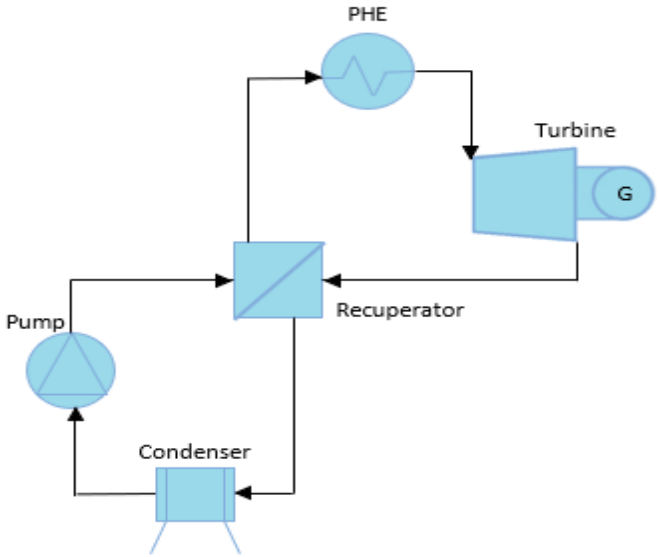

Figure 6 – Component schematic of Simple Recuperative (SR) power cycle

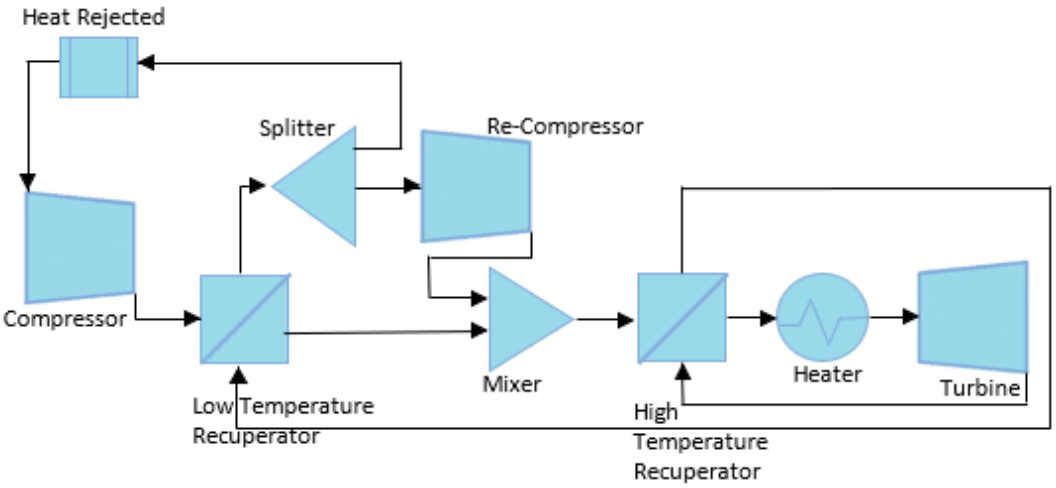

Figure 7 - Component schematic of the recompression cycle

Site of Constuction	Size	Power Cycle	Institute/Project
Posadas, Spain	2 MW	Simple Recuperated	EU funded H2020 SOLARSCO2OL [51]
Daejeon, South Korea	4.5 KWe	Simple Recuperated	Korea Institute of Energy Research Institute (KIER) [52]
Daejeon, South Korea	10 KW	Simple Recuperated	Korea Institute of Energy Research Institute (KIER) [52]
San Antonio, Texas	10MWe	Simple Recuperated	Southwest Research Institute (SwRI), Gas Technology Institute, and General Electric [53]
Daejeon, South Korea	120 KWe	Dual Bryton	Korea Institute of Energy Research Institute (KIER) [52]
San Antonio, Texas	1 MWe	Recompression	Southwest Research Institute (SwRI) [54]
Albuquerque, New Mexico, USA	1 MWe	Recompression	Sandia National Laboratories (SNL) [55]

Table 2 - Worldwide supercritical carbon dioxide facilities, operational or under construction

It's worth noting, however, that the use of pure sCO_2 as a working fluid is not always advantageous, particularly in Concentrated Solar Power (CSP) applications. Unfortunately, with the exception of a few installations in favourable locations, the levelized cost of electricity (LCoE) for this technology is currently around €150/MWh, well above the target of €100/MWh. In addition, in sunny regions, CSP faces the challenge of high ambient temperatures; in fact, when the ambient temperature approaches or exceeds the critical temperature of CO2 (31°C), a sCO_2 condensing cycle, which is associated with a 10% increase in efficiency compared to a non-condensing cycle, cannot be used. To overcome these challenges, several studies propose to increase the critical temperature of CO_2 by using specific additives. [50 and 56-60].

The idea of using combinations of CO_2 with other substances has been previously explored for nuclear, fossil fuel, concentrating solar power, shipboard propulsion, shipboard house power, geothermal, waste heat recovery (WHR), and biomass applications.

One notable research in this area was conducted by Sandia National Labs in the United States [50]. They found that introducing a portion of butane to the working fluid raises its critical temperature, consequently enhancing cycle efficiency. Conversely, adding SF_6 has the opposite effect, lowering the critical temperature.

In the realm of Waste Heat Recovery (WHR), Ayub et al. [61] introduced the concept of employing CO_2-based blends as operational fluids within closed Brayton power systems. These systems would harness the heat from gases with relatively elevated temperatures (400-450 °C) as a source of waste heat. The substances explored as potential additives included R-134a, Novec649, and Novec5110. According to the authors, choosing CO_2 mixtures stands out as the preferred option. This preference is primarily driven by the potential to attain increased cycle efficiency through a simplified cycle design. Moreover, these mixtures offer the advantage of operating at lower maximum pressures compared to pure sCO_2 cycles.

Haroon et al. [62] employed a CO_2 + toluene blend as the operational fluid in power cycles engineered to recover heat from the exhaust gases of medium-scale gas turbines. The results showcased a substantial growth in thermodynamic efficiency when utilizing CO_2 + toluene in contrast to an sCO_2 Brayton cycle.

Liu et al. [63] made a comprehensive thermodynamic assessment of power cycles employing five distinct CO_2-based mixtures (CO_2-cyclohexane, CO_2-propane, CO_2-butane, CO_2-isobutane, and CO_2-H_2S) as operational fluids in a recompression Brayton cycle. The study highlights the advantages of deploying CO_2 mixtures over the traditional sCO_2 Brayton cycle but omits an evaluation of the thermochemical stability of the selected pure compounds and mixtures.

Guo et al. [64] through a comprehensive analysis about three distinct mixtures and four cycle configurations, determined that a combination involving a CO_2-Xenon mixture offers better performances compared to pure sCO_2 power cycles.

Shu et al. [65] singled out CO_2/R32 as the most suitable working fluid, owing to its capacity to operate at lower pressures while delivering higher power output compared to pure CO_2.

Vesely et al. [66]-[67] explored the feasibility of employing noble or inert gases as dopants in CO_2 systems, while Baik et al. [68] considered the utilization of CO_2 mixtures with refrigerants. The former approach

facilitated operation at extremely high temperatures, albeit with only marginal efficiency gains, whereas the latter solution demonstrated a notable improvement in cycle performance but encountered stability issues beyond the temperature range of 250 - 300°C.

Manzolini et al. [69] identified the CO_2-N_2O_4 and CO_2-$TiCl_4$ mixture as an effective fluid for integration with CO_2, demonstrating their potential to achieve high power cycle efficiency (up to 50% for CO_2-$TiCl_4$ and 49% for CO_2-N_2O_4), to enable a simpler regenerative cycle design, reducing plant complexity and lowering specific energy production costs by around 50% compared to traditional steam cycles, to increase yearly electricity production and to lower the Levelized Cost of Electricity (LCOE) in solar tower plants through rigorous thermodynamic analysis.

Recently, the CO_2+C_6F_6 (hexafluorobenzene) mixture appeared to be a promising operational fluid in transcritical power cycles owing to its god thermal stability and thermodynamic efficiency, even within a recuperative cycle [70].

Furthermore, Morosini et al. [71] delved into the adoption of the CO_2+SO_2 blend as an innovative working fluid in a transcritical power cycle featuring a minimum cycle temperature of 51°C. Their findings underscored a heightened cycle efficiency in a recompressed configuration when compared to recompressed sCO_2 cycles, along with a lower LCOE.

In general, the right selection of CO_2 blend mixtures yields advantages over both traditional steam cycles and standard sCO_2 cycles. These advantages include increased efficiency, simplified power block design more compact turbomachinery and a reduction in the overall costs of the plants.

Evaluating Chemical Compatibility for Materials and Innovative Blends in Power Plants

Apart from investigating the mixtures, it is crucial to address the chemical compatibility of these blends with the materials intended for constructing the power plant as they are typically expected to remain operative for 20 years or more [72].

Consequently, the primary aim of this research is to determine whether certain materials recommended for use in pure CO_2 environments or environments containing CO_2 with impurities remain suitable in various CO_2 blends and evaluate their corrosion.

Corrosion is the result of a metal's interaction with its surroundings, leading to changes in the metal's properties and potentially harming its functionality or the environment. Corrosion can manifest in various ways, ranging from minor surface imperfections on metals to the complete breakdown (ISO 8044: 2010 [73]). There are two primary corrosion mechanisms:

- **Dry Corrosion**: dry corrosion occurs in the absence of moisture or water. Common referred to as oxidation, is a corrosion process characterized by the chemical interaction between a material and a gases in a dry environment. This phenomenon leads to the creation of an oxide layer on the material's surface as a consequence of the oxidation reaction. This process is typically expedited by high temperatures.
- **Wet Corrosion**: wet corrosion occurs when visible water layers or water pockets form on metal surfaces due to factors like rain, sea spray, or dew. In other words, it involves the presence of liquid. This type of corrosion commonly occurs at room temperature. Even when the flat surfaces of a metal component appear dry, wet corrosion can occur in crevices or condensation traps. The solubility of corrosion products can affect the corrosion rate during wet corrosion. When corrosion products are soluble, they increase the conductivity of the electrolyte, leading to an accelerated corrosion rate [74].

There are several methods for evaluating corrosion. From the literature related to the study of sCO_2, a variety of techniques and parameters are utilized by researchers to obtain a comprehensive understanding of the phenomena:

- **Corrosion Rate Analysis**: it is a crucial parameter and is often measured by using gravimetric methods. The weight change method is typically used due to the ease with which corrosion products can detach in sCO_2 environments. The corrosion rate (V_c) is calculated by using the formula:

$$Vc = \frac{(87600\,\Delta m)}{(\rho \times A \times T)}$$

where Δm is the weight loss, ρ is the density of the specimen, A is the specimen's area and T is the corrosion time [75].

- **Local Corrosion Rate:** studies in sCO_2 environments primarily focus on pitting corrosion. Teeter examined specific corrosion sites using a ZeScope high-resolution white light interferometer. The depth of localized corrosion pits could be determined by scanning the sample's surface with a microscope and generating a 3D representation. This process was carried out on 12-20 randomly chosen sites per sample to calculate an average pit depth [76].
- **Electrochemical Evaluation**: it involves measuring physical quantities such as corrosion current and corrosion potential. A lower corrosion potential and a higher corrosion current indicate more severe material corrosion [77].
- **Structure Analysis of Corrosion Products**: various techniques, like scanning electron microscopy (SEM), X-ray diffraction (XRD), Raman spectroscopy, infrared spectroscopy (IR), transmission electron microscopy (TEM), and Mossbauer spectroscopy, are employed to study the composition and structure of corrosion products.

Firstly, it's crucial to gain a clear understanding of how alloys corrode in high-temperature and high-pressure sCO_2 (supercritical carbon dioxide) environments. Several studies have already explored this corrosion mechanism, primarily delving into the processes of corrosion reactions involving metallic materials and the composition of corrosion products formed on different metals. These studies also compare the corrosion resistance of various metallic materials within sCO_2 environments. Two main processes occur in high temperature sCO_2: oxidation and carburization.

- **Oxidation**: carbon dioxide (CO_2) generates an oxygen partial pressure that is sufficient to induce oxidation in alloying elements like iron (Fe) and chromium (Cr). This leads to oxidation reactions represented by the equations:

$$xM + yCO_2 \rightarrow M_xO_y + yCO$$

$$xM + \frac{y}{2}CO_2 \rightarrow M_xO_y + \frac{y}{2}C$$

where, M represents alloying elements (typically Cr and Fe). The resistance to corrosion depends on the formation and accumulation of oxide layers on the material's surface. Chromium-rich oxide layers typically exhibit superior corrosion resistance compared to iron-rich oxide layers. This enhanced resistance is mainly attributed to the continuous and compact nature of the chromium-rich oxide layer, which acts as a protective barrier against further oxidation. Conversely, the fragmented and porous structure of the iron-rich layer

allows corrosive gases to penetrate and diffuse within the material, leading to additional oxidation of the underlying material.

- **Carburization**: involves two steps, and the reaction responsible for carbon generation is known as the Boudouard reaction:

$$2CO_2 \leftrightharpoons 2CO + O_2$$
$$2CO \leftrightharpoons CO_2 + C$$

Initially, carbon-containing gas penetrates the oxide layer covering alloy surfaces. Then, some of the carbon (C) combines with alloying elements to create carbide precipitates, while the remaining portion forms a carbon layer between the oxide layer and the material matrix [78]. However, this phenomenon is primarily observed at high pressures because the activity of carbon (C) is quite low in high-temperature sCO_2 and atmospheric pressure [79].

Corrosion of steel in high-temperature CO_2 was extensively researched until the 1980s, primarily in France and the USA for nuclear applications. However, these studies focused on CO_2 in its subcritical phase. Recent research has shown that the behaviour of alloys at high temperatures in the presence of CO_2 is similar in both subcritical and supercritical conditions. As a result, material recommendations for subcritical CO_2 can serve as valuable guidelines, and they are outlined below:

- Mild steel: <350°C
- F-M steel: <450°C
- Austenitic steel: <650°C
- Nickel base alloy: >650°C

The main reactions involved in the damage of metals in high-temperature environments can be summarized as follows:

$$M + CO_2 \rightarrow MO + CO$$
$$2M + CO_2 \rightarrow 2MO + C$$
$$M + CO \rightarrow MO + C$$

where M is a generic metal in the steel or alloy and C is the free carbon [80].

A noteworthy and unexpected result is the observation that carbon dioxide (CO_2) tends to be more corrosive, leading to higher oxidation rates especially in steels, when compared to pure oxygen (O_2) or air. This outcome is intriguing because CO_2 possesses a significantly lower oxygen activity, which is typically the driving force behind oxidation processes [81].

In literature three main categories of alloys are analysed in an sCO_2 environment: ferritic/martensitic steels, austenitic stainless steels, and nickel-based alloys.

For ferritic steels, a protective duplex scale is observed, and it is situated between an external nickel deposit and the internal substrate of the alloy. Both layers are typically composed of magnetite Fe_3O_4. According to various authors, the inner scale layer develops within the void created by outward metal diffusion, eventually forming the outer scale. This protective layer continues to expand until it reaches a point of breakaway characterized by a transformation in the oxide's structure, resulting in the presence of "excrescences" on an otherwise flat oxide surface [82].

Ferritic/martensitic (F-M) steels exhibited limited resistance to oxidation, resulting in the formation of thick oxide scales that tended to flake off easily. These steels are also susceptible to carburization. As previously mentioned, the combination of carburization and corrosion leads to the creation of a duplex oxide scale. This scale consists of an outer layer composed of magnetite/haematite and an inner layer of spinel oxide rich in Fe-Cr, both of approximately equal thickness. Beneath this scale, carbides rich in chromium begin to form. With increasing time and temperature, these carbides become denser and penetrate deeper into the material. The "Available Space Model" is proposed to evaluate the evolution of the oxidation and carburization phenomena. Over time, the oxide layer grows larger, and its pores gradually disappear. However, with rising temperatures, the porosities expand. It is believed that these pores facilitate the internal diffusion of carbon dioxide [83].

Austenitic stainless steels' ability to resist oxidation lies on their efficient formation of a stable chromia scale, which slows down the oxidation process. Although they rapidly form a protective chromia layer on the surface, carbides beneath the oxide layer are formed due to carburization. These carbides can vary in composition depending on the steel and can compromise corrosion resistance by blocking chromium. In addition, it has been noticed that the oxide layer in austenitic steels tends to spall, which causes the breakdown of the protective layer and speeds up the depletion of chromium, resulting in the formation of an area with significantly reduced chromium content. This oxidation spallation in austenitic steels is due to lower diffusion rates, as well as higher levels of growth stress and thermal stress during the oxidation process compared to ferritic/martensitic steels. This transformation from a protective chromia layer to a non-protective iron-rich oxide film is often named "breakaway corrosion" [84].

Nickel-based alloys demonstrate the highest corrosion resistance in sCO_2 environments, respect to ferritic/martensitic and austenitic stainless steels [78]. While chromia spallation can occur in these materials as well, in the spallation zone, new chromium-rich oxides form instead of iron-rich oxides, allowing nickel-based alloys to have the ability to self-repair, unlike austenitic steel. This self-healing capability can be explained by the nickel-based alloys' notably low iron (Fe) content and elevated chromium (Cr) content. Alternatively, it may be due to the slower diffusion rate of iron in nickel-based alloys in comparison to austenitic steels. It has been demonstrated that nickel-based alloys outperform austenitic steels in cyclic oxidation tests, particularly in high-temperature supercritical carbon dioxide environments. In these alloys the oxidation rate decreases with increasing chromium and nickel content. In high-temperature sCO_2, the primary protective corrosion product for nickel-based alloys is a layer of either chromia or alumina. For nickel-based alloys that develop chromia layers, these layers function as a protective shield, effectively halting the progression of oxidation in high-temperature CO_2 environments. Furthermore, owing to the sluggish diffusion of manganese (Mn) within the chromia layer, it results in the formation of Mn–Cr spinel oxides on the surface. These spinel oxides demonstrate a considerably slower rate of growth when contrasted with pure chromia. As a result, this preservation of chromium content significantly bolsters the corrosion resistance of nickel-based alloys [83 and 85]. The improved behaviour of nickel alloys can be evaluated by considering the effects of various elements:

- **Ni and (Fe):** the demonstrated superior oxidation resistance of nickel-based alloys and iron-nickel-based alloys can be attributed to the high nickel content, which accelerates the formation of protective chromia and prevent further thickening of the oxide layer [86]. Investigating the carburization resistance, it was observed that alloys with a higher iron content tend to have reduced performance. This phenomenon can be attributed to the lower solubility of iron when compared to nickel. Moreover, nickel-based alloys were found to offer enhanced carburization resistance by minimizing carbide precipitation [87][88].
- **Cr:** its role is very important. When the Cr content is sufficient, it reacts with oxygen to form a protective chromia layer, preventing further oxidation and carburization. For nickel-based alloys, a minimum Cr content of 14% is recommended to form a protective chromia layer [89]. However, even

with a continuous chromia layer, oxidation and carburization can still occur due to carbon penetration through the chromia, forming an amorphous layer between the matrix and chromia. Tests have shown that, despite a relatively high Cr content, spalling can occur after a certain period [89]. Therefore, for increased corrosion resistance in high-temperature sCO_2 environments, it is advisable to increase the Cr content around 22% [90].

- **Co**: to obtain a clear understanding of Co's effect, additional research is necessary. Increasing cobalt content seems to benefits carburization resistance and high-temperature properties in nickel-based alloys. However, there is limited research on the topic [91].
- **Ti**: typically forms TiO_2 when it oxidizes which usually enhances corrosion resistance. Sometimes, TiO_2 could be found on top of a chromium layer [90]. This occurs because Ti is less active than chromium and diffuses faster through the chromium layer [92].
- **Al**: typically forms alumina when it oxidizes. Al_2O_3 formation is promoted by $(Cr,Fe)_2O_3$ [90]. Alumina is more thermodynamically stable than chromia, preventing carbon from penetrating the matrix [93]. However, higher Al content can lead to internal oxidation increasing the oxidation rate. While typically considered negative, in the context of nickel-based alloys, internal oxidation can occasionally have a positive effect by improving the adhesion of scales through the filling of voids caused by vacancies [94].
- **Mo**: is added to alloys to improve corrosion resistance by preventing carbide formation between Cr and C and promoting the chromia formation. Excessive Mo can accumulate as Mo carbide, that interrupts the continuity of the chromia and harms corrosion resistance [95].
- **Si**: usually in form of silica has a dual impact on corrosion resistance. It can form a protective layer, acting as a barrier against carbon diffusion and slowing down chromia growth [90 and 96]. However, the presence of silica between the oxide layer and the matrix can impact the adhesion of the oxide layer [97], potentially leading to its detachment.
- **Mn**: when it combines with chromium, it creates protective oxides ($MnCr_2O_4$) that resist carburization, reduce C diffusion and enhance corrosion resistance [98 - 99].

There are several other factors that can influence corrosion, including:

- **Temperature**: this parameter has a key role. Several studies [100-101] have explored the impact of temperature on materials exposed to supercritical carbon dioxide (sCO_2). They have evaluated corrosion by measuring mass gain and have suggested that a lower weight gain indicates improved corrosion resistance, as there is less energy available for reactions at lower temperatures. Generally, when increasing temperature alloys experience a significant increase of weight gain, indicating worsening corrosion in sCO_2. The behaviour of materials in sCO_2 has been studied at temperatures between 550°C and 750°C, research at higher temperatures is missing. Since sCO_2 becomes more corrosive at elevated temperatures, it emphasizes the need for further investigation.
- **Pressure**: most of the literature agrees that the effect of pressure on corrosion is negligible [102-104] and does not affect carburization or tensile properties [105], however, other studies, showed that the magnitude of oxidation seems to increase with increasing pressure [106]. Only in one case, the increase in pressure is associated with a positive behavior, which is explained considering itto be responsible for the reduction of porosity in the oxide scale [107].
- **Impurities:** they are difficult to completely avoid in processes involving sCO_2 under current conditions. The effects of the main impurities are listed below. Generally, impurities are evaluated in presence of research grade (RG) or industrial grade (IG) sCO_2, with a purity level of 99,999% and 99,95% respectively.

- $\underline{H_2O}$: usually in form of water vapour, it is a common impurity easily found in sCO_2. In CO_2 it can dissolves to create carbonic acid (H_2CO_3) [108]. It creates more pathways for diffusion, its molecules easily penetrate the material and causes thickening of the oxide layer, enhancing the risk of spalling [78-109]. Moreover the

presence of water does not allow the formation of a protective scale [110]. However, other studies suggest that it doesn't have a significant effect or is responsible to a reduction in the degree of carburization by blocking the sites for carbon diffusion [111]. So, more research is needed to fully understand the effects of H_2O.

- O_2: at concentrations lower than 3%, it appears to have no noticeable effect. At higher concentrations, in general, oxygen tends to have a negative impact, as an increase in its concentration is often linked to greater mass gain, thicker oxide layers, and more aggressive corrosion [112]. However, there are also contrasting findings in literature [113]. In this case, oxygen appears to have a positive effect by enhancing the stability of chromia and inhibiting localized corrosion.

- The coexistence of the two impurities, H_2O and O_2, can lead to the volatilization of chromia, according to the following reaction [114]:

$$\frac{1}{2}Cr_2O_3 + \frac{3}{4}O_2 + H_2O \rightarrow CrO_2(OH)_2$$

Some studies indicate the presence of both impurities as a cause of increased oxidation, especially in localized forms [115]. Conversely, other studies seem to attribute a positive or a negligible effect to the combined presence of O_2 and H_2O on the oxidation of Fe-based and Ni-based alloys [113 and 116]. Regarding carburization, at high O_2 and H_2O contents, it may not occur as they appear to inhibit the decomposition of CO2 [117].

- CO: it has an adverse impact. In fact, its presence results in heightened corrosion due to an accelerated carbon diffusion rate and an increased deposition of carbon. One possible explanation for this could be the Boudouard reaction mentioned earlier [118].

- SO_2: it has mixed effects and is sensitive to slight changes in exposure conditions [90]. Small amounts (0.1%) have little impact, forming protective chromia layers [119] or a severe impact due to the formation of thicker scales consisting of non-protective oxides and sulfates [120]. A higher concentration (0.5%) improved oxidation resistance, creating a protective chromia layer and reducing chromia volatilization. However, SO_2 can also induce to sulfur-containing compounds formation, breaking down protective behavior and increasing oxidation rates [121].

- **Surface finishing**: typically, an increase in surface roughness has a positive effect as it slows down oxidation and promotes the formation of a protective Cr_2O_3 layer by facilitating the outward diffusion of reactive elements like chromium. Surface treatments, including stress-induced martensitic transformation, shot peening, and cold working, have been shown to influence corrosion resistance by increasing the density of grain boundaries or dislocations in the subsurface of the alloy, thereby improving oxidation resistance [122].
- **Welding**: the effect of welding did not undergo in-depth examination. Surprisingly, when subjected to CO_2 exposure, both the welded and unwelded samples exhibit remarkable corrosion resistance, with nearly identical mass gains and no observable signs of a Precipitate-Free Zone (PFZ). The only potential issue lies in the composition of the fusion zone, where the presence of chromium (Cr) and titanium (Ti) segregation could lead to an uneven distribution of γ' precipitates and carbides, adversely affecting mechanical properties [123]. Furthermore, the study referenced in [124] reveals very similar oxides in both base material and welding. In both scenarios described by the papers, there is minimal oxidation observed. However, a notable distinction emerges in the fusion zone, where a thinner layer of oxidation is evident. This difference can likely be attributed to the reduced density within the fusion zone that serves to impede the outward diffusion of elements such as titanium (Ti) and aluminum (Al). On the contrary, in a different study, it's worth noting that welding

could have also a significant impact. The intense heat produced during welding causes changes in the nearby microstructure. More specifically, chromium tends to move towards the grain boundaries, resulting in a noticeable decrease in chromium concentration within the surrounding material. Consequently, this leads to a compromised corrosion resistance in the area around the weld.

- **Coatings:** chromized and aluminized coatings both with and without an intermediate nickel layer, deposited on a steel substrate before the pack cementation, enhance corrosion resistance by creating protective surface layers, Cr_2O_3 and Al_2O_3, respectively. The inclusion of the nickel intermediate layer serves to inhibit the diffusion of elements between the coating and the substrate, further enhancing the protective capabilities of the coatings. In the case of chromized surface, the Cr_2O_3 scale grows on the Cr coating primary by an outward chromium diffusion. Cr becomes available through the oxidation of the nitride coating layer, following the formula: $Cr_2N + \frac{3}{2}O_2 = Cr_2O_3 + \frac{1}{2}N_2$. In the case of an aluminized surface, the corrosion resistance of the Al-Ni coating depends on the stability of the γ-phase and the thickness of the Ni-(Al) layer [125].

Based on the data collected from the literature, a table has been created that defines the upper temperature limits for various categories of metallic alloys in contact with an atmosphere of pure sCO_2. However, it's important to emphasize that the sole criterion used to establish these limits is corrosion resistance. Table 3 could represent a preliminary guideline based solely on this information, without considering other critical factors such as costs, mechanical properties, etc. Therefore, further analysis and assessments may be necessary for a definitive material selection based on specific application needs.

TEMPERATURE	GOOD MATERIALS	RECOMMENDED MATERIALS
<200°C	304SS, P91, T22	Ferritic steel
<250°C	304SS, P91	Low-cost austenitic stainless steel and ferritic steel
<350°C	Mild steel can be used	
<400°C	347SS, 310SS, 304SS, 316SS	Austenitic stainless steel. P91 just for short periods
<425°C-450°C	In presence of dry sCO2 carbon steel can be used; in presence of humid sCO2 (H2O<1000vpm) Mn-Mo-Ni steel or Cr-Mo steel is recommended	
<525°C	Cr-Mo steel can be used in dry CO2	
<550°C	347SS, 310SS	Austenitic stainless steel preferably with high Ni, Co, Cr concentration. 304, 316 for short periods
<650°C	H230, IN617, 800H, 347SS, 310SS	Austenitic Ni/Cr alloy. 347, 310 for short periods
<660°C	Austenitic steels can be used	
>650°C	H282, IN740	H230, IN617 for short periods
>660°C	Nimonic 80, PE16, Ni-based alloys can be used	

Table 3 - Recommended temperature limit of alloys in pure CO_2 [126]

In **conclusion**, it is undeniable that improving Concentrated Solar Power (CSP) technology represents a crucial step in the transition to more sustainable and efficient energy sources. Throughout this analysis, it has been observed that the ability to reach high temperatures and high efficiencies in CSP processes is fundamental for maximizing the production of clean energy. However, to achieve these goals, it is essential to use stable thermal fluids and compatible materials able of withstanding the extreme conditions to which CSP facilities are subjected.

In this context, the thesis aligns perfectly with the European Scarabeus [127] and Desolination projects [128], which aim to find high-temperature stable fluids, fluid-optimal compositions and materials compatible with these fluids.

The University of Brescia (UniBs) plays a pivotal role in these projects, particularly in identifying dopants and conducting thermal stability and material compatibility tests at high temperatures, in particular at 550 °C, which is the expected temperature for the pilot plant conceived in the Desolination project.

CHAPTER 1

MIXTURES' SELECTION AND PRELIMINARY THERMODYNAMIC ANALYSIS

As discussed in the Introduction section, in recent years there has been a growing interest in using supercritical carbon dioxide (sCO_2) as a working fluid across various applications. This upsurge in interest stems from the advantageous thermodynamic properties of sCO_2 coupled with its minimal environmental impact.

Nonetheless, it is imperative to acknowledge that the utilization of sCO_2 as a working fluid may not yield favourable economic outcomes, particularly within Concentrated Solar Power (CSP) contexts. Regrettably, except for a few installations located in favourable regions, the Levelized Cost of Electricity (LCoE) for this technology currently stands at an approximate rate of 150 €/MWh, significantly exceeding the target of 100 €/MWh.

Moreover, in regions with abundant sunlight, CSP power plants face the tough challenge of elevated ambient temperatures. Notably, when the ambient temperature closely approaches or surpasses the critical point of CO_2 at 31°C, the implementation of a sCO_2 condensing cycle, which offers a 10% increment in efficiency when compared to a non-condensing cycle, becomes unviable.

To address this challenge, a multitude of research recommend increasing the critical temperature of CO_2 through the introduction of specific dopants. These dopants, extensively documented in the scientific literature across varying temperature and environmental conditions, include R-134a [129], Novec649 [130], Novec5110 [130], toluene [131], cyclohexane [132], propane [133], butane [134], isobutane [134], H_2S [135], C_6F_6 [136], N_2O_4 [137], Xenon [138], $TiCl_4$ [139], SO_2 [140], acetone [141], ethanol [142], decane [143], decalin [144], undecane [145], mitotane [146], noble or inert gases and various refrigerants.

The main aim of this chapter is the identification of the most suitable fluids to mix with CO_2. The criteria for selecting dopants are based on specific guidelines, which include considerations for thermochemical stability, high critical temperature, melting point below ambient temperature, minimal environmental impact, non-toxicity, non-flammability, high bond energy and high molecular complexity. The process of dopant selection commenced with a comprehensive and systematic examination of relevant scientific literature and subsequently extended to include volcanic gases, considering their resistance to high temperatures. However, it is important to emphasize that those characteristics outlined earlier received meticulous consideration throughout the selection process.

Certain chemical species and structural groups were expressly excluded from the selection, owing to their failure to satisfy one or more requirements. In particular:

- Hydrocarbons and refrigerants are not thermally stable when exposed to temperatures within the ranges of 250-350°C and 300°C-400°C, respectively.
- Noble gases typically possess critical temperatures that are too low to effectively raise the critical temperature of CO_2.
- The mixture of carbon dioxide and water cannot be used due to their significant immiscibility.

- Perfluoroaromatic compounds demonstrate remarkable thermal stability, outperforming even simpler linear fluorocarbons. However, it's worth noting that the simpler linear fluorocarbons still exhibit greater thermal stability compared to their longer-chained counterparts, owing to the presence of fewer weak C-C bonds, which unfortunately leads to a lower critical temperature.

However, significant domains to be considered are Chemical Vapor Deposition (CVD) processes and plasma etching, where exceptionally thermally stable fluids are used. These processes commonly employ gases such as CF_4, SF_6, C_4F_8, Cl_2, BCl_3 and others, primary composed of fluorine or chlorine, for etching applications.

It is important to highlight that all aforementioned gases are characterized by strong molecular bonds. Given these considerations, the incorporation of fluorinated or chlorinated dopants becomes imperative for formulating a thermally stable mixture at elevated temperatures. A selection of six fluids has been made, which includes $TiCl_4$, $SiCl_4$, SO_2, C_6F_6, C_4F_{10} and Novec4710:

- $TiCl_4$, a titanium halide used in conjunction with CO_2 for fluid extraction techniques;
- $SiCl_4$, a silicon halide utilized in the production of high-quality silicon;
- SO_2, a sulfur-based compound known for its exceptional thermal stability at elevated temperatures;
- C_6F_6, a cyclic perfluorocarbon distinguished by its low toxicity and high thermal stability;
- C_4F_{10}, a linear perfluorocarbon recognized for its low toxicity and exceptional solvent capability;
- Novec4710, an insulating gas characterized by high thermal stability, comprising a mixture of propanenitrile and 2,3,3,3-tetrafluoro-2-(trifluoromethyl).

Except for Novec, these fluids have been identified within the research activities conducted under the Horizon 2020 projects Scarabeus [127] and Desolination [128]. Table 4 provides a summary of the principal characteristics of the dopants, each accompanied by its respective CAS numbers and information regarding thermodynamic and safety properties:

Name	CAS number	MW (kg/kmol)	Tcr (°C)	Pcr (bar)	NFPA 704				Thermal stability (°C)
					H	F	I	OTH	
CO_2	124-38-9	44.01	31.1	73.8	2	0	0	SA	> 700 [147]
$TiCl_4$	7550-45-0	189.68	364.9	46.6	3	0	2	W	550-700°C [148]
$SiCl_4$	10026-04-7	169.90	235	35.9	3	0	2	W	550-700°C
SO_2	7446-09-5	64.07	157.6	78.8	3	0	0	-	550-700°C [71]
C_6F_6	392-56-3	186.06	243.6	32.7	1	3	0	-	390-550°C [147]
C_4F_{10}	355-25-9	238.03	113.2	23.2	1	0	0	-	390°C
Novec4710	42532-60-5	195.04	112.9	25	3	1	0	-	390-550°C [149]

Table 4 – Parameters of candidate dopants

Among these, it's important to mention the NFPA 704, a safety labeling system used to identify the hazards of hazardous materials. This system features a label with a diamond divided into four sections or quadrants, each with an abbreviation and a specific color. The abbreviations H, F, I, and OTH stand for:

- H (Health): represented by the blue quadrant, it indicates the health hazard associated with the material, ranging from 0 (no hazard) to 4 (extreme hazard).
- F (Flammability): represented by the red quadrant, it indicates the material's fire or explosion hazard, also on a scale from 0 (no hazard) to 4 (extreme hazard).
- I (Instability): represented by the yellow quadrant, it indicates the material's chemical reactivity or instability hazard, again on a scale from 0 (no hazard) to 4 (extreme hazard).
- OTH (Other): represented by the white quadrant, it may contain additional information, such as special instructions or other relevant information about the material's hazard.

Finally, it is worth to evidence that the thermal stability values reported in the last column of Table 4are derived from investigations carried out by the research groups participating in the aforementioned Scarabeus and Desolination projects.

1.1 Working fluids and mixtures adopted in this study

In this section, the working fluids considered in this research are analyzed and discussed. An in-depth exploration of their respective characteristics and properties will be highlighted in the following.

1.1.1 SUPERCRITICAL CARBON DIOXIDE (sCO_2)

One of the most common natural fluids is carbon dioxide (Table 4). Supercritical carbon dioxide (sCO_2) refers to carbon dioxide operating above its critical point (304.13K, 7.38MPa, as detailed in Table 5). It is a colourless and odorless gas, relatively non-flammable, non-toxic and falls under the category of substances "generally regarded as safe" (GRAS). Thanks to its favorable thermodynamic properties, the interest in utilising CO_2 has experienced a significant surge, particularly in recent years. Two significant factors influence the choice of sCO_2 for a power cycle. The first factor is the enhanced cycle efficiency in power cycles using supercritical fluids when operating near the critical range of the fluid. The second factor is the critical temperature of CO_2 which is closed to ambient temperature (31°C), facilitating the use of sCO_2 power cycles with a wide range of heat sources and the operation of cycle variations that discharge heat to sinks at nearly ambient conditions (Table 5-Table 6). Supercritical CO_2 is frequently applied across a various range of industrial and commercial sectors, spanning from the food, cosmetics, pharmaceuticals and materials. Moreover, supercritical CO_2 are used for extraction, impregnation, formulation, sterilization and cleaning. Other field where sCO_2 plays a significant role include geology and mineralogy for hydrothermal synthesis, chemistry as an organic solvent (carbon dioxide ranks as the second least expensive solvent after water), oil and gas industries for innovative separation techniques, particularly in supercritical fluid extraction and petrochemical sector for improving the recovery of viscous oil and the processing of petroleum products. To summarize, the applications in which sCO_2 is involved can be categorized by heat source and include geothermal, industrial, solar, biomass and nuclear applications (as outlined in Table 7).

Chemical Symbol	**Molar Mass**	**Critical Temperature and Pressure**	**Density**
CO_2	44.011 g/mol	304.21 K; 73.3773 bar	0.4676 kg/l

Table 5 – Characteristics of CO_2

Properties	**Effects**
High density and low viscosity	Reduced compressor work, increased compactness and reduced complexity
Critical temperature near room temperature	Wide availability
Abundance	Low cost

Table 6 – CO_2 properties and their effects

Application	**Temperature**
Nuclear	350-700°C
Fossil fuel	550-900°C
CSP	500-1000°C
Shipboard propulsion	200-300°C
Shipboard house power	230-650°C
Waste heat recovery	230-650°C
Geothermal	100-300°C
Fossil Fuel	1100-1500°C

Table 7 – CO_2 applications and their temperatures

1.1.2 TITANIUM TETRACHLORIDE ($TiCl_4$)

Titanium tetrachloride, an economically affordable and non-carcinogenic substance, exhibit a complete absence of Global Warming Potential and Ozone Depleting Potential. It is currently utilized in high-temperature industrial processes for the production of pure metal titanium and it has demonstrated exceptional thermal stability through a prior thermal analysis conducted at temperatures up to 550°C. Nevertheless, challenges arise in the storage and handling of this fluid, requiring air-tight packaging and dry conditions to prevent exposure to the open air. At room temperature, it exists in a colorless liquid state, with a normal boiling point of 136.5°C and a normal melting point of -24°C. One notable drawback is its high reactivity with water, even in the presence of small amounts typically found in humid air, resulting in the generation of heat and corrosive gases containing hydrogen chloride. Additionally, $TiCl_4$ exhibits corrosive properties towards various metals in the presence of water. However, these unfavorable characteristics become less critical when the substance is highly diluted with CO_2. Table 8 lists some of its high-temperature applications.

Application	Temperature
Working fluid for high-temperature power cycles	500-800°C
Kroll process to produce metallic titanium	700-1000°C
Chemical vapor deposition	726-1726°C
Thermochemical production of TiO_2	1226-1726°C

Table 8 – $TiCl_4$ applications and their temperatures

1.1.3 SILICON TETRACHLORIDE ($SiCl_4$)

Silicon tetrachloride, also known as Tetra-chlorosilane, is an inorganic compound utilized in the industrial sector for the production of highly pure silicon or silica. It exhibits exceptional thermal stability, rendering it well-suited for high-temperature processes. In the Siemens process, utilized for the production of high-purity silicon, $SiCl_4$ is generated as a by-product during the pyrolysis of $SiHCl_3$. To enhance silicon production, $SiCl_4$ must undergo reduction with hydrogen or H_2-radicals, typically carried out at temperatures around 900°C. Notably, the compound maintains its stability even at elevated temperatures, such as 1200°C. At standard room temperature, silicon tetrachloride assumes a state of a colorless liquid, with a boiling point of 57.6°C and a melting point of -68.7°C. Table 9 enumerates some of its applications in high-temperature processes.

Application	Temperature
Chemical vapor deposition (CVD)	600-1100°C
Silicon Production	850-900°C

Table 9- $SiCl_4$ applications and their temperatures

1.1.4 SULPHUR DIOXIDE (SO_2)

Sulfur dioxide is a colorless gas characterized by a pungent odor. It exhibits notable solubility in a variety of organic solvents and is utilized as a solvent and reaction medium. Two key properties are its resistance to thermal degradation and its non-combustible and non-explosive nature when mixed with air. Previous research has elucidated the potential reactivity of sulfur dioxide with metals in elevated temperature environments. Notably, nickel alloys, frequently utilized in high-temperature components, typically demonstrate resistance to SO_2 exposure, although they may still be vulnerable to sulfur-related concerns, including sulfidation. To ensure safety, it is essential to be aware that sulphur dioxide is toxic when inhaled and can cause strong irritation. Its melting point and boiling point are -75.5°C and -10°C, respectively. Table 10 enumerates some of its applications in high-temperature settings.

Application	Temperature
Precursor to sulfuric acid	450°C

Table 10 - SO_2 applications and their temperatures

1.1.5 HEXAFLUOROBENZENE (C_6F_6)

Hexafluorobenzene, also known as perfluorobenzene, is an organic compound that closely resembles benzene in its molecular structure, but with hydrogen atoms entirely replaced by fluorine atoms. It belongs to the category of perfluorocarbons, characterized by strong molecular bonds, including C-C, C=C and C-F, along with exceptional solvent properties. Despite its high flammability, it is generally considered to be a relatively safe choice when compared to other fluids utilized at medium-high temperatures. Research efforts have been directed towards assessing the thermal stability of hexafluorobenzene, revealing its ability to withstand temperatures of approximately 600°C when blended with CO_2 [129]. Its aromatic molecular structure with double bonds, provides an energy barrier against thermal decomposition reactions. Furthermore, it is important to note that compounds featuring fully aromatic rings and benzene-based heterocyclic ring systems have exhibited a high thermal stability. Nonetheless, further investigations are imperative to assess the material compatibility of hexafluorobenzene under high-temperature conditions, ensuring its thermal stability. Noteworthy properties of hexafluorobenzene include its melting and boiling points at 5.2°C and 80.1°C, respectively.

1.1.6 PERFLUOROBUTANE (C_4F_{10})

Perfluorobutane (PFB) is a fluorocarbon gas with a chemical structure similar to butane, but with all its hydrogen atoms replaced by fluorine atoms. Perfluorocarbons have gained significant interest within both the research and industrial sectors owing to their extraordinary gas-dissolving capabilities, making them potentially valuable in petrochemical refinery gas absorption processes. This gas is colorless and inert under normal conditions and exhibits a boiling point of -2.1°C and a melting point of -129°C. Perfluorobutane has been identified as a promising dopant for low-temperature applications. Earlier investigations into the thermal stability of a similar linear perfluorocarbon (C_6F_{14}) have a thermal stability up to 350°C and a discernible sign of decomposition at 400°C. This observation points out the lesser stability of linear fluorocarbons when compared to their cyclic and aromatic counterparts. Considering the stability range observed for C_6F_{14}, extending from 350°C to 400°C, it is reasonable to expect that C_4F_{10}, characterized by its lower molecular complexity, would demonstrate higher thermal stability. In general, shorter linear molecular chains tend to possess superior thermal stability due to their reduced number of C-C single bonds, widely regarded as the weakest bonds in fluorocarbons. This results in a lower probability of molecular collisions that could lead to dissociation reactions (Arrhenius theory). Previous evaluations of thermal stability conducted on C_4F_{10} within the framework of the SCARABEUS project confirmed its robustness and a thermal stability up to 500°C. The primary drawback associated with C_4F_{10} is its elevated Global Warming Potential (GWP), equivalent to 8,860 (for a 100-year time horizon). However, this limitation can be mitigated by blending C_4F_{10} with carbon dioxide.

1.1.7 NOVEC 4710

Novec 4710, also known as C_3F_7CN (fluoronitrile) and manufactured by 3M Company, is a sustainable and environmentally friendly option to replace sulfur hexafluoride (SF_6) in applications involving electrical equipment insulation and arc quenching. Novec 4710, when combined with inert gases, exhibits a notably low Global Warming Potential (GWP) and a complete absence of ozone depletion potential (ODP). These characteristics make it highly advantageous for mitigating environmental impacts. The thermal stability of Novec 4710 is notably robust; data on thermal stability found in literature reports that a mixture of 500 ppmv of Novec 4710 in CO_2 demonstrated no discernible thermal decomposition until temperatures approached 800 °C. In summary, this pioneering gas offers a more environmentally responsible, safer, and dependable choice for electrical applications, thus contributing to a more sustainable future.

1.2 Preliminary thermodynamic analysis

A preliminary evaluation of the power cycle was conducted using both pure CO_2 and CO_2 blends to evaluate the cycle's efficiency and have an idea of their performance within the considered application. This initial evaluation focused on identifying the most promising mixture composition using a Transcritical Simple Recuperative (SR) configuration and the PENG ROBINSON state equation, implemented in Aspen Plus v12.0 Software. The choice of this cycle configuration was motivated by its simplicity and its potential to lower the levelized cost of electricity (LCOE). SR cycle contains few components: compressor, recuperator (REC), primary heat exchanger (PHE) and turbine. The SR cycle starts at state point 1, where the fluid enters a pump (or a compressor) to increase its pressure. The fluid then flows out of the pump (or a compressor) at state 2 and into a recuperative heat exchanger where it receives energy input from the fluid exiting the turbine. The fluid subsequently enters the primary heat exchanger at state 3 and at state 4 is expanded through the turbine. From here the fluid passes through the internal recuperator at state point 5 where it gives up energy to the fluid from the compressor (refer to Figure 8):

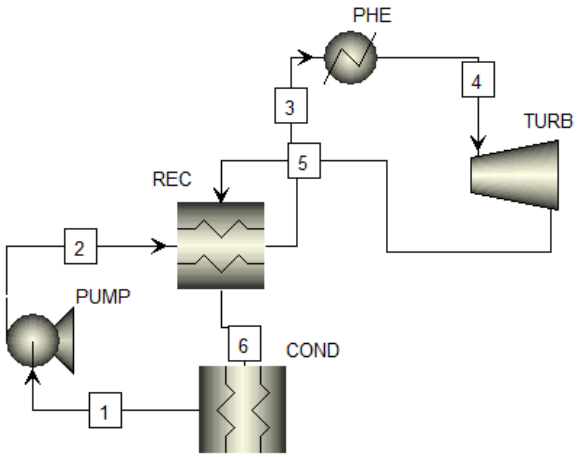

Figure 8 – Simple recuperative (SR) power cycle

In addition, it is possible to further improve the overall efficiency of the cycle by using a Recompression cycle (RC) (Figure 9), a more complex cycle than the Simple Recuperative (SR). RC cycle includes two compressors (main compressor (1-3) and recompression compressor (10-11)), two recuperators (3-4) and (9-12), flow splitter (SPLIT) and mixer (MIX). Bypassing the low-temperature recuperator (REC1) with a portion of the flow increases the temperature entering (and exiting) the high-temperature recuperator (REC2), reducing the exergy destruction in the primary heat exchanger (H). While this power cycle does slightly complicate the system, the thermal efficiency typically increases enough to offset the economic cost and complexity of the added components. The analysis mentioned earlier can simply be modified to include the recompressor and a lower temperature recuperator throughout the cycle.

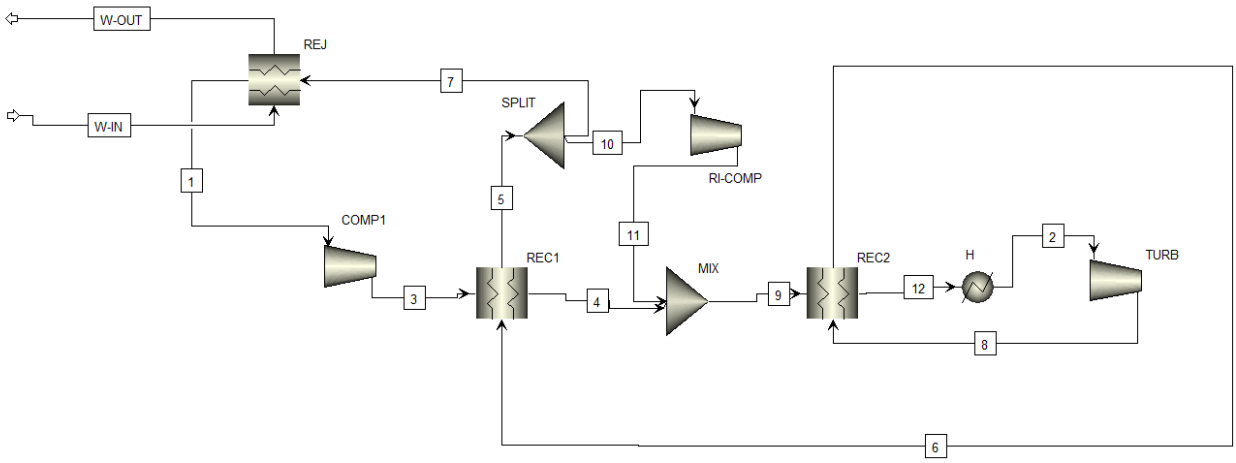

Figure 9 - Recompression cycle (RC)

The reference cycle assumptions for the following simulations are reported in Table 11 [149-151]:

Parameters	**Values**
Turbine inlet pressure	253 bar
Turbine inlet temperature	550°C
Minimum temperature	50°C
Heat exchanger minimum internal temperature difference	5°C
Compressor isentropic efficiency	88%
Turbine isoentropic efficiency	92%
Condenser pressure loss	2 bar
Primary heat exchanger (PHE) pressure loss	4 bar
Printed Circuit Heat Exchanger (PCHE) pressure loss HP/LP	0.5 bar/ 1 bar

Table 11 – Cycle's assumptions for pure CO_2 and blends

Clearly, variations in mixture composition lead to changes in thermodynamic properties of the working fluid. Therefore, optimizing the composition is essential to maximize efficiency, control blending costs and minimize environmental impact associated with specific compositions.

1.2.1 Simulation results for sCO₂ cycles (550 and 700°C)

For the pure fluid (i.e., pure CO_2), a comparative study was conducted between the two cycles, SR and RC, at two distinct maximum temperatures: 550°C and 700°C. The temperature of 550°C was selected due to its association with the maximum temperature for the pilot plant foreseen within the Desolination project [134], while the temperature of 700°C is a target temperature for next-generation CSP systems, aiming to achieve even higher efficiencies. In these analysis PC-SAFT equation of state is implemented. Under the specific cycle conditions detailed in Table 11, an efficiency analysis was conducted as function of the minimum pressure. The results are reported in Figure 10:

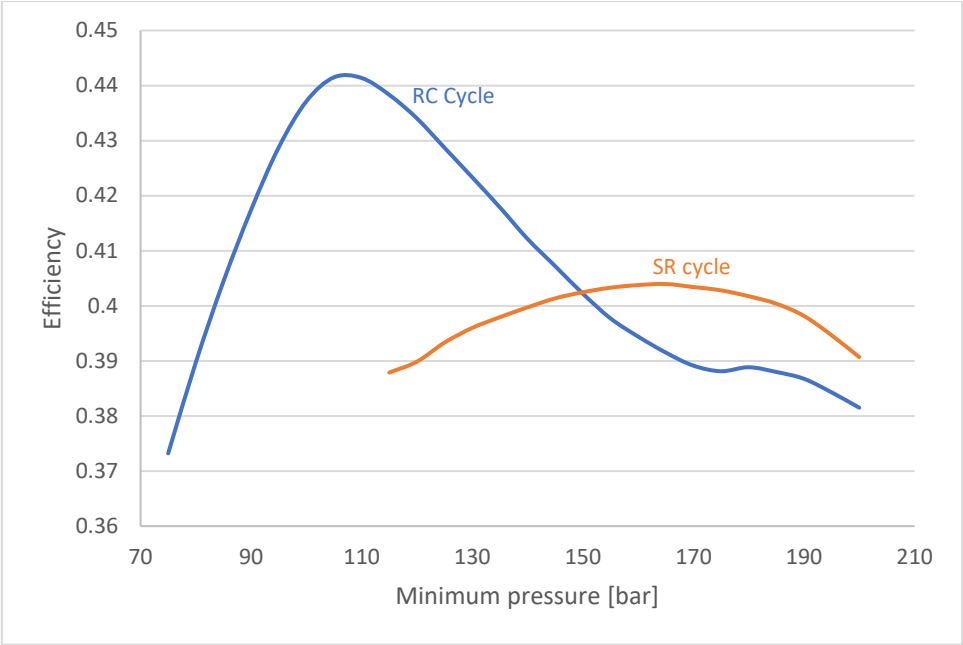

(a)

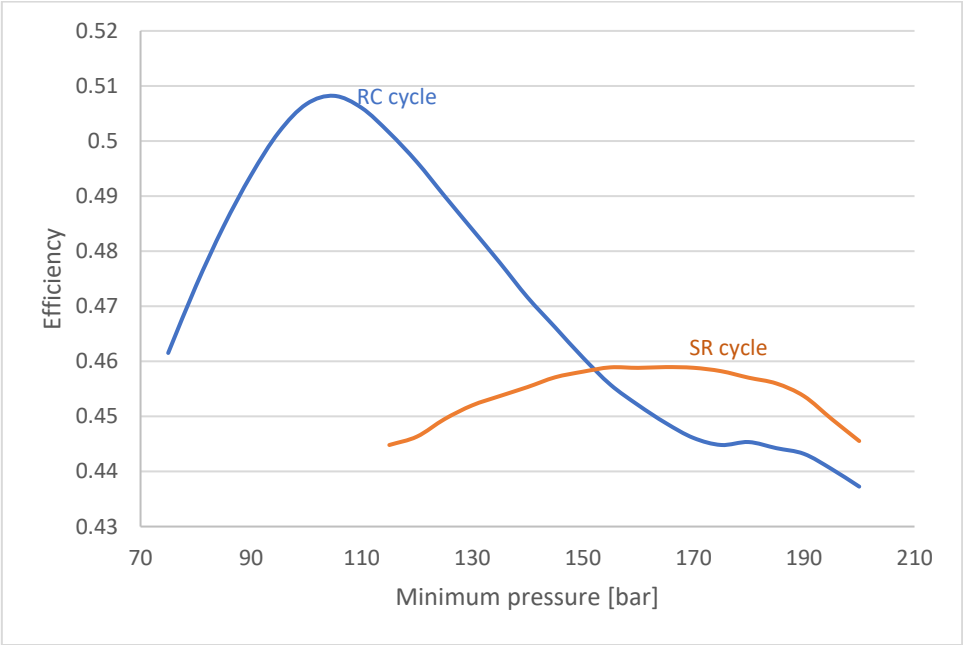

(b)

Figure 10 – Cicle efficiency vs minimum pressure at (a) 550°C and (b) 700°C

Based on the data presented in the above graphs, it is evident that, as expected, the recompression cycle consistently outperforms the simple recuperative cycle for both temperatures.

In particular, at 550°C, the maximum efficiencies are obtained with a minimum pressure of 165 bar for the SR cycle (40.39%) and 105 bar for the RC cycle (44.14%). At 700°C, maximum efficiencies are reached with a minimum pressure of 165 bar for the SR cycle and 105 bar for the RC cycle, resulting in maximum efficiency values of 45.90% and 50.82%, respectively.

1.2.2 Simulation results for sCO_2 blends cycles (550 and 700°C)

The cycle analysis for the sCO_2 blends was carried out considering all the selected dopants reported in Table 4 at 550°C, using the same conditions outlined in Table 11. For the case of 700°C, only the three mixtures deemed stable at that temperature were considered, namely $TiCl_4$, $SiCl_4$ and SO_2. Given the primary objective of optimizing cost-efficiency by employing the simplest power cycle, as previously mentioned, the mixtures were assessed using a simple recuperative cycle. For each mixture, the PENG ROBINSON state equation was implemented, with the exception of the CO_2+SO_2 blend, for which the PC-SAFT state equation was considered more appropriate, as indicated in [148].

Figure 11, presents the efficiencies of various mixtures as a function of the molar fraction of CO_2. As reference values, the maximum efficiencies achieved with pure sCO_2 in SR and RC cycles, for both temperatures are also reported in the dotted lines.

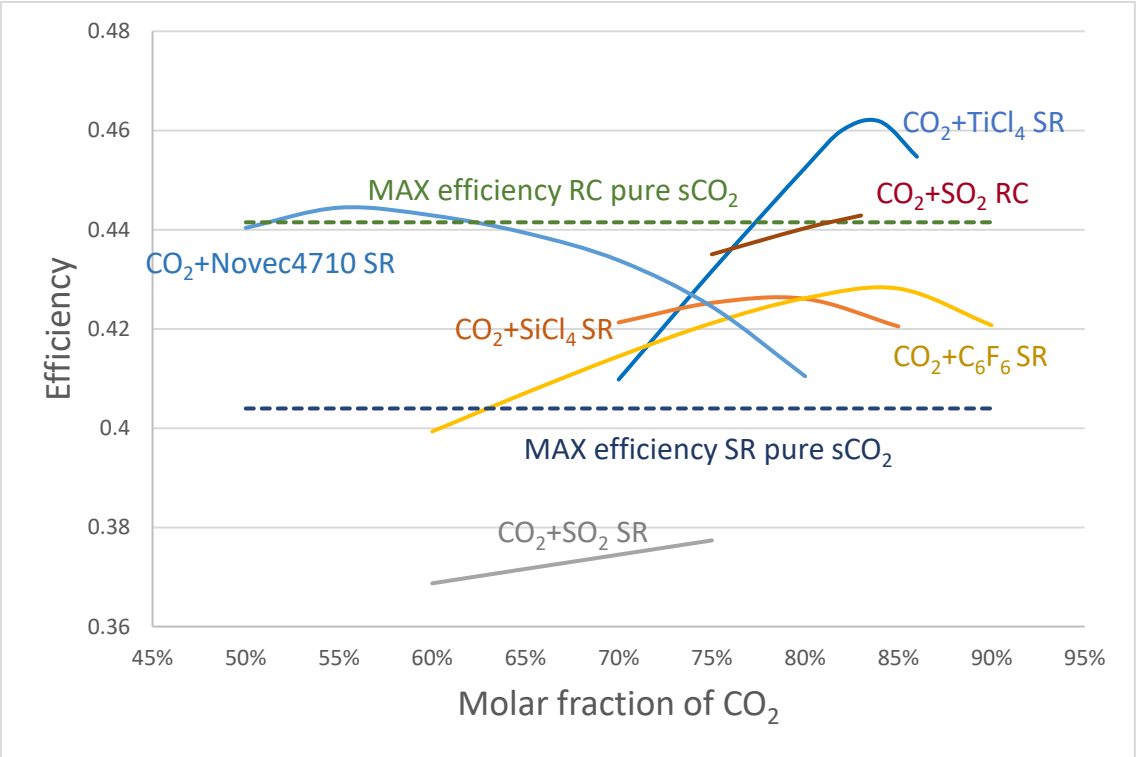

(a)

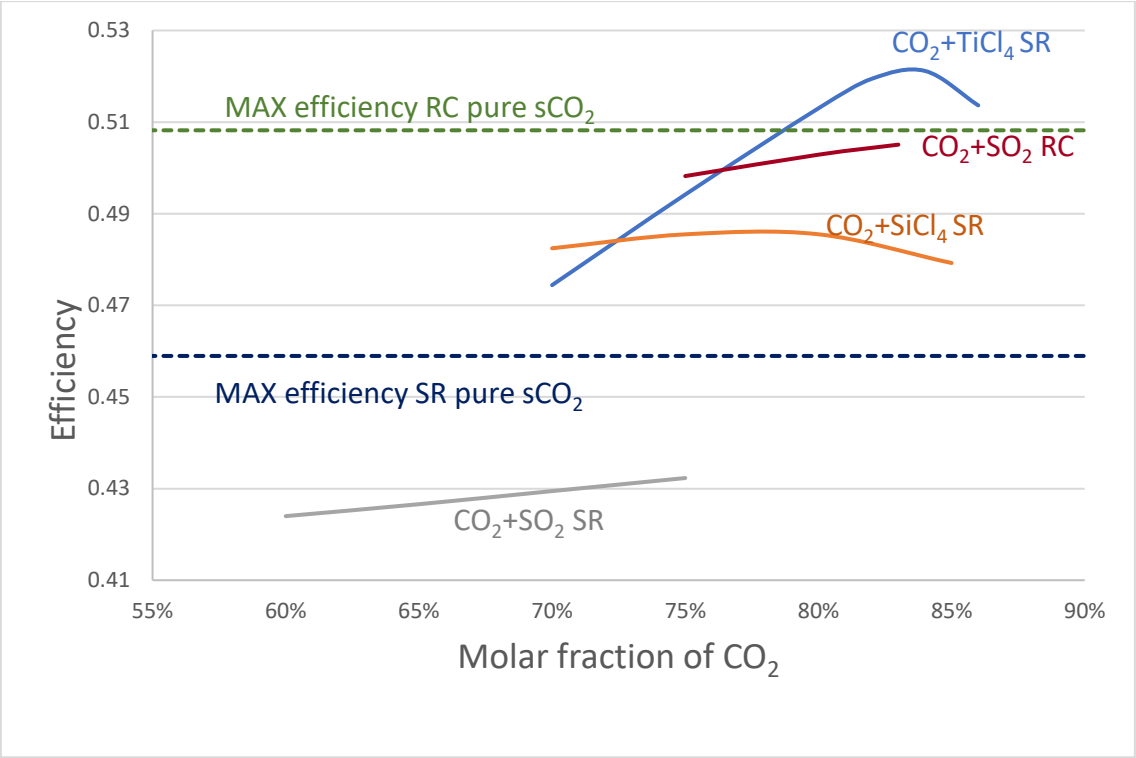

(b)

Figure 11 - Cycle efficiency vs composition at (a) TIT=550°C and (b) TIT=700°C

It can be observed that, at both temperature levels, all the mixtures show efficiencies higher than those of pure CO_2 in the SR cycle and comparable with those of pure sCO_2 in the RC cycle.

Notably, the blends containing Novec4710 and $TiCl_4$ at 550°C, as well as $TiCl_4$ at 700°C, at the optimized compositions outperform pure sCO_2 in RC. The only exception concerns the blend containing SO_2, which shows a lower efficiency compared to pure CO_2. For this reason, this particular blend was evaluated also with a recompression cycle to enhance its performance. As shown in Figure 4, when the RC cycle is considered for the CO_2+SO_2 blend, the efficiency exceeds that of pure CO_2 at 550°C, while at 700°C, it aligns with the values of pure CO_2.

In particular, Table 12 and Table 13 list, at 550°C and 700 °C, the maximum efficiency and the corresponding optimized CO_2 fraction. For some blends, the maximum efficiency and the corresponding CO_2 moral fraction data found in literature under very similar conditions are also reported.

Dopant	**CO_2 molar fraction and Max efficiency**	**CO_2 molar fraction and Max efficiency – Literature data**
$TiCl_4$ (SR cycle)	84% and 46.18%	83% and 45.42% [153]
$SiCl_4$ (SR cycle)	80% and 42.61%	
SO_2 (RC cycle)	83% and 44.29%	70% and 44.32% [153]
C_6F_6 (SR cycle)	85% and 42.28%	42.4% [70] - 86% and 41.9% [150] - 84% and 41.3% [151]
Novec4710 (SR cycle)	65% and 43.93%	
CO_2 (SR cycle)	100% and 40.40%	100% and 37.4% [151]
CO_2 (RC cycle)	100% and 44.15%	100% and 41.7% [151] or 41.9% [70]

Table 12 – Maximum efficiency and corresponding molar fraction of CO_2 at TIT=550°C

Dopant	**CO_2 molar fraction and Max efficiency**	**CO_2 molar fraction and Max efficiency – Literature data**
$TiCl_4$ (SR cycle)	84% and 52.12%	82% and 49.5% [152]
$SiCl_4$ (SR cycle)	80% and 48.55%	
SO_2 (RC cycle)	83% and 50.50%	80% and 51.4% [71]
CO_2 (SR cycle)	100% and 45.90%	100% and 45.3% [71]
CO_2 (RC cycle)	100% and 50,82%	100% and 49.8% [71]

Table 13 - Maximum efficiency and corresponding molar fraction of CO_2 at TIT=700°C

Through a comparison with the data available in the literature, it is evident that, in general, the use of SR cycles is preferable for all dopants, except for SO_2, for which the implementation of RC cycles is recommended. The trends of efficiency and molar composition curves closely resemble those obtained in this thesis, with maximum performance values and their corresponding CO_2 molar fractions being comparable.

In summary, this preliminary simulations show the considered CO_2 mixtures yield favorable results, comparable or even exceeding those of pure CO_2. Therefore, the following the chapters will delve into a detailed analysis of material compatibility for the most promising CO_2 blends considered so far.

CHAPTER 2

MIXTURES' COMPATIBILITY BETWEEN MATERIALS AND INNOVATIVE BLENDS OF sCO_2.

The degradation of the working fluid can be significantly influenced by the utilization of specific materials. This may lead to adverse consequences on the performance of power plants, particularly in their high-temperature sections. This aspect represents an innovation in scientific literature. While numerous studies have explored material compatibility for steam and supercritical carbon dioxide in power plants, as mentioned previously, there is a lack of experimental and theoretical analysis in case of carbon dioxide mixtures. The only exceptions are some studies that consider material compatibility with carbon dioxide in the presence of contaminants such as water, oxygen, sulphur dioxide and nitrogen dioxide. However, these analyses generally pertain to relatively small amounts of impurities within a temperature range typically lower than that used in a solar power plant. It is worth noting that the results of this research have significant implications for the techno-economic optimization of the power block, as they enable the identification of the most cost-effective materials to be used at different temperatures and in various sections of the plant.

In the literature there are several experimental techniques used to investigate the effects of sCO_2 on materials:

- Corrosion Rate Measurement: it is frequently determined by using gravimetric methods, which encompass both the weight gain and weight loss techniques.
- The corrosion rate Vc [$\frac{m}{h}$] is calculated with the formula:

$$Vc = \frac{87600\ \Delta m}{\rho\ \mathrm{x}\ A\ \mathrm{x}\ T}$$

  where Δm is the weight loss [g]; A is the area of the specimen [m^2]; T is the corrosion time, [h], ρ is the density of specimen [g/cm^3]; T is the corrosion time [h]; the number written in the equation is the unit conversion constant [154-156].

- Local Corrosion Rate Measurement: the use of this approach is limited to pitting. An average pit depth from the 10 deepest pits detected on the samples cross section is used to evaluate the localized corrosion rate (LC) by applying the following formula:

$$RL = \frac{8.76h}{t}$$

  where h is the depth of the local corrosion pit; t is the corrosion time [h] [157].

- Electrochemical Evaluation: it measures corrosion current, corrosion potential, and analyses the electrodes processes of the electrochemical system. A three-electrode system is employed with an electrochemical workstation. The larger the corrosion current density, the more severe the corrosion of the material [158-159].

- Autoclave Method: it is a widespread method that involves the use of an autoclave wherein samples and the desired fluid are placed [160-161].

- Structural Evaluation: common research practices for corrosion test specimens encompass their preparation, cleaning, and subsequent evaluation. Characterization of the material structure occurs across various scales using diverse techniques, including scanning electron microscopy (SEM), X-ray diffraction (XRD), Raman spectroscopy, infrared spectroscopy (IR), transmission electron microscopy (TEM), and/or Mossbauer spectroscopy (where a nucleus emits or absorbs gamma rays without recoil) [162-163]. In particular, SEM offers detailed images of the surface morphology at a high resolution; XRD identifies the crystal structure of the material by analyzing how X-rays interact with its atomic arrangement, revealing information about crystalline phases; Raman spectroscopy examines vibrational modes of molecular bonds, offering details about the chemical composition and molecular structure of the material; IR analyses the absorption of infrared light by molecular bonds providing info about functional groups and molecular vibrations in the material; TEM utilizes transmitted elections to achieve high resolution images of the material's microstructure; Mossbauer Spettroscopy allows precise analysis f chemical, structural and magnetic properties at the atomic leel.

The methodology employed in the preparation of the thesis is influenced by these approaches.

Three tests on materials were conducted, each with specific procedures:

- **Preliminary corrosion tests** on metallic alloys in contact with supercritical carbon dioxide (sCO_2) blends were carried out by using a pressure vessel made from different materials: IN625, AISI 316 and AISI 304. These barrels consisted of a cylindrical body directly welded to two bottoms. In this specific case, welding was preferred to the screw joint due to its advantages in minimizing fluid leakage and simplifying the design. Furthermore, given the preliminary nature of these tests, there was no need for vessel reusability, making a disassemblable vessel unnecessary. This phase focused on analysing the interaction of the sCO_2 blend with the cylindrical body and the welded region inside the vessel. Figure 12 and Figure 13 show the vessels and the initial cuts to collect the samples for the analysis. It is important to note that the vessel geometry of AISI 316 closely resembled that of AISI 304. The experimental tests were conducted to obtain initial insights into the behavior of materials, particularly in the presence of an atmosphere containing perfluorocarbons, and to gain an understanding of both Ni and Fe-based alloys performance in such environment.

Figure 12 - Pressure vessel made in IN625 and its parts

Figure 13 - Pressure vessel made in AISI 304 and its parts

The experiments were conducted under supercritical conditions in the range of 500-600°C, for a duration of 300 hours. The material analysis involved the extraction of two metallographic samples from the vessel, one collected from the shell of the cylindrical barrel and the other from the weld and the preparation of

the metallographic samples to evaluate the corrosive effects of supercritical carbon dioxide blends. All barrels, except that made in AISI 304, underwent weld analysis. It is worth to mentioning that each weld was performed by using the same filler metal as the base material to mitigate any potential galvanic corrosion effect. The nominal chemical compositions of these alloys were shown in Table 14.

	C	Si	Mn	P	S	Al	Co	Cr	Fe	Mo	Ti	Ni	Na+Ta
IN625	0.029	0.1-0.5	0.08-0.5	0.005-0.015	0.001-0.015	0.24-0.4	0.13-1	20-23	3.92-5	8-10	0.25-0.4	58-60.3	3.15-4.15
AISI316	0.035	0.75	2		0.03			16-18	68-76	2-3		11-14	
AISI304	0.035	0.75	2		0.03			18-20	66-71			8-11	

Table 14– Nominal chemical compositions of the considered alloys

After the metallographic preparation, the samples were observed in cross-section under the optical microscope to assess the damage caused by the exposure to the mixture (Table 15).

Samples	Atmosphere	Temperature	Weight change	Preparation	Optical Microscope	SEM surface	SEM cross-section
IN625	50%CO_2+50%C_4F_{10}	550°C		X	X		
IN625	80%CO_2+20%C_6F_6	650°C		X	X		
AISI304	Pure CO_2	500°C		X	X		
AISI316	80%CO_2+20%C_6F_6	550°C		X	X		
IN625	80%CO_2+20%C_6F_6	500°C		X	X		
IN625	92%CO_2+8%C_6F_6	550°C		X	X		
IN625	80%CO_2+20%SO_2	550°C		X	X		
IN625	80%CO_2+20%$SiCl_4$	550°C		X	X		

Table 15 - Information about samples, atmosphere and analyses performed in the preliminary tests

As already mentioned, the materials considered in the preliminary tests were the nickel-based alloy Inconel 625 and the austenitic stainless steels AISI 304 and AISI 316.

- In the **first test campaign**, the test setup was updated to process a larger number of samples at the same time. Furthermore, as perfluorocarbons have demonstrated notable aggressiveness on both nickel-based and iron-based alloys, this first experimental campaign focused on investigating the interaction of two new CO2-dopants with several different materials. In this case, two welded pressure vessels, made by IN625 housed each one a 99% alumina rod upon which 12 disks of different materials were fixed, and separated with spacers composed of 96.5% alumina interposed between them to prevent any potential mutual interaction or shadowing effects (Figure 14-a),. These disks had a hollow design with internal and external diameters measuring 6.5 mm and 32 mm, respectively and a thickness of 4 mm (Figure 14 a-b). The hollow geometry served the purpose of fixing the samples within the vessel. One vessel was filled with an 80%CO_2+20%SO_2 mixture and the other with 80%CO_2+20%$SiCl_4$.

(a) (b)

Figure 14– Set-up of the first test campaign (a) and samples geometry (b)

The tests were carried out under supercritical conditions at 550°C, with a duration of 547 h for the mixture containing $SiCl_4$ and 681 h for the mixture containing SO_2. Before the high-temperature (HT) test, the samples underwent ultrasonic cleaning in an ethanol bath, followed by drying with hot air and subsequent weighing with a Gibertini E42-B balance with a precision of 0.1 mg. At the end of tests, the samples were re-weighed to determine the weight gain per unit of area exposed to the corrosive environment. This parameter is commonly used in literature for facilitating comparisons regarding the performance of different materials in corrosive atmospheres. After this, the samples underwent comprehensive analysis by using optical microscopy and scanning electron microscopy (SEM) techniques, as detailed in Table 16.

Samples	Atmosphere	Temperature	Weight change	Preparation	Optical Microscope	SEM surface	SEM cross-section
IN625 additive	80%CO_2+20%SO_2	550°C	X	X	X	X	X
IN625 additive with weld			X	X	X	X	X
IN625 forged			X	X	X	X	X
ASTM A494 CW6MC			X	X	X	X	X
IN725			X	X	X	X	X
IN718			X	X	X	X	X
G130			X	X	X	X	X
IN625 additive	80%CO_2+20%$SiCl_4$	550°C	X	X	X	X	X
IN625 additive with weld			X	X	X	X	X
IN625 forged			X	X	X	X	X
ASTM A494 CW6MC			X	X	X	X	X
IN725			X	X	X	X	X
IN718			X	X	X	X	X
G130			X	X	X	X	X

Table 16 – Information about samples, atmosphere and analyses performed in the first test campaign

In detail, the materials considered in first test campaign included nickel-based alloys, such as Inconel IN625 additive and IN625 additive with weld (produced using additive manufacturing techniques), IN625, IN718 and IN725 (produced by forging), ASTM A494 CW6MC, and G130 (manufactured by casting). Their nominal chemical compositions were reported in Table 17:

	C	Si	Mn	P	S	Al	Co	Cr	Fe	Mo	Ti	Ni	Na+Ta	Nb	B
IN625	0.029	0.1-0.5	0.08-0.5	0.005-0.01	0.001-0.01	0.24-0.4	0.13-1	20-23	3.92-5	8-10	0.25-0.4	58-60.3	3.15-4.15		
IN725	0.00-0.03	0.0-0.2	0.00-0.35	0.00-0.02	0.00-001	0.00-0.35		22-50	bal.	7-9.5	1-1.7	55-59		2.75-4	
IN718	<0.08	<0.35	<0.35	<0.015	<0.015	0.2-0.8	<1	17-21	bal.	2.8-3.3	0.65-1.15	50-55	<0.05	4.75-5.5	<0.006
A494	0.029	0.1-0.5	0.08-0.5	0.005-0.01	0.001-0.01	0.24-0.4	0.13-1	20-23	3.92-5	8-10	0.25-0.4	58-60.3	3.15-4.15		
G130	0.015	0.2	0.5				19.5	24.5				bal.			

Table 17 -Nominal chemical composition of the considered alloys

- In the **second test campaign**, a refined procedure was developed. In the aftermath of the previous experimental campaign, the most effective alloy composition was identified, providing initial insights into materials best suited for that specific atmosphere. To align the procedure more closely with literature and to gain a better understanding of the evolution of the corrosive phenomenon over time, the experimental setup was modified to allow the extraction of samples during the experiment. The samples were placed within a disassemblable vessel, allowing the interruption of tests at predetermined times, approximately every 600 hours, with an overall duration of 2000 hours (Figure 15).

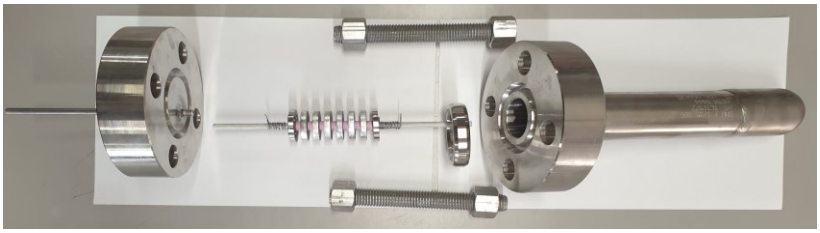

Figure 15 – Second test campaign set-up

Whenever the test was interrupted, the samples were removed from the pressure vessels and weighed to assess the weight gain/loss relative to the initial value, as done in the first test campaign. After weighing, the samples were reinserted into the vessel. The tests were conducted at two distinct temperatures: 120°C and 550°C, as documented in Table 18.

Samples	Atmosphere	Temperature	Weight change	Preparation	Stereo-microscope	Optical Microscope	SEM surface	SEM cross-section
IN725	$80\%CO_2+20\%SO_2$	120°C	X		X		X	
ASTM A216 WCB			X		X		X	
AlCrO by PVD			X		X			
ASTM A494 CW6MC			X		X			
X22CrMoV12			X		X			
SiO2 by PECVD			X		X			
Carbonitrided			X		X			
FLOMA 200			X		X			
Reinforced PTFE			X		X			
Pure PTFE			X		X			
IN725	$80\%CO_2+20\%SO_2$	550°C	X	X	X	X	X	X
IN625 additive			X	X	X	X	X	X
IN625 additive with weld			X	X	X	X	X	X
IN718 additive			X	X	X	X	X	X
IN718 additive with weld			X	X	X	X	X	X
G130			X	X	X	X	X	X
Carbonitrided			X					
AlCrO by PVD			X	X	X	X	X	X
SiO2 by PECVD			X	X	X	X	X	X
IN718			X	X	X	X	X	X
CrNO by PVD			X				X	
Waspaloy			X	X	X	X	X	X

Table 18 - Information about samples, atmosphere and analyses performed in the second test campaign

In detail, the materials considered in this campaign were:

- nickel-based alloys, including IN725, IN718 (manufactured by forging), ASTM A494 CW6MC (manufactured by casting), IN625 additive, IN718 additive, IN625 additive with weld, and IN718 with weld (additively manufactured) and G130 (manufactured by casting);
- cobalt-based alloys, such as Waspaloy,
- iron-based alloys, such as carbon steel ASTM A216 WCB and martensitic stainless steel X22CrMo12;
- different surface treatments or coatings, such as AlCrO by PVD, CrNO by PVD, SiO2 by PECVD and carbonitriding. The surface treatments and coatings shared X22CrMoV12 as a matrix.

Additionally, polymers were considered, such as pure and reinforced PTFE and the ceramic material Floma 200. Their nominal chemical compositions were reported in Table 19.

	C	Si	Mn	P	S	Al	Co	Cr	Fe	Mo	Ti	Ni	Na+Ta	Nb	B	Cu	Zr	V
IN725	0.00-0.03	0.0-0.2	0.00-0.35	0.00-0.02	0.00-001	0.00-0.35		22-50	bal.	7-9.5	1-1.7	55-59		2.75-4				
IN718	<0.08	<0.35	<0.35	<0.015	<0.015	0.2-0.8	<1	17-21	bal.	2.8-3.3	0.65-1.15	50-55	<0.05	4.75-5.5	<0.006			
A494	0.029	0.1-0.5	0.08-0.5	0.005-0.01	0.001-0.01	0.24-0.4	0.13-1	20-23	3.92-5	8-10	0.25-0.4	58-60.3	3.15-4.15					
IN625	0.029	0.1-0.5	0.08-0.5	0.005-0.01	0.001-0.01	0.24-0.4	0.13-1	20-23	3.92-5	8-10	0.25-0.4	58-60.3	3.15-4.15					
G130	0.015	0.2	0.5				19.5	24.5				bal.						
Waspaloy	0.07	0.75	1	0.03	0.03	1.4	13.5	19.5	2	4.25	3	54			0.006	0.5	0.06	
A216	<0.3	<0.6	<1	<0.035	<0.035			<0.5	bal.	<0.2		<0.5				<0.3		<0.03
X22CrMoV12	0.22	0.22	0.65	0.02	0.003			11.5	bal.	0.85		0.65						0.3

Protec	AlN-based
Moldena	CrN/CrON

Table 19 –Nominal chemical composition of the considered alloys

- The **third test campaign** was conducted similarly to the second one on the samples listed in Table 5. The aim was to further investigate that class of materials and coatings that had exhibited superior performance in the previous campaign. The methodology remained unchanged, as it aligns with the approaches found in the existing literature. However, after 118 hours, an anomalous pressure drop was recorded, leading to the interruption of the test. The samples appeared to be covered with a dark deposit. Specific analyses were carried out on the samples that appeared more damaged, both before and after a mechanical cleaning operation, to identify the cause of the pressure drop. Materials and tests are detailed in Table 20.

Samples	Atmosphere	Temperature	Weight change	Preparation	Optical Microscope	SEM surface	SEM cross-section
IN740	80%CO_2+20%SO_2	550°C	X				
CrC NiCr Wasp HVOF			X	X	X		X
Stellite cladding			X	X	X	X	X
CrC wasp base Co HVOF			X	X	X		X
Nimonic			X				
Stellite cast 6			X				
L605			X				
L605 HVOF wasp			X				
CrNO by PVD			X				
AlCrO by PVD			X				
G130			X				
MCrAlY PVD			x				

Table 20 - Information about samples and procedures of the third test campaign

In particular, the materials considered include:

- nickel-based alloys, such as Inconel IN740 and G130 (manufactured by casting);
- Cr-Co alloys, such a Nimonic;
- Co-based alloys, such as cast Stellite 6;
- high-velocity oxygen fuel (HVOF) coatings like CrC NiCrWasp, CrCwasp base Co, and L605 wasp with Waspaloy as the matrix;

- cladding coatings, such as Stellite;
- physical vapor deposition (PVD) coatings, such as MCrAlY PVD, AlCrO by PVD and CrNO by PVD.

It is worth noting that G130, AlCrO by PVD and the CrNO by PVD samples were the same already tested for 2000 h in the previous test campaign. Their nominal chemical composition is reported in Table 21:

	C	Si	Mn	P	S	Al	Co	Cr	Fe	Mo	Ti	Ni	Na+Ta	Nb	B	Cu	W
IN740	0.005-0.08	0.00-1	0.00-1	0.00-0.03	0.00-0.03	0.2-2	15-22	23.5-25.5	0.00-3	0.00-2	0.5-2.5	bal.		0.5-2.5	0.0006	0.00-0.5	
G130	0.015	0.2	0.5				19.5	24.5				bal.					
Nimonic	<0.1	<0.4	<0.5		<0.03	<0.35	<1	12.5	bal.	5.75	2.9	42.5				<0.5	
Stellite 6	1						66	26	3			3					5
L605	0.05-0.15	<0.4	1-1.2	<0.04	<0.03		rest.	19-21	<3			9-11					14-16

Table 21–Nominal chemical composition of the considered alloys

2.1 High Temperature Test Set-Up (common for all test campaigns)

The fluid sealed in pressure vessel was heated in a furnace and continuously monitored for temperature and pressure. The setup included the pressure vessel (A), four needle valves (B), two pressure transmitters (C), a fitting for fluid connections (D) and an external thermocouple (Figure 16).

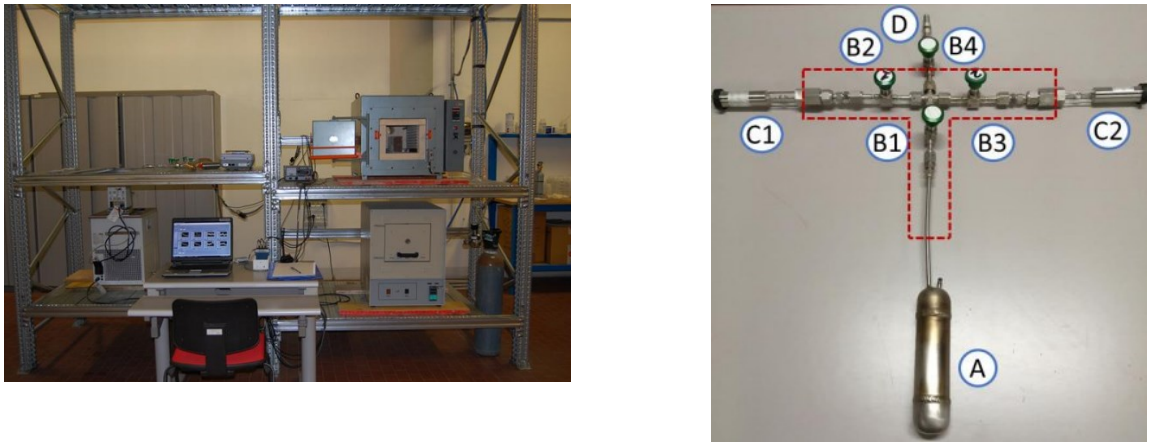

Figure 16 – Test setup

The fluid compositions were fixed on the basis of preliminary results obtained from the European projects Scarabeus and Desolination. The fluid mass in the vessel was determined to maintain the system pressure below 60 bar, preventing damages to the valves or to the vessel itself. The internal walls of the vessels remained in contact with the fluids at the specified conditions.

The list of the experimental characterization techniques that have been applied to study the interaction between the gas and the materials, is presented in Table 15Table 16Table 18Table 20 and can be summarized in the following points:

- preparation of metallographic samples;
- microstructural analysis with the optical microscope;
- SEM-EDS analysis on polished cross-sections and internal surfaces of the samples.

The main technologies used are described below.

The **MeF3** optical microscope, equipped with LAS4.12 software for image analysis, was employed for microstructural analysis and measurement of the interaction layer formed after prolonged exposure to the high-temperature environment., This metallographic optical microscope operates based on Chatelier's principle, involving the reflection of light from the sample surface using prism arrangements. It can observe

samples in reflected light, offering flexibility to view them from the top down or bottom up while maintaining the optical axis perpendicular to the sample surface. The microscope's design incorporates a glass plate positioned at a 45° angle to the light direction, partially reflecting light towards the objective lens. This reflected light illuminates the sample's surface, creating a magnified image through the objective lens. The microscope features an optical tube with an objective and eyepiece, mounted on a stand with a table for sample placement. Adjustability is provided for the distance between the objective and sample, as well as sample movement and condenser position for directed light intensity. The instrument employs multiple objectives and eyepieces, each marked with a magnification factor. The total magnification is the product of the eyepiece and objective magnifications. While magnification is a key aspect, resolution is also critical, and optical microscopes typically offer a resolution power of 0.2 µm due to the limitations of using white light (Figure 17).

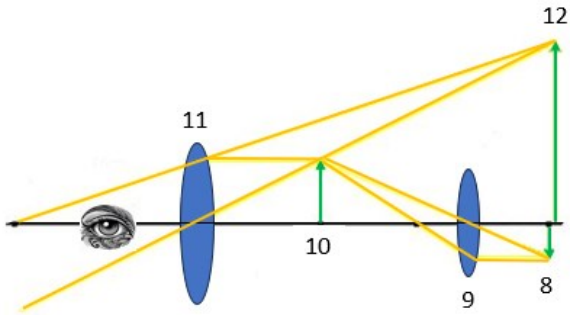

1. Ocular
2. Objective
3. Stage
4. Fine focus
5. Coarse focus
6. Condenser and diaphragm
7. Stage controls
8. Real object
9. Objective lens

Figure 17 - Diagram of the light path and the components of an optical microscope

The **EVO 40XVP scanning electron microscope (SEM)** and **Link Analytical eXL energy-dispersive spectroscopy (EDS) micro-analysis** were utilized for investigating high-temperature corrosion mechanisms in alloys. This involved examining both sample surfaces and polished cross-sections. SEM technique provides advantages over optical microscopy, offering insights into surface morphology, chemical composition, and surface contamination. The SEM setup includes a focused beam of primary electrons, a high vacuum system, electromagnetic lenses, deflection coils, an objective lens, signal detectors, a signal-to-image transformation system, and a sample chamber. In SEM, secondary electron imaging (SEI) and backscattered electron imaging (BSE) are the primary techniques used. SEI captures secondary electrons emitted from the sample's surface due to interactions with the primary electron beam, providing detailed surface morphology. BSE utilizes backscattered electrons to reveal information about the density of sample. Combining these techniques with EDS micro-analysis offers a comprehensive understanding of a sample's structure, morphology, chemical composition, and surface contamination.

The chemical analysis was performed utilizing **Energy Dispersion Spectrometry (EDS)**. This analysis is rapid and non-destructive, functioning by bombarding the sample with high-energy electrons, which, in turn, generate characteristic X-rays when interacting with the sample's atoms. These emitted X-rays have energies specific to the elements present in the sample. The EDS apparatus detects and measures the

energies of these X-rays, creating a spectrum representing the elemental composition of the sample. In this way is possible to identify the elements in the material and quantify their concentrations by analyzing the positions and intensities of the peaks in the spectrum.

CHAPTER 3 PRELIMINARY CORROSION TESTS: MATERIALS COMPATIBILITY WITH SUPERCRITICAL CO_2 MIXTURES CONTAINING PERFLUOROCARBONS

Below are presented the results obtained during the preliminary corrosion tests, ordered according to the considered gas mixture.

3.1 Microstructural analysis of materials under investigation

The microstructures of the pressure vessels are shown in Figure 17-18.

- The microstructure of **IN625** bulk was fully austenitic, with equiaxed grains. Furthermore, it is crucial to emphasize the existence of banding resulting from the alignment of micro-segregations during the manufacturing process. In Figure 18, a high-magnification overview of the welded section of IN625 is shown. In particular, Figure 18-b reveals three distinct microstructures, arranged from left to right: the weld metal, the heat-affected zone (HAZ), and the unaffected base metal. As expected, the weld metal exhibited a pattern of columnar dendrites, whereas the HAZ displayed grain coarsening and recrystallization.

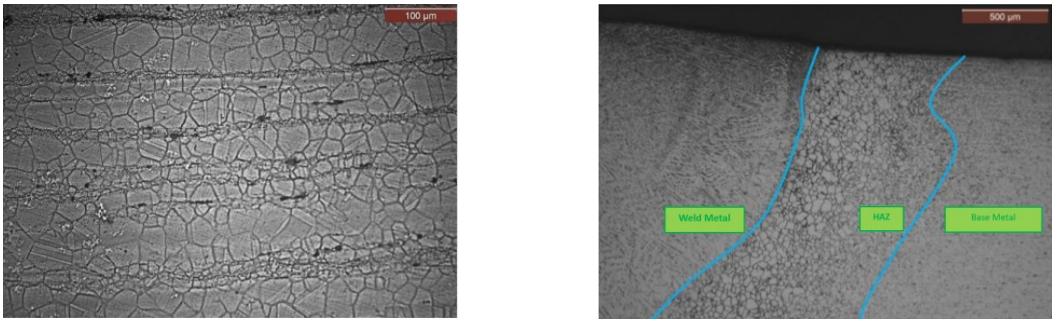

(a) (b)

Figure 18 - Microstructures of bulk (a) and welding (b) of IN625

- **AISI 304 and AISI 316** showed a very similar microstructure in both the base metal and the welded zone, which was also comparable to that observed in IN625. Specifically, the base metal showed austenitic equiaxed grains with recrystallization twins, while the weld metal displayed a columnar dendritic microstructure (Figure 19).

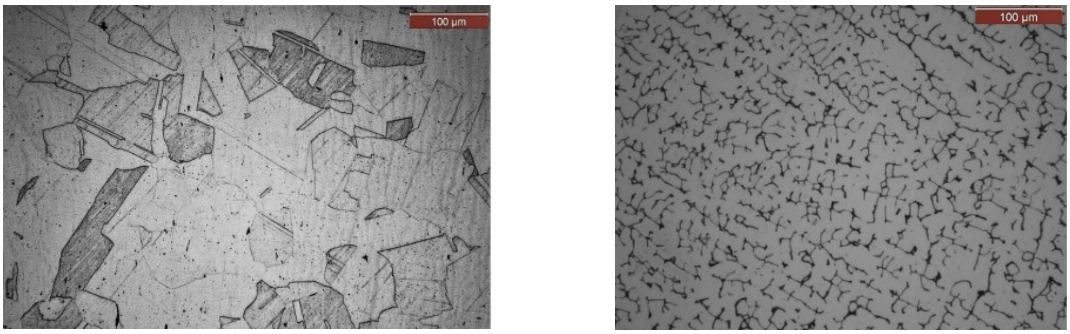

(a) (b)

Figure 19 – Microstructures of bulk (a) and welding (b) of AISI 304 barrel (Kalling 2% etching).

3.2 Surface and cross-section analysis of samples after the exposure to the gas

- **IN625 vessel at 550°C and 48,5 bar in a 50% CO_2 and 50% C_4F_{10} atmosphere**

The surface showed an outer layer rich in carbon, under which corrosion products resulting from exposure to the fluorine-rich mixture had formed (Figure 20).

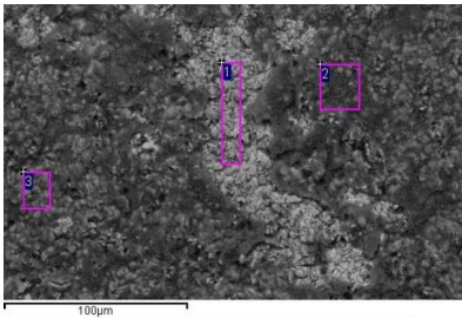

	C	O	F	Al	Cr	Fe	Ni	Mo
1	47.81		31.86		3.15	1.59	14.44	1.15
2	69.11	3.14	14.98	0.23	2.02	0.94	8.13	1.44
3	66.28	2.87	17.37		2.4	0.79	9.11	1.19

Figure 20 - SEM-EDS analysis at the surface of IN625 exposed to 50% CO_2 + 50% C_4F_{10} at 550°C (wt.%)

The cross-section analysis revealed an intergranular attack, but the interaction layer was thin approximately 15-20 µm deep (Figure 21).

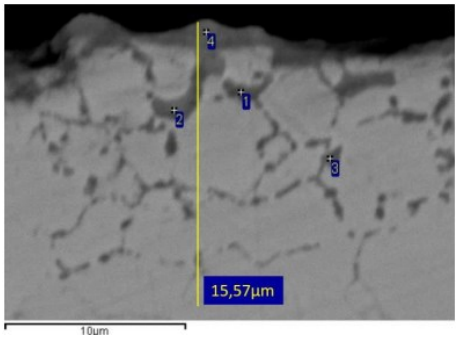

	C	F	Ti	Cr	Fe	Ni	Mo
1	4.80	11.67		10.85	6.8	61.89	3.9
2	6.24	27.87	0.4	12.43	4.5	44.6	3.8
3	3.86	21.09		21.88	2.5	44.74	5.9
4	20.65	15.88		9.27	2.4	46.84	4.8

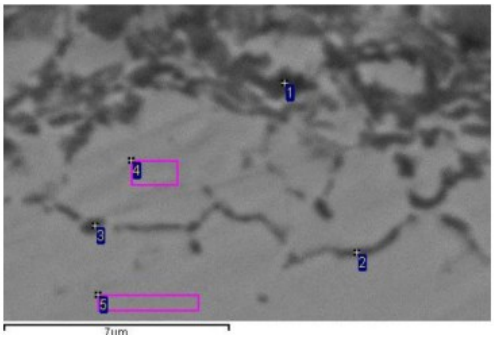

	C	F	Ti	Cr	Fe	Ni	Mo
1	5.2	21.49		18.99	3.56	44.96	5.8
2	7.18	13.16		22.21	2.73	47.38	7.34
3	5.51	14.96		21.54	2.78	49.31	5.91
4	7.28		0.46	21.08	3.35	57.97	9.86
5	7.44			20.97	3.83	58.46	9.3

Figure 21 - SEM-EDS cross-section of IN625 exposed to 50% CO_2 + 50% C_4F_{10} at 550°C (wt.%)

The heat-affected zone of the weldment exhibited long intergranular cracks, extending for hundreds of microns (Figure 22). EDS analysis inside these cracks confirmed the formation of metallic fluorides, indicating that grain boundaries were the preferred sites for fluorine corrosion. EDS analysis at the crack tip revealed high levels of Cr, Ni, and F. The branched nature of the cracks confirmed that they were the result of corrosion instead of being preexisting cracks induced by mechanical or thermal stresses during the vessel manufacturing.

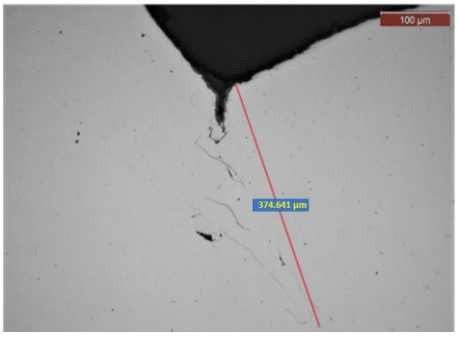

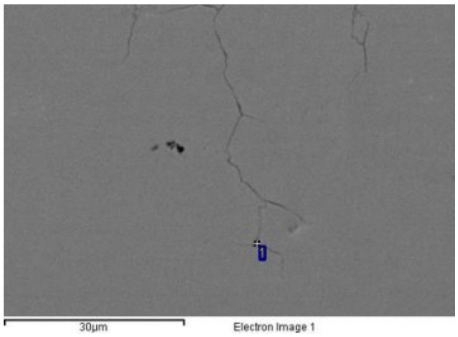

	C	O	F	Cr	Fe	Ni
1	8.92	2.24	11.14	21.54	3.78	52.38

Figure 22– Intergranular crack at HAZ and the chemical composition (wt.%) of its tip of IN625 exposed to 50% CO_2 + 50% C_4F_{10} at 550°C (wt.%)

- **IN625 vessel at 650°C and 46.88 bar in an 80% CO_2 and 20% C_6F_6 atmosphere**
  The surface exhibited a layer containing notable amounts of carbon and fluorine, as depicted in Figure 11. Considering that these elements were the main components of the gas mixture, this layer was likely a result of gas degradation at elevated temperatures favoured by the interaction with the IN625 wall. EDS analysis also detected a minimal quantity of sulphur in a few points (Figure 23).

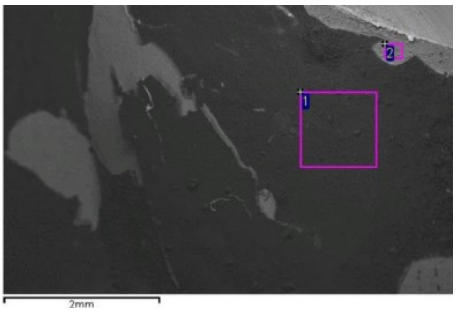

	C	F	S	Cr	Fe	Ni	Mo
1	77.15	10.16	0.78	1.21		9.31	1.39
2	18.62	16.10		16.18	1.65	47.45	

Figure 23 – SEM-EDS analysis at the surface of IN625 exposed to 80% CO_2 + 20% C_6F_6 at 650°C (wt.%)

The sample cross-section showed the presence of an inner layer resulting from the corrosive action by fluorine-containing gas on the 625 alloy (Figure 24). This was a double layer that consists of an incoherent deposit rich in chromium and fluorine in the upper part, likely chromium fluoride (CrF_3) and a second inner layer where the corrosion predominantly occurred along grain boundaries, penetrating selectively to a depth of approximately 70-80 µm. In the weldment the intergranular attack was particularly severe, producing a main crack extending about 4.52 mm into the Heat Affected Zone, with additional branches confined to the HAZ (Figure 25). This area was prone to secondary phase precipitation at grain boundaries and surface irregularities that promote crack propagation. Notably, nickel alloys are susceptible to stress corrosion cracking in fluorine-rich environments like HF, typically displaying an intergranular crack morphology. However, the exposure to 650°C for several hours should relieve any residual stress within the vessel, so the primary corrosion mechanism was likely selective corrosion.

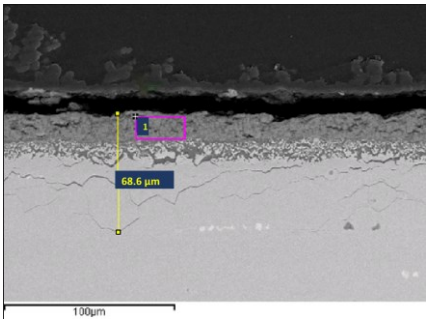

C	F	Cr	Fe	Ni	Mo
13.73	39.6	11.39	3.26	30.56	1.45

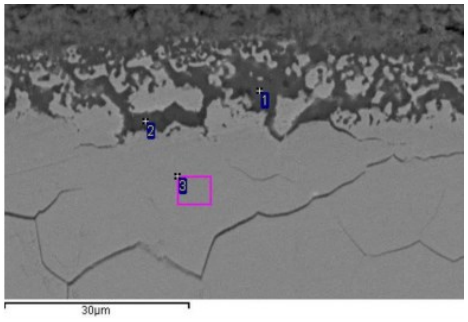

	C	O	F	Al	Ti	Cr	Fe	Ni	Mo
1	6.57	1.14	51.42			37.76	0.39	1.67	1.05
2	6.48	1.32	48.07	0.47	0.41	37.59	0.41	4.21	1.06
3	7.35					21.51	3.47	57.68	9.99

Figure 24 – SEM-EDS cross-section of IN625 exposed to 80% CO_2 and 20% C_6F_6 at 650°C (wt.%)

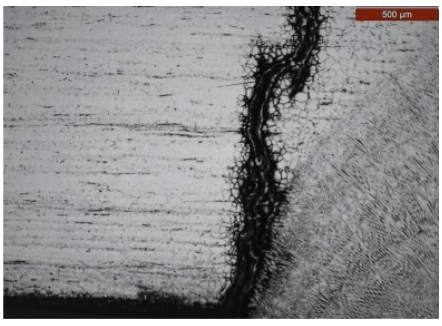

Figure 25– Intergranular crack at the HAZ of IN625 exposed to 80% CO_2 and 20% C_6F_6 at 650°C

This sample and the previous one exhibited similar characteristics, including a dual interaction layer consisting of the same elements but in different percentages, intergranular corrosion and cracks with a branching nature in the heat-affected zone (HAZ). However, in the case of C_4F_{10}, the extent of corrosion is significantly more limited. This could be attributed to the lower gas mixture temperature (550 vs. 650 °C) or the reactivity of the distinct fluorine-bearing compound present in the mixture (C_4F_{10} instead of C_6F_6). Additionally, the fluorides had a different composition, underscoring the substantial influence of temperature and gas composition on both the mechanism and kinetics of fluorine attack.

- **AISI304 vessel at 500°C and 38,7 bar in a pure sCO_2 atmosphere**
  The surface was uniformly covered by a carbon-rich deposit, which also contained oxygen and a relevant quantity of Si (Figure 26). This elevated silicon content had been confirmed through subsequent SEM-EDS analysis the massive presence of silicon had been confirmed. This might be attributed to contamination phenomena.

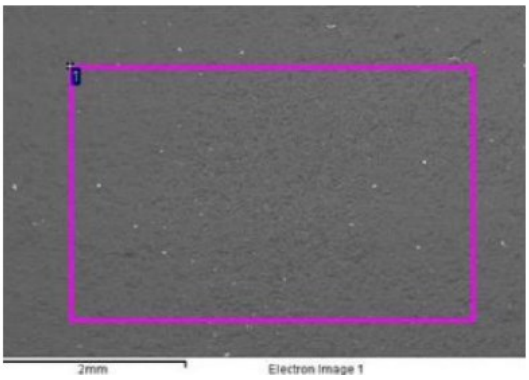

	C	O	Al	Si	Cr	Fe	Ni
1	30.18	26.22	0.57	30.15	3.79	8.69	0.39

Figure 26 - SEM-EDS analysis at the surface of AISI 304 exposed to pure CO_2 at 500°C (wt.%)

The cross-section analysis revealed an interaction layer with a thickness of approximately 6-7 µm (Figure 27). Few internal defects were evident, characterized by an oxide rich in manganese and aluminium, possibly caused by internal selective oxidation. It's noteworthy that the interaction layer formed on the surface of AISI 304 contained a significant amount of silicon and oxygen. This was unusual, since silicon typically in this alloy is at a low concentration (around 1%). One plausible explanation is that supercritical carbon dioxide gradually reacts with the silicon in the stainless steel, forming a layer of silicon oxide mixed with carbon through specific reactions:

$$2CO_2 + Si = 2CO + SiO_2$$

$$2CO = C + CO_2$$

Considering the Boudouard equilibrium, which describes reactions between CO_2 and CO, it confirms that at a temperature of 500°C, the deposition of pyrophoric carbon is the favoured reaction. Referring to relevant literature, Rouillard analysed corrosion layers on an austenitic alloy exposed to sCO_2 at 550°C for 310 hours. He observed an oxide layer enriched in Cr and, below that, a layer enriched in Si. He proposed that the presence of silicon was due to the formation of SiO_2 during the very initial stages of oxidation, which aligns with the observations made in this case after 100 hours at 500°C.

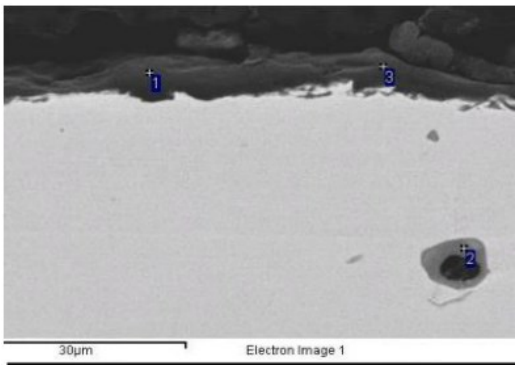

	C	O	Mg	Al	Si	Cr	Mn	Fe
1	42.88	39.93			16.55			0.63
2		41.42	2.92	20.75		12.75	22.15	
3	50.28	35			13.68			1.04

Figure 27- SEM-EDS cross-section of AISI 304 exposed to pure CO_2 at 500°C (wt.%)

Under identical test conditions, an analysis was conducted on another sample from a different vessel exposed to pure CO_2. In this case, the surface remained essentially unchanged. Notably, the presence of a carbon layer was not evident, indicating that pure CO_2 exhibited limited reactivity with the material. However, SEM-EDS analysis identified the existence of a thin oxidation layer, rich in iron oxide, and signs of slight internal oxidation, implying that the oxidation process had initiated after 100 hours (Figure 28).

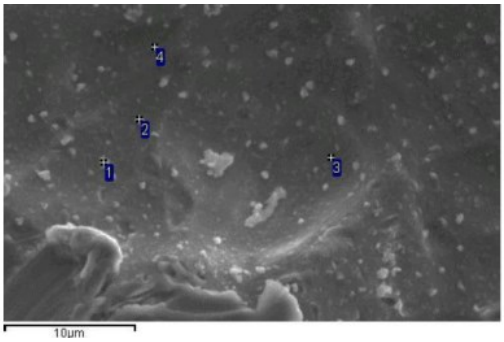

	C	O	Si	Cr	Mn	Fe	Ni
1	4.65	19.04	0.62	12.73	1.27	54.89	6.8
2	4.44	17.25	0.79	13.12	1.27	56.25	6.88
3		4.49	0.36	18.36	1.78	65.51	9.51
4		6.34	0.41	17.44	1.71	67.72	11.39

(a)

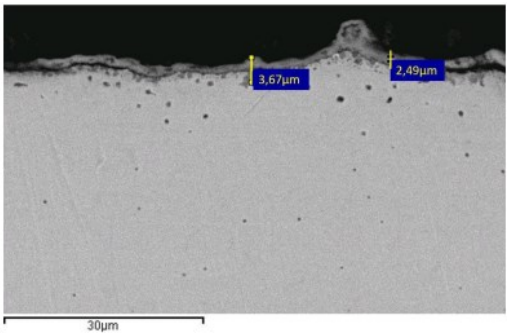

(b)

Figure 28 – Surface (a) and cross-section (b) SEM analysis of AISI 304 exposed to pure CO_2 at 500°C (wt.%)

These results aligned with previous literature that discourages the prolonged use of AISI 304 in pure CO_2 at 500°C.

- **AISI316 vessel at 550°C and 36,44 bar in an 80% CO_2 and 20% C_6F_6 atmosphere**

  The surface revealed a dual-layer interaction, rich in carbon, with a total thickness of approximately 130 µm. On top of this layer, an outer deposit of corrosion products had developed, reaching a thickness exceeding 120 µm. The inner layer, notably thin (around 10 µm in thickness), exhibited signs of intergranular attack.EDS analysis showed the presence of a mix of metallic oxides and fluorides (Figure 29). The corrosion deposit appeared to be partially separated from the substrate, likely due to resin shrinkage during metallographic sample mounting. Beneath the surface, there was evidence of a minor intergranular attack, with a depth of 5-10 µm. Notably, the corrosion products at the grain boundaries

consisted solely of fluorides, with no oxygen found, confirming also in this case that fluorine was the more corrosive element in the fluid.

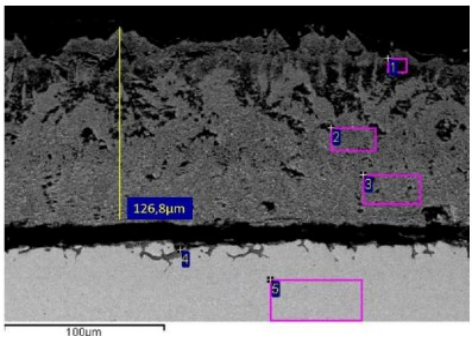

	C	O	F	Si	Cr	Mn	Fe	Ni	Mo
1	40.76	7.04	21.65		6.89		19.02	3.8	0.8
2	12.58	14.14	27.13		9.20	0.6	30.47	3.96	1.8
3	9.12	24.55	12.75	0.6	10	1	35.14	5.39	1.3
4	9.74		51.02	0.2	7.31	0.7	25.61	4	1.3
5				0.7	17.96	1.9	63.08	12.11	4.2

Figure 29- SEM-EDS cross-section of AISI 316 exposed to 80% CO_2 and 20% C_6F_6 at 550°C (wt.%)

It's important to highlight that despite exposing the material to temperatures critical for sensitization (400-800°C) for 100 hours, no intergranular cracks had been observed in the weld.

3.3 Discussion

The metallographic analysis of samples had demonstrated that the introduction of fluorine-bearing organic gases such as C_6F_6 and C_4F_{10} made the CO_2 mixtures highly corrosive to metals at high temperatures. This gas mixture interacted with the vessel surface, resulting in the deposition of carbon-rich compounds and the formation of unprotective metallic fluorides, ultimately leading to corrosion. Notably, there was a lack of literature on the subject, as no previous research had investigated the compatibility of metals with CO_2 and fluorine-containing mixtures. In contrast, the corrosion mechanisms of metals in the presence of pure CO_2 are well-documented for various alloys. In the case of supercritical CO_2 (sCO_2), carbon reacted with metals to form carbides beneath the oxide scale. The severity of the corrosion attack in the gas mixture was observed to increase with temperature, primarily exhibiting intergranular propagation. Temperature appeared to play a crucial role in determining the corrosion rate. However, it's worth noting that an increase in fluoride formation was not solely attributable to temperature but was also influenced by higher fluorine concentrations in the gas mixture. Comparing the corrosion penetration depths for the different samples, it was evident that the IN 625 alloy exhibited greater resistance to fluorine corrosion than AISI 316 and AISI 304 stainless steels. For instance, the 625 alloy displayed a corrosion penetration depth of approximately 70-80 microns, while AISI 316 exhibited more than 120 microns of penetration depth, despite the IN 625 alloy being exposed to a higher temperature (650°C vs. 550°C). On the other hand, the IN 625 alloy had serious issues in weldments. In fact, long intergranular cracks developed in the heat-affected zone of the welds, likely due to the precipitation of second phases at grain boundaries, facilitating the propagation of fluorine corrosion. This phenomenon was not observed in the case of stainless steels.

3.4 Conclusion

From the analysis of sCO_2+perfluorocarbons blends, the following conclusions could be drawn:

- The presence of fluorine significantly increased the corrosiveness of the mixture, resulting in corrosion products rich in fluorine.
- Temperature played a critical role in influencing the corrosion kinetics.
- Corrosion primarily exhibited a uniform pattern with intergranular propagation.
- IN 625 demonstrated greater resistance to corrosion penetration.
- Deep intergranular cracks formed in the heat-affected zone of IN 625 welds.
- Welding in AISI 316 remained undamaged even in presence of fluorine in the fluid.
- There was limited interaction of AISI 304 stainless steel in the presence of pure sCO_2 at a temperature of 500°C.

Hence, IN625 and AISI 316 were considered not suitable materials in contact with an atmosphere containing sCO_2+perfluorocarbons in the considered range of temperatures.

To definitively assessed the effect of fluorine content, two additional tests were carried out at lower temperatures:

- **IN625 at 500°C in an 80%CO_2+20%C_6F_6 atmosphere (case a)**
- **IN625 at 550°C in a 92%CO_2+8%C_6F_6 atmosphere (case b)**

As in the previous case, in this instance, the samples under consideration were taken from the pressure vessel itself. One was used to analyse the base metal, and the other to analyse the welded zone. The same methodology described earlier was followed, but the analysis stopped at optical microscope examination, which proved sufficient to draw some interesting observations.

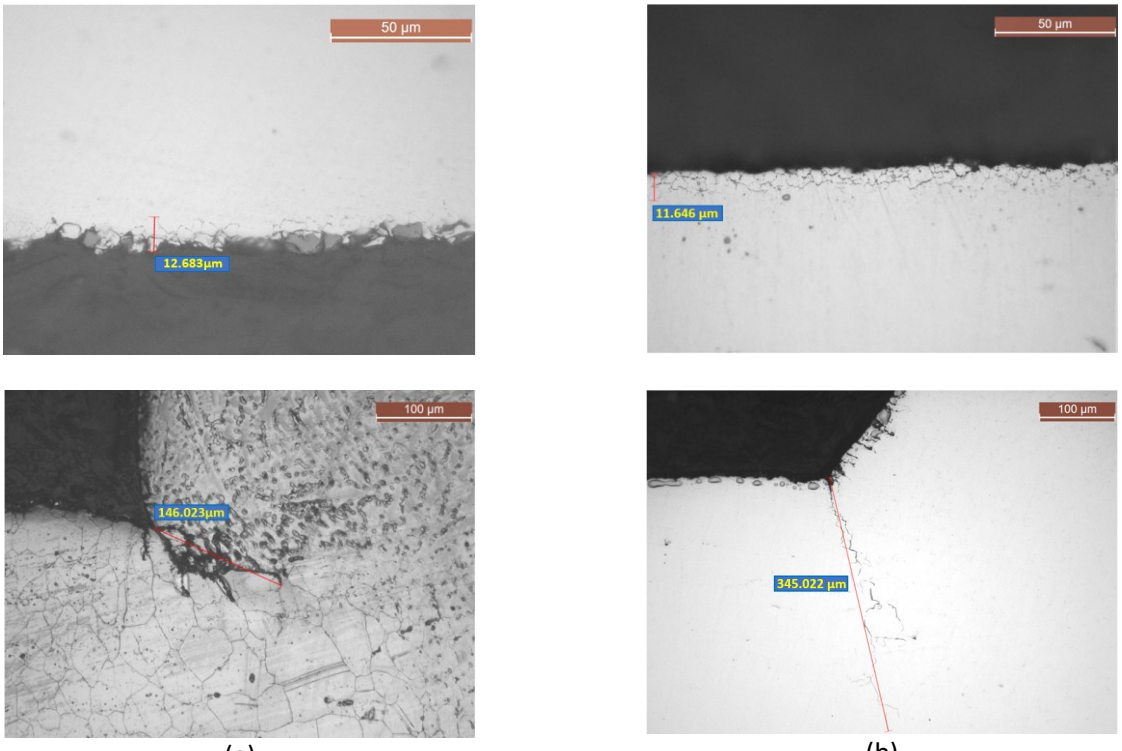

(a) (b)

Figure 30 – Optical microscope analysis of the base metal and the Heat-Affected Zone in the case of IN625 exposed to: (a) 500°C in 80% CO_2 + 20% C_6F_6 and (b) 550°C in 92% CO_2 + 8% C_6F_6

In both cases corrosion on the base metal was intergranular, uniform and comparable in thickness (around 15 µm). Intergranular cracks also appeared in the Heat Affected Zone with a maximum length of 150 µm in case (a) and 350 µm in case (b). As a result, the most relevant factor influencing the corrosion in the presence of perfluorocarbons seems to be the temperature rather than the fluorine content(Figure 30).

CHAPTER 4 PRELIMINARY CORROSION TEST: MATERIALS COMPATIBILITY WITH SUPERCRITICAL CO_2 MIXTURES CONTAINING $SiCl_4$ OR SO_2 DOPANTS

Based on the previous considerations, the use of perfluorocarbons as dopants in sCO_2 mixtures had been discarded. These would not be suitable candidates at all, as despite the relatively small corrosion in the base metal, long cracks developped in the HAZ. Therefore, two other dopants, $SiCl_4$ and SO_2, had been tested. The experimental approach remained the same described previously. In this case, optical microscope analyses were considered sufficient to draw preliminary conclusions. The case studies were:

- **IN625 at 550°C in 80%CO_2+20%$SiCl_4$ atmosphere**
- **IN625 at 600°C in 80%CO_2+20%SO_2 atmosphere**

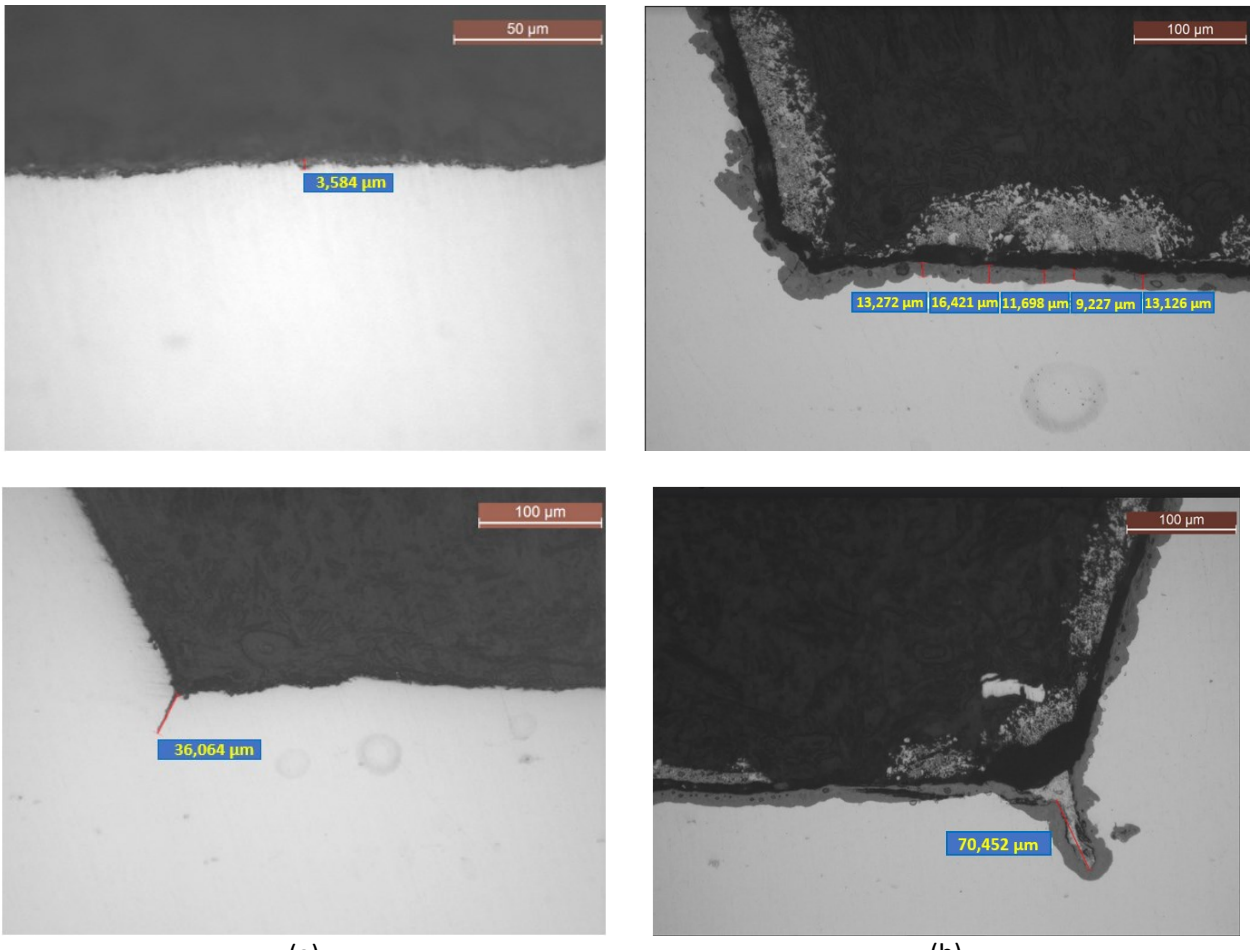

(a) (b)

Figure 31 - Optical microscope analysis of the base metal and the Heat-Affected Zone in the case of IN625 exposed to: (a) 550°C in 80% CO_2 + 20% $SiCl_4$ and (b) 600°C in 80% CO_2 + 20% SO_2

In both cases no intergranular or localized corrosion were detected in the cross-sections (Figure 31). The interaction layer was uniform and had a maximum depth of 5-10 µm. Cracks were still present in the HAZ, but they were very short and likely preexisting because when analysing untested samples, cracks were already there.

Based on these good results, it had been decided to carry out a more in-depth analysis of these specific mixtures, by using a different experimental approach.

CHAPTER 5 FIRST TEST CAMPAIGN: MATERIALS COMPATIBILITY WITH SUPERCRITICAL CO_2 MIXTURES CONTAINING 80%CO2+20%$SiCl_4$ AND 80%CO2+20%SO_2

As previously mentioned, the CO_2+C_6F_6 blend was rejected due to its excessive aggressiveness towards welded IN 625 samples, causing the formation of extensive cracks in the heat-affected zone. Subsequently, a new series of tests was conducted to assess material compatibility with the two other promising fluid combinations previously mentioned: 80%CO_2+20%$SiCl_4$ and 80%CO_2+20%SO_2.

The hot corrosion tests were carried out by setting the test samples inside pressure vessels, which were then filled with the respective gases and maintained at 550°C for specific durations:

1. **80%CO_2+20% $SiCl_4$, 550°C, 547 hours**
2. **80%CO_2+20%SO_2, 550°C, 681 hours.**

At the end of each test, welded barrel was opened by cutting and the rod with the samples and spacers was extracted (Figure 32).

(a) (b)

Figure 32 – The appearance of the rod, spacers and samples exposed at 80%CO_2+20%$SiCl_4$ (a) and 80%CO_2+20%SO_2 (b)

Figure 32 shows that the alumina rod looks dirty and broken after exposure to 80%CO_2+20%$SiCl_4$ while it appears intact and relatively clean when exposed to 80%CO_2+20%SO_2.
Before analysing the samples, a study was also carried out on the weldments of the two vessels made in IN 625.

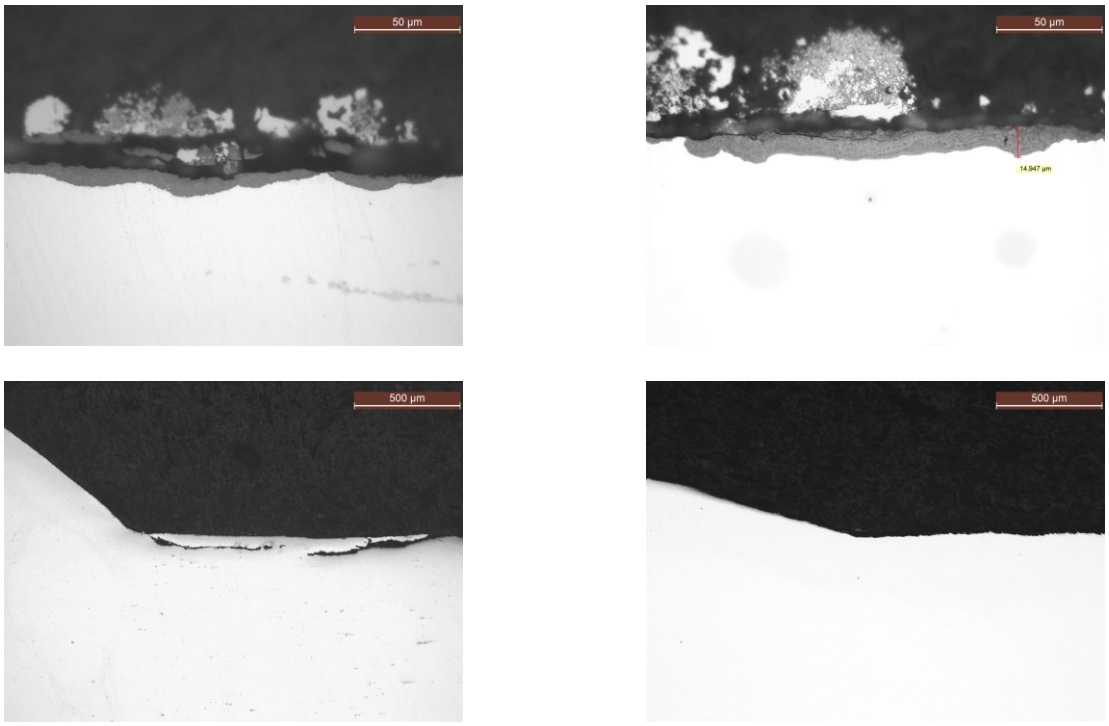

(a) (b)

Figure 33 - Optical analysis of the base metal section and the welded area of the vessel exposed to 80%CO_2+20%$SiCl_4$ (a) and 80%CO_2+20%SO_2 (b).

Figure 33 confirms the preliminary results. For both atmospheres the cross sections showed the presence of a thin uniform interaction layer (<15 microns), without signs of localized or intergranular corrosion. In particular, no cracks were evidenced in the heat-affected zone of the weldments.

5.1 Results of the test carried out with 80%CO_2+20%$SiCl_4$

Table 22 display samples weight changes a after the test carried out in a 80%CO_2+20%$SiCl_4$ environment. The samples remained exposed continuously for 547 hours. Mass gain, measured in mg/cm^2, served as an index of material corrosion (Table 10). Literature suggests that a mass gain of approximately 0.6 mg/cm^2 is acceptable after a similar exposure duration (about 500-600 hours).

Notably, both IN625 samples produced by additive manufacturing exhibited the highest mass gains of the batch, approximately 4-5 times above the acceptable threshold. This indicated substantial interactions between IN625_additive samples and the fluid. Interestingly, the presence of welding did not adversely affect the mass gain outcomes. Conversely, IN625 samples produced by casting or forging displayed lower mass gains. Among these, the forged IN625 samples demonstrated the most promising results, nearly meeting the acceptable threshold. A comparable mass gain (less than 1 mg/cm^2) was also exhibited by forged IN725 and IN718 samples. In contrast, both G130 samples showed an extremely high mass gain (in red in Table 22), two order of magnitude more respect to others, probably explaining the reason of the damage observed in Figure 42. In general, all the samples' pairs exhibited a large scatter of results, likely due to static testing conditions that facilitated the "random" deposition of organic substances released from gas thermal decomposition. This may had led to an overestimation of measured mass gains.

SAMPLES	INITIAL WEIGHT (g)	FINAL WEIGHT (g)	MASS GAIN (mg/cm²)
IN625_additive	26.4406	26.4985	2.97
IN625_additive with weld	26.5756	26.6237	2.48
IN625	26.0871	26.0952	0.42
IN625	26.0851	26.1023	0.88
ASTM A494 CW6MC_IN625	25.7146	25.7268	0.63
ASTM A494 CW6MC_IN625	25.9342	25.9680	1.73
IN718	25.4404	25.4637	1.20
IN718	25.5028	25.5200	0.88
IN725	25.5329	25.5513	0.95
IN725	25.5812	25.5887	0.38
G130	25.0599	28.5296	178.08
G130	25.1266	32.2271	364.42

Table 22 - Test with 80%CO_2+20%$SiCl_4$ – Samples mass gain

To investigate the interaction occurred between the alloys and the fluids, the samples were analysed by optical microscope and SEM-EDS. For each samples' pair, only the worst was considered.
In case of **IN625_additive**, the surface appears covered by a quite uniform deposit containing high percentages of O, Si, Cl, Ni, Cr and Fe, confirming that an intense interaction with the fluid had occurred (Figure 34).

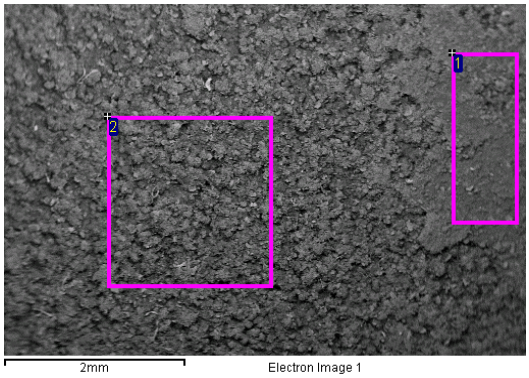

	O	Si	Cl	Cr	Fe	Ni
1	35.53	2.81	34.39	1.40	1.97	23.90
2	46.91	26.83	4.26	16.65		5.35

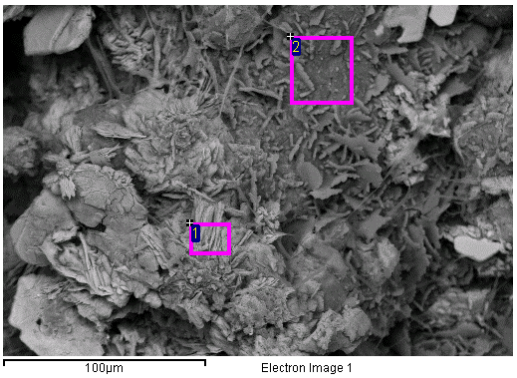

	O	Si	Cl	Cr	Fe	Ni
1	42.99	15.00	17.63	8.89	1.26	14.23
2	40.17	14.05	20.70	4.74	1.33	19.01

Figure 34 – Test with 80%CO_2+20%$SiCl_4$ – SEM-EDS analysis of the surface of IN625_additive (wt.%)

This result was also confirmed by the cross-section analysis.
The images collected by the optical microscope show the presence of a thin interaction layer covering the entire surface of the sample (Figure 35). This layer had a thickness of few microns, suggesting that the relatively large mass gain measured on the sample was also a consequence of gas decomposition products deposited on the surface, implying an overestimation of the measured mass gain.

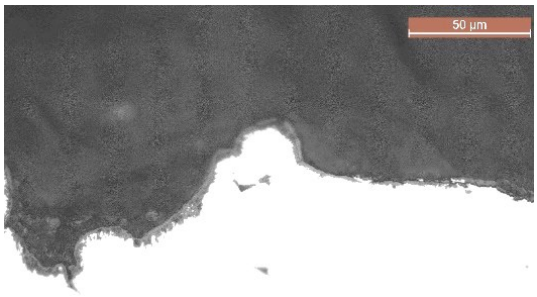

Figure 35 – Test with 80%CO_2+20%$SiCl_4$ – Optical microscope image of IN625_additive

In case of **welded IN625_additive,** as seen for the previous sample, the surface appeared to be covered by a layer O, Si, Cl, Ni and Cr (Figure 36). Few hexagonal crystals rich in Cl, O and Ni were also present. There was no evident difference between the welded area and the base metal.

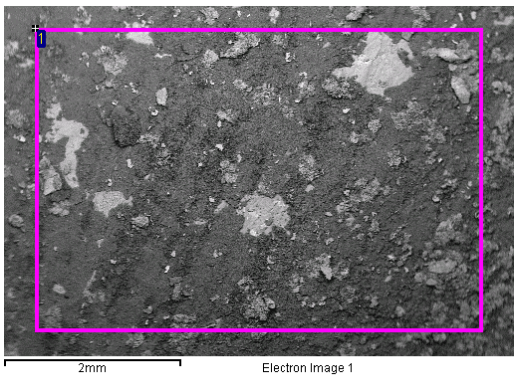

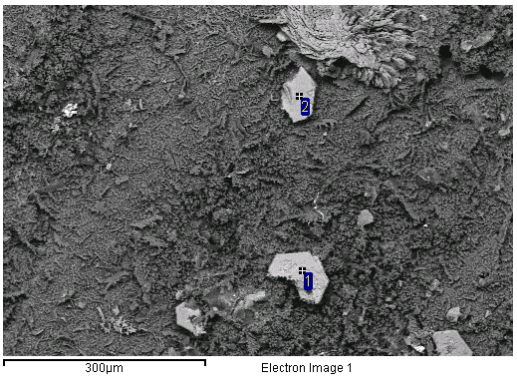

	O	Si	Cl	Cr	Ni
1	49.00	24.86	8.29	8.94	8.90

	O	Si	Cl	Cr	Fe	Co	Ni
1	7.29	0.44	51.82	1.37	3.11	0.53	35.44
2	11.77	2.58	42.95	1.52	3.27	1.10	36.81

Figure 36 – Test with 80%CO_2+20%$SiCl_4$ – SEM-EDS analysis of the surface of sample welded IN625_additive with weld (wt.%)

The images of cross-section collected by optical microscope show only slight interactions between the gas and the material as for the bas material (Figure 37). The only difference was the presence of few porosities in the weld. There was no evidence of localized or intergranular corrosion and there were no cracks in the HAZ.

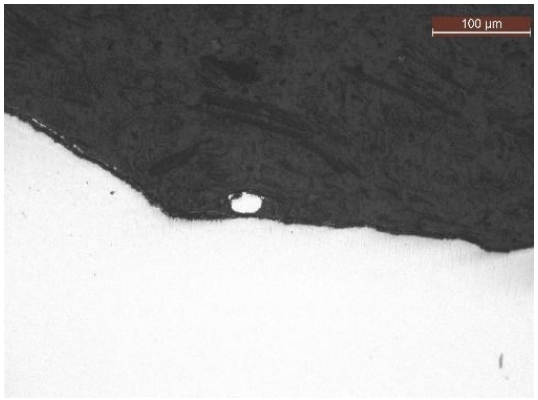

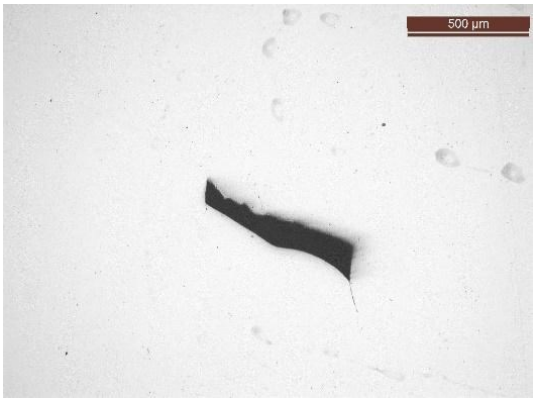

Figure 37 – 80%CO_2+20%$SiCl_4$ – Optical microscope images of IN625_additive with weld

In case of **IN625** made by forging, the surface was covered by a deposit rich in O, Si, Cl, and Ni and isolated particles rich in Cl, O and Ni, as already observed in the previous samples. The parallel finishing lines were still visible. This was a sign that the interaction has occurred, but with limited intensity, confirming the low mass gain of this sample (Figure 38). The images of the cross-section collected by optical microscope confirmed the presence of a slight interaction. In fact, on the entire surface, the sample had an interaction layer that was thinner respect to the IN625 samples realized by additive manufacturing (Figure 38-b).

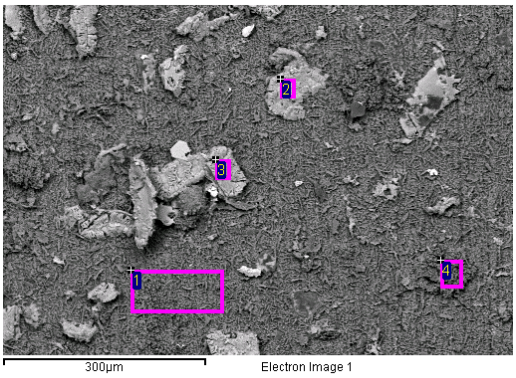

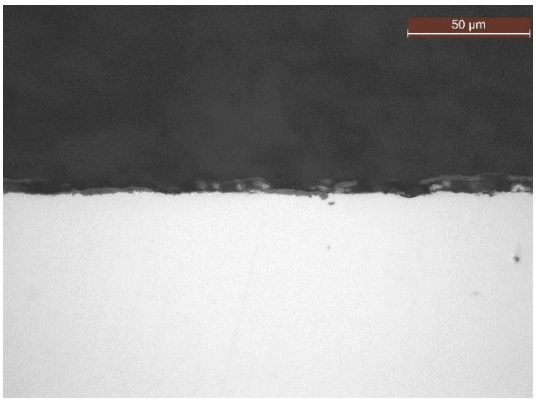

	O	Si	Cl	Cr	Fe	Ni
1	51.80	30.52	3.64	9.65	0.85	3.55
2	18.78	1.30	43.61	1.17	8.27	26.87
3	23.90	0.66	43.12	0.94	8.83	22.55
4	53.34	33.39	5.55	2.13	1.40	4.19

(a) (b)

Figure 38 - Test with 80%CO_2+20%$SiCl_4$ – SEM-EDS analysis of the surface (wt.%) (a) and optical microscope cross-section of IN625 (b)

In case of **ASTM A494 CW6MC_IN625**, as seen for the forged sample, the interaction layer had a thickness in the order of few microns. The chemical composition of the interaction layer closely resembled that observed in the forged sample (Figure 39). The presence of a thin, uniform interaction layer covering the entire surface of the specimen was depicted in Figure 39-b.

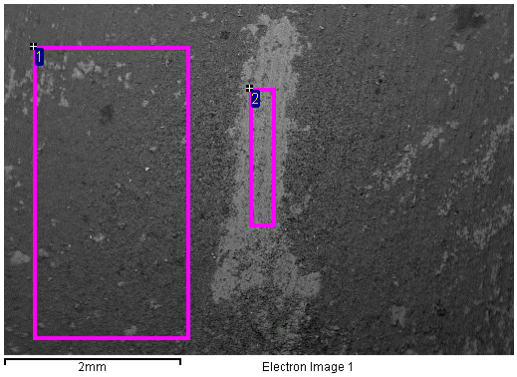

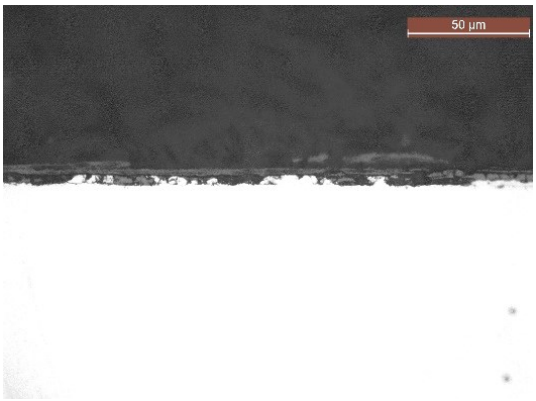

	C	O	Si	Cl	Cr	Fe	Co	Ni	Mo
1		52.64	28.12	5.31	5.04	0.67	0.71	5.72	1.78
2	8.93	39.11	7.16	4.36	29.87		0.74	5.61	4.22

(a) (b)

Figure 39 – Test with 80%CO_2+20%$SiCl_4$ _ SEM-EDS analysis of the surface (wt.%) (a) and optical microscope cross-section of ASTM A494 CW6MC (b)

In case of **IN718,** made by forging, the surface appeared covered by a thin layer rich in Si, Cl, O, Ni and Cr and there were also isolated particles rich in Cl, O and Ni with also small amounts of Fe and Co (Figure 40). The images collected by optical microscope show the presence of a thin interaction layer covering the entire surface, with also a very slight intergranular attack (Figure 40-b).

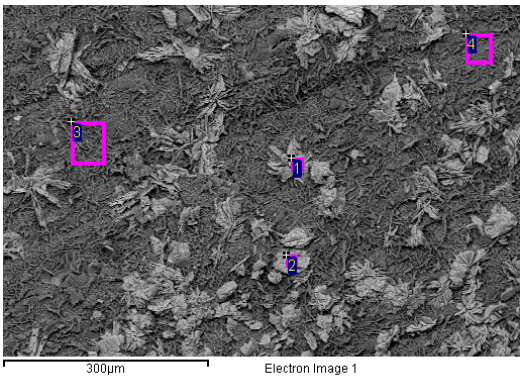

	C	O	Si	Cl	Cr	Fe	Co	Ni
1		26.51	1.87	39.46	1.93	5.77	1.21	23.25
2		20.67	4.39	40.19	1.88	6.91	1.96	24.00
3	6.03	52.74	28.49	2.96	5.46	1.02		3.31
4		53.10	31.52	3.91	6.59	1.19	0.29	3.40

(a)

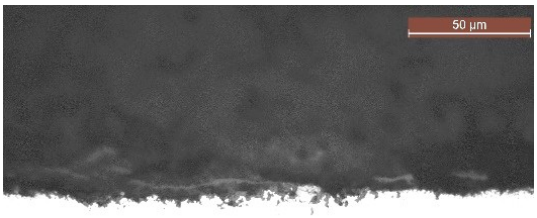

(b)

Figure 40 - Test with 80%CO_2+20%$SiCl_4$ - SEM-EDS analysis of the surface (wt.%) (a) and optical microscope cross-section of IN718 (b)

In the case of **IN725**, the surface was covered with a deposit containing O, Cr, C, Cl, Mo and Nb (Figure 29). At points where the material had been removed, there is a lower percentage of O and Cr and a higher percentage of Cl, Ni and Mo compared to the deposit. The interaction, in this case, was limited, as the finishing lines are still evident. Optical microscope images confirmed the presence of slight interaction. The layer thickness was comparable to what observed in the case of forged IN625 (Figure 41-b).

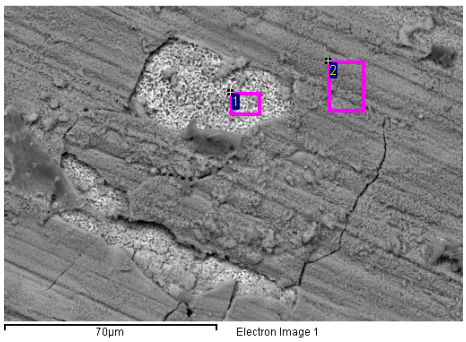

	C	O	Si	Cl	Ti	Cr	Fe	Co	Ni	Nb	Mo
1		15.26		4.57	0.73	8.70	3.25	1.90	53.91		11.68
2	4.88	45.56	0.22	1.62	0.90	37.92	0.32	0.39	2.64	1.78	3.77

(a)

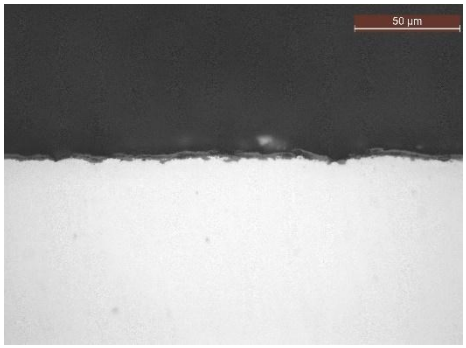

(b)

Figure 41 - Test with 80%CO_2+20%$SiCl_4$ – SEM-EDS analysis of the surface (wt.%) (a) and optical microscope cross-section of IN725 (b)

In the case of the **G130** the surface was covered with a very thick and friable corrosion deposit composed of O, Si, Cl (which are the constituents of the gas) as well as Cr, Co, Ni (Figure 42). Due to the excessive friability of the entire sample, and the handling difficulty, no further analysis had been performed.

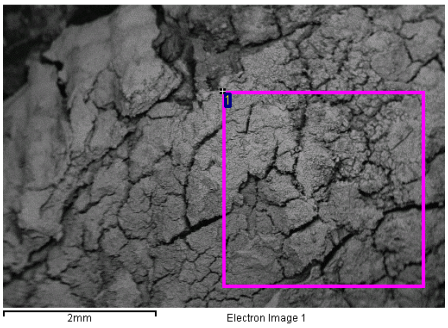

	O	Si	Cl	Cr	Co	Ni
1	9.28	2.67	46.28	3.28	12.74	25.74

Figure 42 - Test with 80%CO_2+20%$SiCl_4$ – SEM-EDS analysis of the surface of G130 (wt.%)

In conclusion, the analysis carried out on the surface and cross-section of IN625 samples realized by additive manufacturing, forging, and casting showed similar interaction layers, notwithstanding the differences evidenced by the mass gain measurements. In all cases, it was evidenced the formation of a layer with a thickness of few microns covering the entire surface, together with small particles rich in Cl, O and Ni.

Similar results were obtained also for the IN718 sample, except for the slight intergranular attack detected under the interaction layer covering the surface.

A thin interaction layer was also present in IN725, but particles were very scarce. The chemical composition of the deposit was approximately the same of other samples, although it contains less O, Si, Cl, and a higher quantity of Cr and Ni. Finally, the G130 was completely disintegrated. The reason was not investigated in detail, but a critical point could be the high content of Co in the alloy composition.

5.2 Results of the test carried out with 80%CO_2+ 20%SO_2

The mass gains of samples exposed to 80%CO_2+20%SO_2, expressed in mg/cm^2, are shown in Table 23. Note that in this case the samples had a continuous exposure to the fluid for 681h.

SAMPLES	INITIAL WEIGHT (g)	FINAL WEIGHT (g)	MASS GAIN (mg/cm^2)
IN625 _additive	26.5395	26.5524	+0.66
IN625_additive with welding	27.1141	27.1344	+1.05
IN625	26.0739	26.0987	+1.27
IN625	26.1163	26.1473	+1.59
ASTM A494 CW6MC	25.9975	26.0214	+1.23
ASTM A494 CW6MC	25.8232	25.8566	+1.71
IN718	25.3787	25.3884	+0.50
IN718	25.3865	25.4008	+0.73
IN725	25.4844	25.4960	+0.60
IN725	25.5549	25.5708	+0.82
G130	25.0687	25.0705	+0.09
G130	25.0551	25.0571	+0.10

Table 23 – Test with 80%CO_2+20%SO_2 – Weighing and mass gain values

Comparing the mass gain values obtained with the $SiCl_4$ mixture, it is evident that the IN625_additive, IN718 and G130 samples exhibited lower values in the SO_2-containing mixture. On the contrary, IN625 showed a lower mass gain in the $SiCl_4$ mixture, while the remaining samples displayed comparable mass gain values.

In particular, the IN718, the IN725 and the IN625_additive samples showed a mass gain close to 0.6 mg/cm^2 that could be considered acceptable according to scientific literature (Table 8).
The ASTM A494 CW6MC and the IN625 made by forging showed a higher mass gain, about twice the critical threshold and the G130 displayed an extremely low mass gain, indicative of minimal interaction with the mixture. In the $SiCl_4$-containing mixture, G130 experienced complete disintegration, resulting in a markedly opposite trend in mass gain.

In 80%CO_2+20%SO_2 the scatter of the results for samples pairs was much smaller than that observed in 80%CO_2+20%$SiCl_4$. Probably, in this case the "random" deposition of gas decomposition products was less important, providing more reliable and repeatable results from mass gain measurements.

The samples were examined by using optical microscope and SEM-EDS to determine the interaction that occurred between the alloys and the fluids. Only the worst case of each samples pair was considered.

The SEM-EDS analysis of **IN625_additive** showed that the surface is covered by an almost uniform interaction deposit containing especially O, S, Ni and Cr, suggesting that some interaction with the gas had occurred (Figure 43).

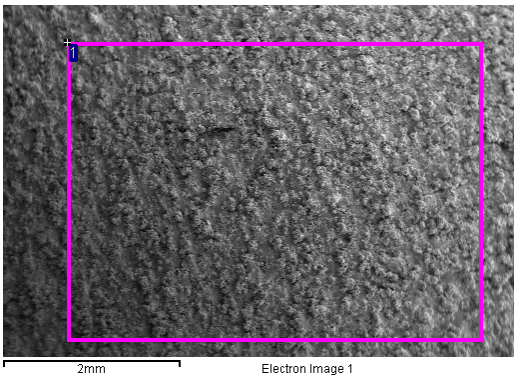

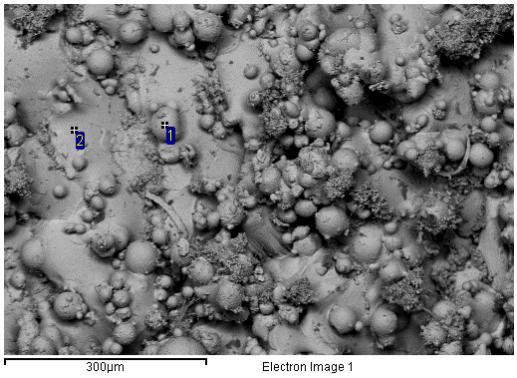

	C	O	Al	S	Cr	Fe	Ni
1	7.03	14.89	1.54	4.45	16.21	0.79	55.10

	C	O	Al	Cr	Fe	Ni	Mo
1	5.23	5.00	0.59	20.37	0.51	59.74	8.56
2	5.55	4.85	1.02	20.35		58.52	9.72

Figure 43 - Test with 80%CO_2+20%SO_2– SEM-EDS analysis of the surface of IN625_additive (wt.%)

This was confirmed by the optical microscope analysis of cross section which shows the presence of a thin interaction layer over the surface of the sample (Figure 44).
It is interesting to observe that the interaction layer was similar or even thicker than the layer observed on the samples exposed to 80%CO_2+20%$SiCl_4$. This seems to confirm that part of the mass gain measured in 80%CO_2+20%$SiCl_4$ was probably due to the deposition of gas decomposition products.

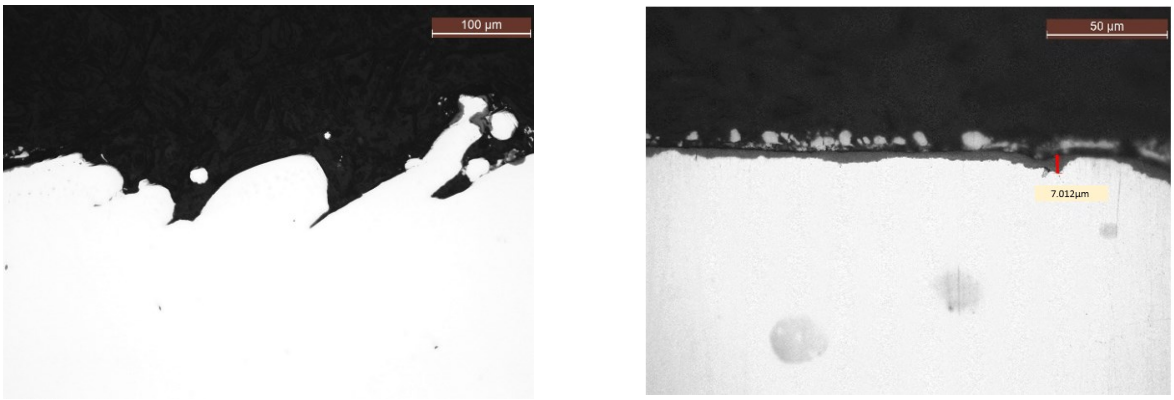

Figure 44 - Test with 80%CO_2+20%SO_2– Optical images of IN625_additive section

The SEM-EDS of cross-section revealed the presence of some localized attack (Figure 33). In these points the interaction layer had an overall thickness of about 25 µm. It consisted of 2 layers: the inner mainly rich in O, Cr, Ni, Nb and Mo, and the outer rich in S, O and Ni (Figure 45).

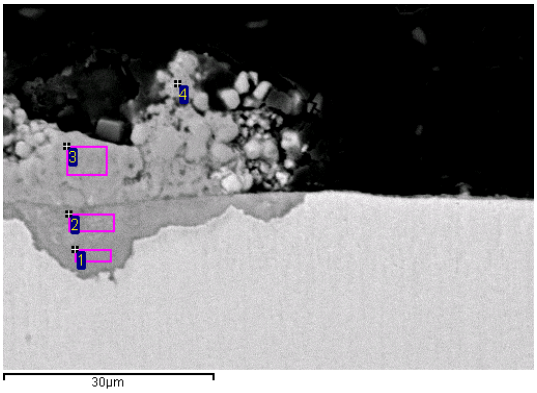

	O	Al	S	Ti	Cr	Fe	Ni	Nb	Mo
1	31.39	0.47	3.69	0.72	32.96	1.4	9.82	6.54	13.00
2	29.16		7.78	0.41	23.29	0.5	23.69	7.25	7.93
3	19.95		10.17		0.48	0.79	68.60		
4	16.57		26.52		7.78		49.14		

Figure 45 - Test with 80%CO_2+20%SO_2- SEM image of cross-section of IN625_additive (wt.%)

The SEM-EDS of **IN625_additive with weld** surface showed a not uniform interaction layer, with some areas covered by very thick deposits (Figure 46). The thick layers had a high content of O, S, C and Ni, suggesting that in these points a larger interaction with the gas had occurred. The presence of these thick layers of corrosion products could explain the higher mass gain of this sample respect to the as built one.

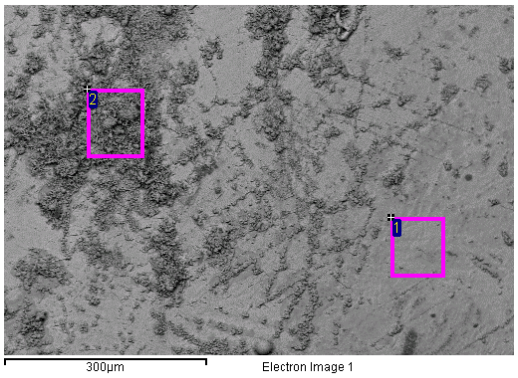

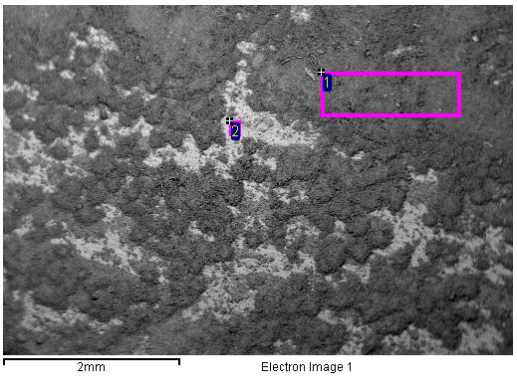

	C	O	Al	S	Ti	Cr	Ni	Mo
1	6.23	20.77	4.95		0.56	15.55	43.43	8.51
2	15.71	19.05	0.44	9.39		5.84	49.57	

	O	Al	S	Ti	Cr	Fe	Ni
1	15.24		13.53				71.23
2	17.31	3.14	3.62	0.40	18.97	0.84	55.72

Figure 46 - Test with 80%CO_2+20%SO_2- SEM-EDS analysis of the surface of sample 625 with weld (wt.%)

The cross-section analysis was carried out by optical microscope and SEM-EDS techniques. The results were presented in Figure 47. The presence of a thin and almost continuous interaction layer was confirmed. There was no evidence of localized or intergranular corrosion and there were no cracks in the HAZ.

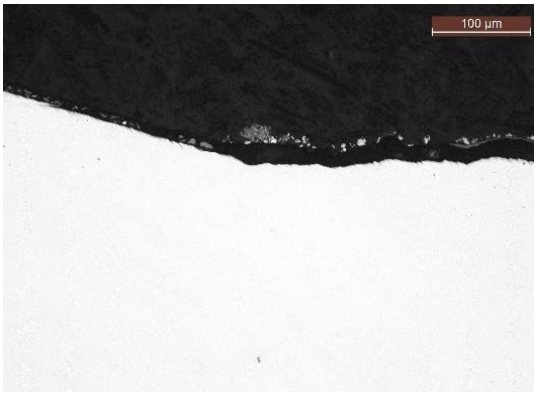

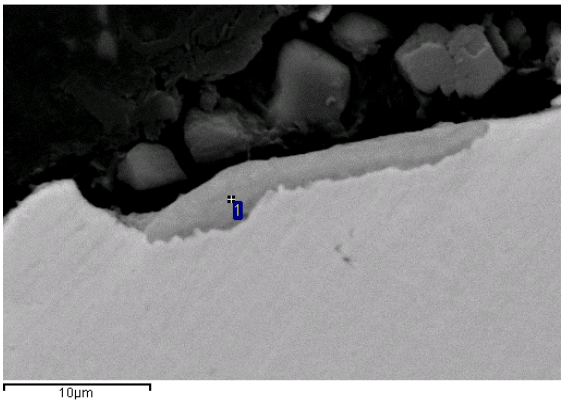

	O	Al	S	Ti	Cr	Ni	Nb	Mo
1	34.44	0.47	3.22	0.52	27.38	12.17	6.10	15.70

(a) (b)

Figure 47 - Test with 80%CO_2+20%SO_2- Optical images of IN625 with weld section SEM image of cross-section (wt.%)

The SEM-EDS analysis of **IN625** sample surface showed the presence of a thick deposit rich in S, O and Ni, which could justify the relatively high mass gain of this sample (Figure 48). The needle-like morphology of the outer interaction layer was associated to a composition rich in S, O and Ni (Figure 48).

The presence of an almost uniform thick interaction layer was also confirmed by the cross-section analysis: a thin layer rich in O, Cr, Mo, Ni and Nb adherent to the substrate, was topped by an outer layer made of coarse particles rich in S and Ni (Figure 49-Figure 50).

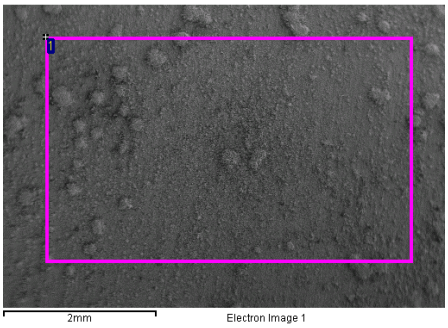

	O	S	Cr	Ni
1	14.89	15.77	3.86	65.48

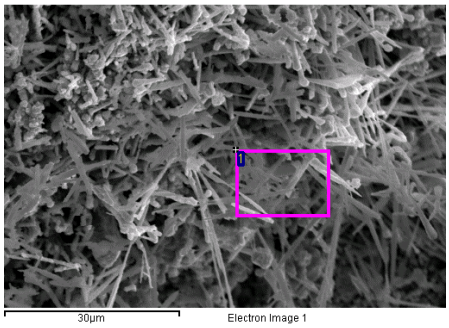

	O	S	Cr	Ni
1	9.29	18.20	0.36	72.15

Figure 48 - Test with 80%CO_2+20%SO_2- SEM-EDS analysis of the surface of sample IN625 (wt.%)

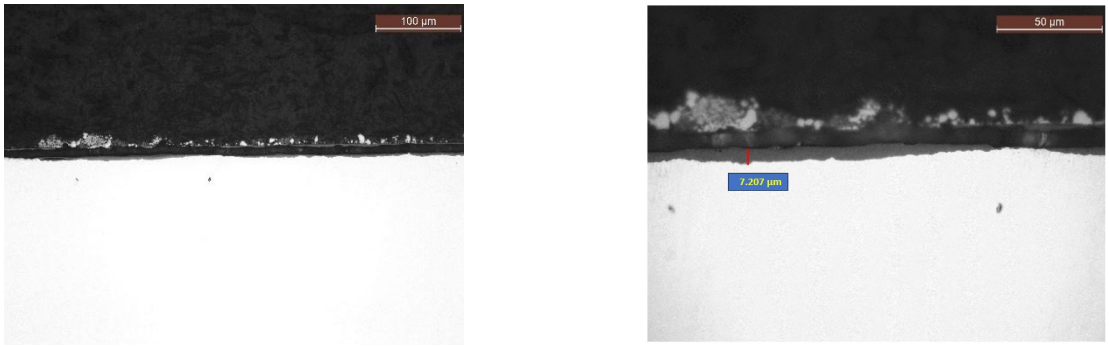

Figure 49 - Test with 80%CO_2+20%SO_2- Optical images of IN625 section

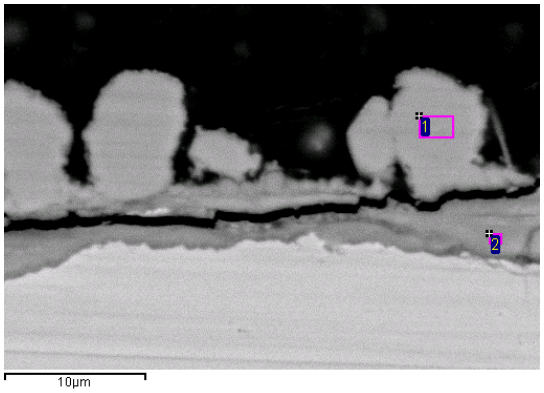

	O	Al	S	Cr	Ni	Nb
1			37.14	0.41	62.45	
2	27.93	1.14	3.83	35.08	8.64	8.84

Figure 50 - Test with 80%CO_2+20%SO_2- SEM image of IN625 cross-section (wt.%)

The SEM-EDS of **ASTM A494 CW6MC** surface showed a uniform deposit rich in O, S, Ni and Cr very similar to the chemical composition observed on the IN625 sample surface (Figure 51). As in the case of the forged sample, optical microscope and SEM-EDS analysis revealed the presence of an interaction layer over the entire surface of the sample. This layer, in many points, was much thicker respect to the IN625 sample (Figure 52). A possible explanation could be that the casting products are frequently more porous than forgings, increasing the effective interaction area. The SEM-EDS cross-section revealed the presence of two layers, with compositions like those of IN625 made by forging or additive manufacturing. Moreover, the cross-section analysis revealed the presence in the microstructure of precipitates rich in Nb and Mo that had been

not identified in the forging or additive manufacturing samples (Figure 53). Additionally, with respect to the same sample tested in 80%CO_2+20%$SiCl_4$, in this case the interaction layer was thicker.

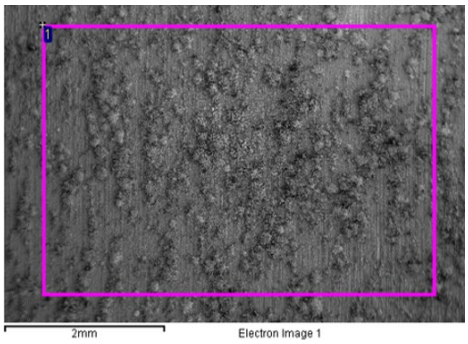

	C	O	S	Cr	Fe	Ni
1	5.06	23.97	8.76	17.21	3.29	41.71

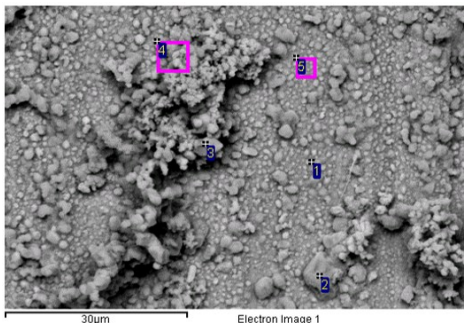

	O	S	Cr	Fe	Ni
1	33.30	2.94	35.81	2.20	25.75
2	30.53	25.59	32.58	3.00	8.30
3	23.90	19.44	6.33	1.10	49.23
4	28.36	13.14	33.04	5.47	19.98
5	30.94	4.78	26.63	2.65	35.00

Figure 51 - Test with 80%CO_2+20%SO_2- SEM-EDS analysis of the surface of ASTM A494 CW6MC (wt.%)

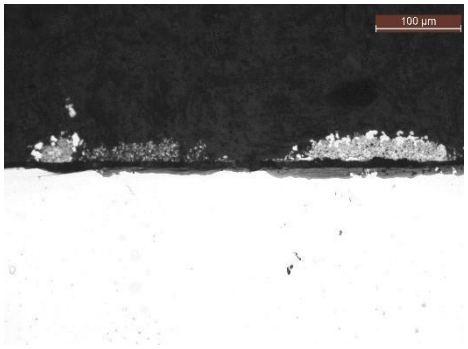

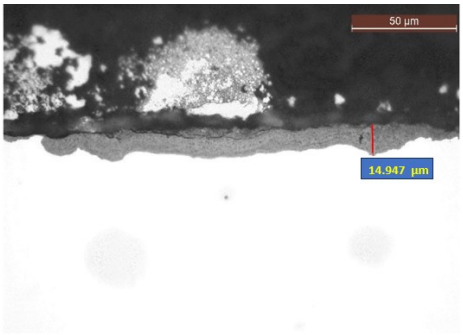

Figure 52 - Test with 80%CO_2+20%SO_2- Optical images of ASTM A494 CW6MC section

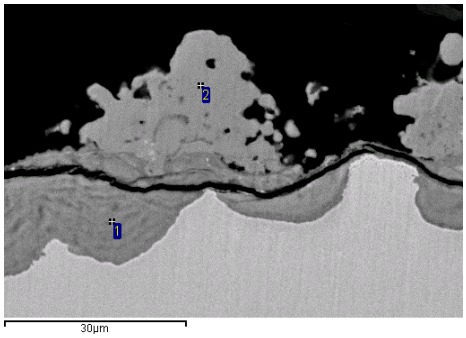

	O	S	Cr	Fe	Ni	Nb	Mo
1	28.05	3.09	36.52	6.03	1.89	7.02	17.40
2		36.55			63.45		

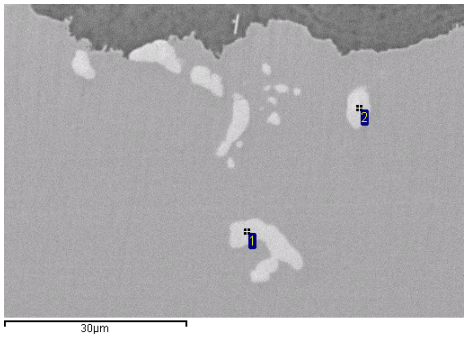

	Si	Cr	Fe	Ni	Nb	Mo
1	0.98	13.98	1.74	26.31	27.69	29.31
2		8.44	1.32	14.72	60.74	14.78

Figure 53 - Test with 80%CO_2+20%SO_2- SEM images of ASTM A494 CW6MC cross-section (wt.%)

In case of **IN718 sample,** the SEM-EDS surface analysis showed the presence of localized corrosion, with the formation of several isolated and rounded particles mainly rich in O, S, Cr, Fe and Ni, on a thin oxide layer rich in O, Ni, Cr and Fe (Figure 54). The optical microscope cross-section confirmed the formation of corrosion

pits having a maximum depth of about 25 µm, topped by a layer rich in O, S, Fe and Ni, for an overall thickness above 50 microns. The corrosion products inside the pit were rich in O and Cr with a small amount of S, Nb and Mo. Out of the pits area, the interaction layer was extremely thin (Figure 55-b).

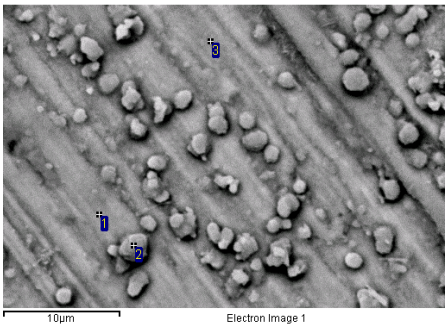

	C	O	Al	S	Ti	Cr	Fe	Ni	Mo
1		27.32	1.36		1.36	16.23	13.39	35.59	4.75
2	4.78	39.35		12.35		30.00	7.89	5.62	
3		21.21	1.30		1.19	19.72	15.71	40.87	

Figure 54 - Test with 80%CO_2+20%SO_2- SEM-EDS analysis of the surface of IN718 (wt.%)

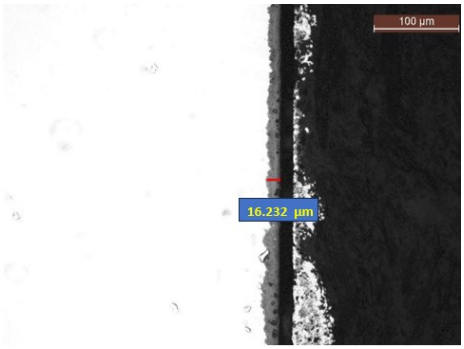

(a)

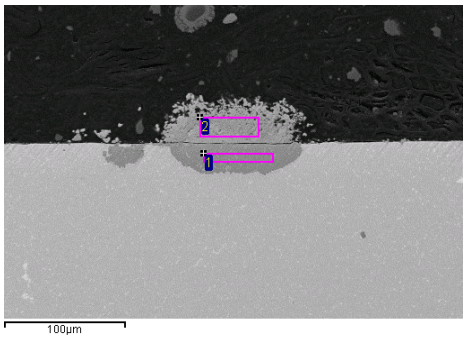

	O	Al	S	Ti	Cr	Fe	Ni	Nb	Mo
1	31.24	0.86	3.76	1.92	29.48	8.7	8.77	8.89	6.39
2	22.86		13.47		0.56	21.56	36.6		4.95

(b)

Figure 55 – Test with 80%CO_2+20%SO_2- Optical images (a) and SEM image of cross-section of IN718 section(wt.%)

The SEM-EDS analysis of the **IN725** surface revealed a non-uniform interaction layer, with a deposit rich in O, S, Ni and Fe, particles identifiable as nickel sulphides and areas where the surface finishing lines were still present (Figure 56). The cross-section analysis carried out by using optical and electron microscopy techniques was presented below. The demonstrated phenomenon is indicative of localized corrosion, consisting of two interaction layers with a combined thickness of approximately 10 µm: the inner layer was rich in O, Cr, Fe, and Mo, while the outer layer was primarily composed of nickel sulphides (Figure 57). This confirms the low mass gain value calculated.

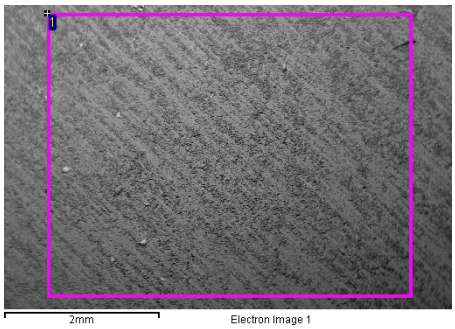

	C	O	S	Ti	Cr	Fe	Ni
1	6.38	24.04	10.31	0.63	17.56	4.87	36.21

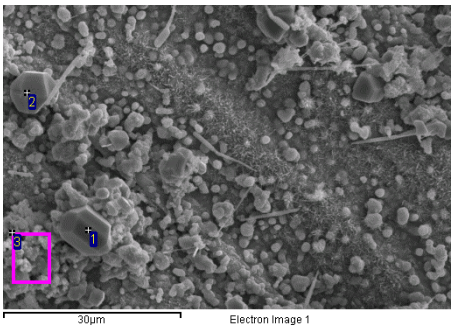

	O	S	Cr	Fe	Ni
1		37.62	0.95	0.79	60.64
2		39.55	1.69	0.50	58.26
3	18.25	9.40	2.35	5.60	64.39

Figure 56 - Test with 80%CO_2+20%SO_2- SEM-EDS analysis of the surface of IN725 (wt.%)

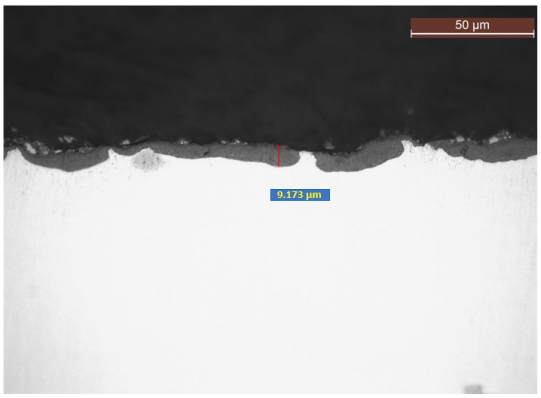

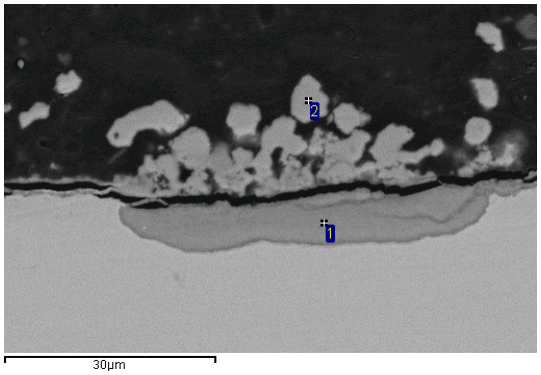

	O	S	Ti	Cr	Fe	Ni	Nb	Mo
1	27.16		2.24	34.48	5.84	2.04	6.9	21.34
2		36.81				63.19		

Figure 57 - Test with 80%CO_2+20%SO_2- Optical images and SEM analysis of the cross-section of IN725 (wt.%)

The SEM-EDS analysis of the **G130** surface revealed a limited interaction with the gas. Only few areas showed the formation of chromium and cobalt oxides, which appeared to be protective. The presence of limited gas interaction was further confirmed by cross-section analyses, which showed a thin interaction layer (<1 micron) rich in oxygen, sulphur, chromium, aluminum, titanium and cobalt (Figure 58-Figure 59).

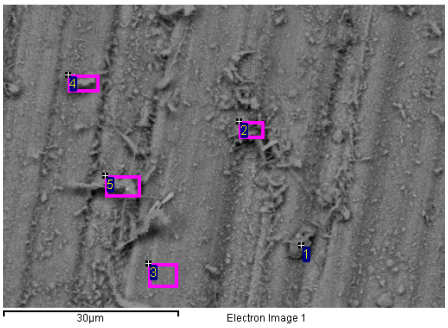

	C	O	Al	Si	S	Ca	Ti	Cr	Mn	Fe	Co	Ni
1	6.27	41.22			4.97	2.28		39.31			2.32	3.63
2	4.34	35.63	0.41	0.46	2.68		0.66	40.62	0.63		4.40	10.17
3	2.75	27.27	1.33	0.41	1.02		1.54	26.91		0.40	12.05	26.33
4	5.08	34.44	1.20	0.59	1.53		1.11	28.57		0.38	8.76	18.34
5	4.55	36.87	1.17		1.71		1.20	32.53			6.45	15.52

Figure 58 - Test with 80%CO_2+20%SO_2- SEM-EDS analysis of the surface of sample G130 (wt.%)

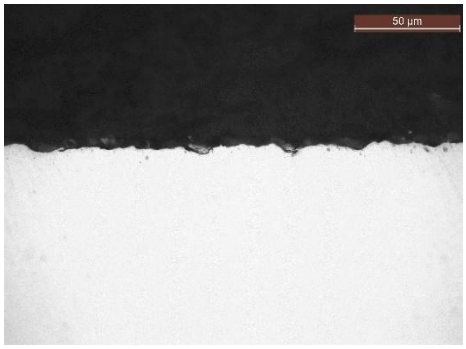

(a)

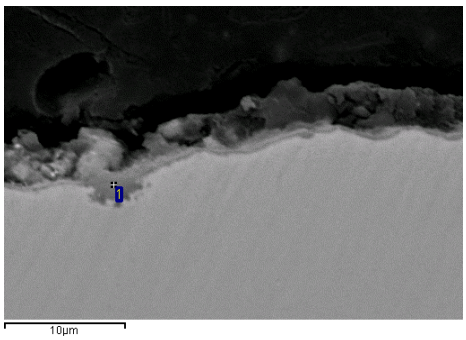

	O	Al	Si	S	Ti	Cr	Co	Ni	Nb
1	34.08	3.48	0.92	11.77	3.29	32.12	5.01	8.32	1.00

(b)

Figure 59 - Test with 80%CO_2+20%SO_2- Optical images (a) and SEM analysis of the surface of G130 section (wt.%)

In conclusion, despite the differences shown by mass gain measurements, the analyses performed on the surface and cross-section of IN625 samples realized by additive manufacturing, forging, and casting revealed some similarities in the composition of interaction layers formed on different samples. In particular, the interaction layer was double with an overall thickness of few tens of microns: the outer layer was especially rich in S and Ni, while the inner one was rich in O, S, Cr and Ni with small amounts of Nb and Mo.

The IN718 samples also showed the formation of a double interaction layer but localized only in the area where occurred the breakdown of the thin protective layer rich in O, Ni, Cr and Fe formed on the surface. The chemical composition of corrosion products in the pits was very similar to the interaction layers formed on the IN625 alloy, except for the higher Fe content.

The IN725 samples exhibited a dual-layer structure in regions affected by localized corrosion. The alloy's chemical composition closely resembled that of previously analysed samples (IN625, IN725, IN718, ASTM A494 CW6MC), for both interaction layers. Notably, when directly comparing with ASTM A494 CW6MC, variations in chemical composition of elements in the corroded area are evident exclusively in the inner layer, marked by an increased concentration of Mo and decreased levels of Cr, Fe, and Nb.

In contrast, the G130 samples surface was covered by only a single layer, which was exceptionally thin, confirming its protective effect and the superior performance, respect to the other samples.

5.3 Final considerations: 80%CO_2+20%$SiCl_4$ vs. 80%CO_2+20%SO_2

Based on the mass gain measurements, it can be inferred that, for most alloys, the corrosive impact of the 80%CO_2+20%$SiCl_4$ blend was greater compared to the 80%CO_2+20%SO_2 one. However, the more detailed analyses performed on samples surface and cross-section reduced this difference.

In the case of 80%CO_2+20%$SiCl_4$ blend, the thickness of the interaction layers formed on **IN625 samples** made by additive manufacturing, forging, and casting was very similar or even smaller respect to 80%CO_2+20%SO_2 for the same samples. This consideration suggests that the mass gain measured on samples exposed to 80%CO_2+20%$SiCl_4$ was overestimated because of a "random" deposition of gas decomposition products. This also could explain the large scatter of data for this batch. About the composition of the interaction layer formed in 80%CO_2+20%$SiCl_4$, all IN625 samples evidenced the formation of a layer with a thickness of few microns covering the entire surface, together with small particles rich in Cl, O and Ni. In case of 80%CO_2+20%SO_2, the interaction layer was double with an overall thickness of few tens of microns. The outer layer was especially rich in S and Ni, while the inner layer is rich in O, S, Cr and Ni with small amounts of Nb and Mo.

In case of **IN718 samples** exposed to 80%CO_2+20%SO_2, notwithstanding the lower mass gain measured respect to 80%CO_2+20%$SiCl_4$, the samples exhibited localized attack, with the formation of pits very deep, covered by voluminous corrosion products (overall thickness of more than 50 microns). On the contrary, in case of 80%CO_2+20%$SiCl_4$ the corrosion of IN718 was shallow and uniform, with only a slight intergranular attack detected under the interaction layer.

In the case of **IN725** exposed to 80%CO_2+20%SO_2, as indicated by the low mass gain, the corrosion was not negligible, being characterized by a double interaction layer in localized areas with an overall thickness of approximately 25 microns. This thickness was comparable to the interaction layer formed in the presence of 80%CO_2+20%$SiCl_4$.

Conversely, in the case of **G130,** the behaviour of the samples had a strong variation depending on the atmosphere considered. When exposed to 80%CO_2+20%$SiCl_4$, the material was completely deteriorated. On the other hand, when exposed to 80%CO_2+20%SO_2, it showed the best performance with the formation of a thin protective oxide layer.

In conclusion, the study showed that at 550°C both 80%CO_2+20%$SiCl_4$ and 80%CO_2+20%SO_2 blends can produce significant interactions with IN718, IN725 and IN625 realized by additive manufacturing, forging and casting.

For all IN625 samples, the attack was quite uniform in both blends and, notwithstanding the mass gain results, the depth of the interaction layer was similar. The welded sample seemed not critical, because no cracks were identified in the HAZ of the weldments, as observed in other fluids as CO_2+C_6F_6.

For IN718 samples, in 80%CO_2+20%$SiCl_4$the corrosion was quite uniform except for a slight superficial intergranular attack, on the other hand, in 80%CO_2+20%SO_2 localized corrosion was detected with the formation of corrosion pits very deep.

For the IN725 samples, the thickness of the interaction layer was approximately similar, although it was more localized in the case of 80%CO_2+20%SO_2. The sample surface exhibited noticeable differences, with material detachment evident in the case of 80% CO_2+20% $SiCl_4$, a phenomenon absented in the mixture containing SO_2.

Based on the presented results, notably the substantial interaction observed in the G130 samples exposed to 80% CO_2 + 20% $SiCl_4$ and considering the prevailing focus in the literature on the SO_2-containing mixture over the $SiCl_4$-containing one, a decision had been made to undertake a more thorough analysis of the mixture containing SO_2.

CHAPTER 6 SECOND TEST CAMPAIGN RESULTS ON THE COMPATIBILITY PRIMARILY OF MIXTURES CONTAINING $80\%CO_2+20\%SO_2$

As previously mentioned, the high-temperature corrosion tests were carried out by setting the samples inside two flanged (removable) pressure vessels, one maintained at 120°C and the other at 550°C. These vessels were filled with an $80\%CO_2+20\%SO_2$ mixture for an overall duration of 2000 hours (Figure 60). The testing procedure involved periodically removing the samples from the pressure vessels, typically at intervals of around 600 hours, and weighing them by using a four-decimal-place Gibertini E42-B balance to assess the weight gain/loss relative to the initial value. After weighing, the samples were reinserted into the vessel. This approach allowed for the examination of the corrosion process over time for both bulk samples and coated samples subjected to the test. For clarity, it is important to note that within this second experimental campaign, the analyses include not only the calculation of "mass gain," a parameter commonly used in literature to assess corrosion levels and determined based on the sample's weight variation but also the use of a stereomicroscope to validate the "mass gain" measurements and ensure the absence of gas decomposition products on the sample surface. Additionally, optical microscopy was employed for microstructural analysis and measurement of the interaction layer, while SEM was applied on both the sample surface and cross-sections to investigate high-temperature corrosion mechanisms occurred on the alloys, identifying the chemical composition of the corrosion deposit and the involved phases. For specific details on the test performed on each sample, refer to Table 18.

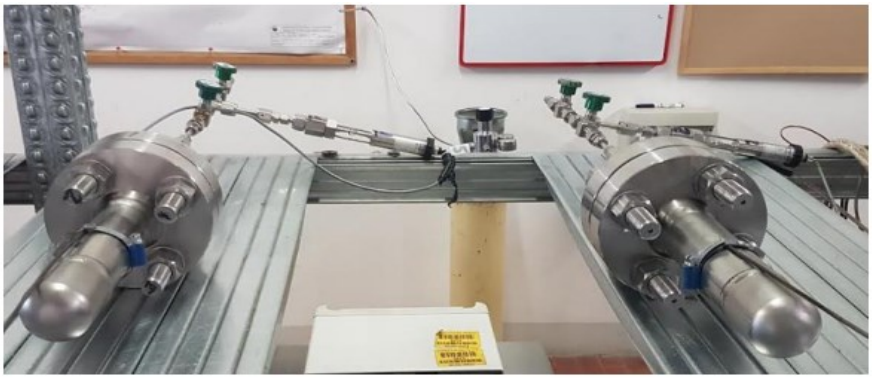

Figure 60 –Test Set-up

6.1 Results of the test carried out at 120°C

The results of the test conducted at 120°C are summarized in Table 24, which shows the weight values of different samples. It's worth noting that for Floma 200, reinforced PTFE in sand colour, and pure PTFE in white colour samples, there was only one exposure for 800 hours. From these results, the mass gain in mg/cm^2 was calculated (Table 25).

In general, it could be observed that there were minimal changes in weight for all samples. Particularly, after the first 600 hours, the mass gains were even negative, possibly due to moisture loss from the samples and/or minor drift in the calibration of the used balance. After 1200 hours, the mass loss of the samples decreased, and after 2000 hours, in many cases, a small weight gain was observed. This suggested that there was a gradual interaction between the samples and the mixture, but it was extremely limited in all cases.

At the end of the test, sample ASTM A216 WCB showed the highest mass gain, equal to 0.0831 mg/cm^2, although other samples of the same type recorded negative gain values even after 2000 hours. Negative gain values were also measured for the two ASTM A494 CW6MC samples and the two SiO2 by PECVD samples.

Therefore, it could be concluded that in all cases, including samples tested only 800 hours, the interaction with the mixture at 120°C was extremely limited.

Samples add at the beginning of the test (total exposure of 2000h)				
Sample	**Initial weight (g)**	**Weight after 600h (g)**	**Weight after 1200h (g)**	**Weight after 2000h (g)**
IN725	28.0789	28.0777	28.0784	28.0793
IN 725	28.1322	28.1308	28.1322	28.1325
ASTM A216 WCB	23.7365	23.7354	23.7366	23.7381
ASTM A216 WCB	23.6351	23.6331	23.6345	23.6357
ASTM A216 WCB	23.6979	23.6946	23.696	23.697
ASTM A216 WCB	23.4033	23.4008	23.4025	23.4042
ASTM A216 WCB	24.205	24.2036	24.2055	24.2064
ASTM A216 WCB	23.6001	23.5963	23.5978	23.5988
AlCrO by PVD	23.9754	23.9745	23.975	23.9766
AlCrO by PVD	23.9293	23.929	23.9297	23.9301
ASTM A494 CW6MC	25.8942	25.8921	25.8936	25.8941
ASTM A494 CW6MC	26.0097	26.0076	26.0093	26.0094
X22CRMOV12	23.7555	23.7525	23.7538	23.7558
X22CRMOV12	23.7673	23.7633	23.7652	23.7681
SiO2 by PECVD SiO_2	23.7702	23.7694	23.7682	23.7685
SiO2 by PECVD SiO_2	23.7794	23.7783	23.7778	23.7787
Carbonitrided	23.9348	23.9341	23.9343	23.9353
Carbonitrided	23.9567	23.9547	23.9568	23.9571
Samples add after 1200h (total exposure of 800h)				
Sample add after 1200h		**Initial weight (g)**		**Weight after 800 h (g)**
Floma 200		26.665		26.6655
Reinforced PTFE (sand color)		0.7876		0.7883
Pure PTFE (white color)		0.5192		0.5194

Table 24 – Test at 120°C - Weighing values

Samples add at the beginning of the test (total exposure of 2000h)			
Sample	**mg/cm² (600h)**	**mg/cm² (1200h)**	**mg/cm² (2000h)**
IN 725	-0.04	-0.02	+0.01
IN 725	-0.05	+0.00	+0.01
ASTM A216 WCB	-0.05	+0.00	+0.083
ASTM A216 WCB	-0.10	-0.03	+0.03
ASTM A216 WCB	-0.16	-0.09	-0.04
ASTM A216 WCB	-0.12	-0.04	+0.0
ASTM A216 WCB	-0.07	+0.02	+0.07
ASTM A216 WCB	-0.19	-0.11	-0.06
AlCrO by PVD	-0.04	-0.02	+0.06
AlCrO by PVD	-0.01	+0.02	+0.04
ASTM A494 CW6MC	-0.10	-0.03	-0.00
ASTM A494 CW6MC	-0.10	-0.0206	-0.01
X22CRMOV12	-0.15	-0.08	+0.01
X22CRMOV12	-0.20	-0.10	+0.04
SiO2 by PECVD SiO_2	-0.04	-0.10	-0.08
SiO2 by PECVD SiO_2	-0.05	-0.08	-0.03
Carbonitrided	-0.03	-0.02	+0.02
Carbonitrided	-0.10	0.00	+0.02
Samples add after 1200h (total exposure of 800h)			
Sample add after 1200h		**mg/cm² (800h)**	
Floma 200		0.00	
Reinforced PTFE (sand color)		0.01	
Pure PTFE (white color)		0.00	

Table 25 - Test at 120°C – Mass gain

To verify these conclusions, drawn from the weight measurements, the samples tested at 120°C were observed under a stereomicroscope. In all cases, images captured at low magnifications did not show clear signs of damage (Figure 61). Only in the case of samples ASTM A216 WCB and IN725, it was detected the presence of some deposits, localized in a few areas and extremely superficial.

Sample	**Stereomicroscope images**
X22CrMoV12 2000h	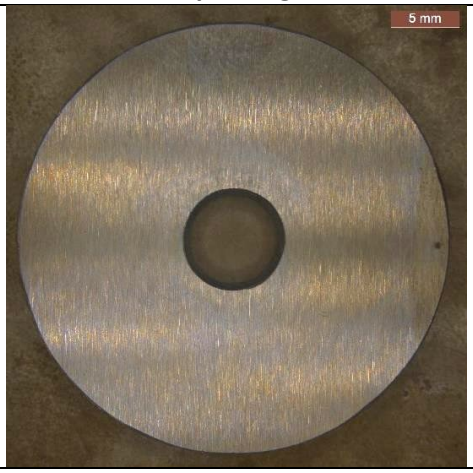

ASTM A216 WCB 2000h	 
IN725 2000h	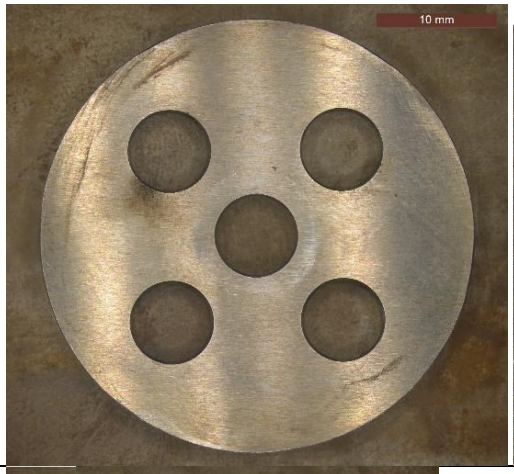 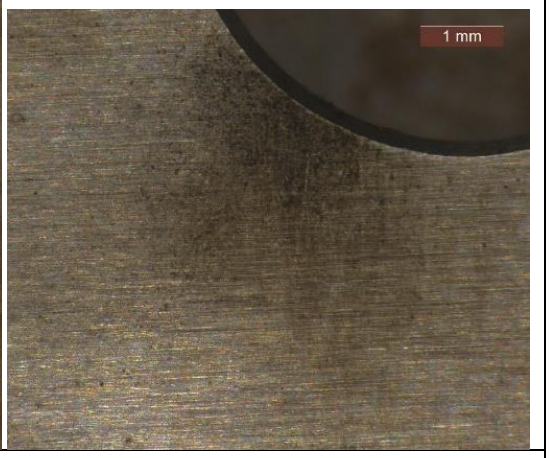
ASTMA494 CW6MC 2000h	
Floma 200 800h	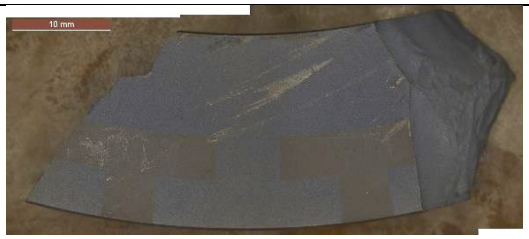
Reinforced PTFE sand color 800h	

Pure PTFE white color 800h	
AlCrO by PVD 2000h	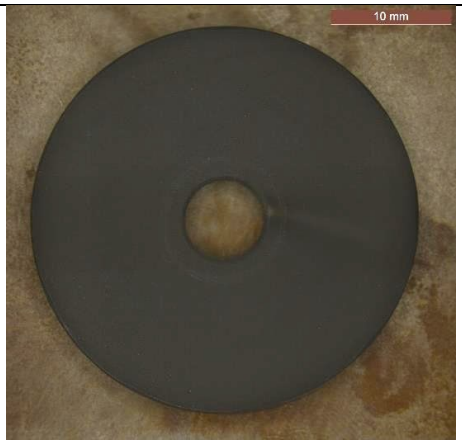
Carbonitrided 2000h	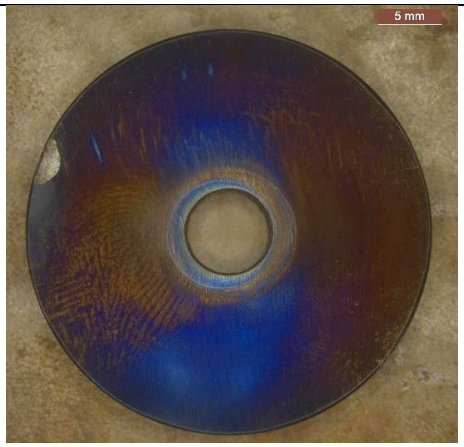
SiO2 by PECVD 2000h	

Figure 61 - Images under a stereomicroscope of the samples tested at 120°C

A surface analysis was also conducted by using SEM for ASTM A216 WCB and IN725 to identify the main elements in the deposits.

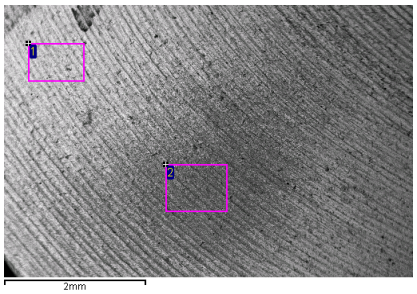

	O	Si	S	Cl	Ca	Cr	Mn	Fe
1	14.81	0.40	3.40		0.37		1.64	79.38
2	30.60	0.51	8.82	1.31	0.69	0.30	0.93	56.85

(a)

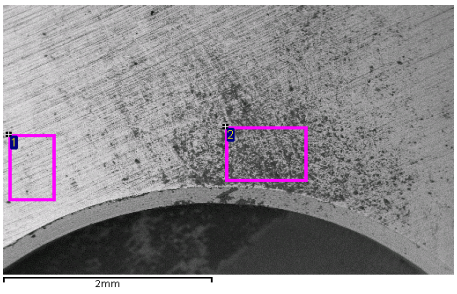

	C	O	Na	Mg	Al	Si	S	Cl	Ca	Ti	Cr	Fe	Ni	Nb	Mo
1	18.18	11.94					2.00			0.99	15.35	6.65	38.46	1.53	4.91
2	20.60	26.10	0.90	0.31	0.44	0.82	7.14	0.57	2.44	0.74	9.37	6.26	20.26	1.13	2.92

(b)

Figure 62 – Test at 120°C - analysis of the constituents of the deposit on ASTM A216 WCB (a) and on IN725 (b)

In both cases minimal surface interaction was observed, and the finishing lines remain visible. The deposits consisted of different elements (Figure 62). For ASTM A216 WCB, elements such as O, S and Fe were present, while for IN725, in addition to O, S, Fe, also significant amounts of C, Cr, Ni and traces of Nb and Mo were detected.

6.2 Results of the test carried out at 550°C

Table 26 presented the mass measurements of different samples for the test conducted at 550°C. It's worth noting that the IN718 and CrNO by PVD samples had two exposures of 600 and 1200h while the Waspaloy samples had a single exposure of 800 h. From these data the mass gain was calculated, expressed in mg/cm^2 (Table 27).

Samples add at the beginning of the test (total exposure of 2000h)				
Sample	**Initial weight (g)**	**Weight after 600h (g)**	**Weight after 1200h (g)**	**Weight after 2000h (g)**
IN725 1	28.0768	28.0866	28.09	28.09
IN725 2	28.0789	28.0895	28.09	28.10
625 additive with weld	27.3317	27.3623	27.36	27.38
625 additive	26.4172	26.4745	26.49	26.54
718 additive with weld	27.2118	27.2329	27.23	27.24
718 additive	25.9966	26.0141	26.01	26.02
G130	25.1611	25.1613	25.16	25.16
G130	24.9356	24.9367	24.93	Removed after 1200h
G130	25.1088	25.1089	25.11	25.11
Carbonitrided	23.8757	24.3168	Removed after 600h	Removed after 600h
CAronitrided	23.927	24.2957	Removed after 600h	Removed after 600h
AlCrO by PVD	23.9682	23.9675	23.96	23.96
AlCrO by PVD	23.9659	23.9636	23.96	23.96
SiO2 by PECVD	23.754	23.8243	23.86	23.90
SiO2 by PECVD	23.806	23.8845	23.92	23.97
IN718	25.5269	25.5805	25.58	Removed after 1200h
IN718	25.5747	25.6574	25.66	25.66
IN718	25.5043	25.586	Removed after 600h	Removed after 600h
Samples add after 600h (total exposure of 1400h)				
Samples add after 600h	**Initial weight (g)**	**Weight after 600h (g)**	**Weight after 1400h (g)**	
IN718	25.3927	25.4971	25.5088	
CrNO by PVD 1	23.9397	23.94	23.9423	
CrNO by PVD2	23.9496	23.9443	23.9447	
Samples add after 1200h (total exposure of 800h)				
Samples add after 1200h	**Initial weight (g)**	**Weight after 800h (g)**		
Waspaloy	25.223	25.226		
Waspaloy	25.1086	25.112		

Table 26 – Test at 550°C - Weighing values

Samples add at the beginning of the test (total exposure of 2000h)			
Sample	**mg/cm² (600h)**	**mg/cm² (1200h)**	**mg/cm² (2000h)**
IN725	0.40	0.66	0.72
IN725	0.43	0.53	1.06
625 additive with weld	1.57	1.86	2.62
625 additive	2.93	3.96	6.29
718 additive with weld	1.06	1.36	1.71
718 additive	0.86	1.04	1.24
G130	0.01	0.17	0.17
G130	0.05	0.09	X
G130	0.00	0.08	0.12
Carbonitrided	22.68	X	X
Carbonitrided	18.96	X	X
AlCrO by PVD	-0.035	0.00	0.02
AlCrO by PVD	-0.12	0.03	0.08
SiO2 by PECVD	3.6	5.55	7.53
SiO2 by PECVD	4.04	6.19	8.44
718	2.75	2.94	X
718	4.25	4.67	4.82
718	4.20	X	X

Samples add after 600h (total exposure of 1400h)		
Samples add after 600h	**mg/cm² (600h)**	**mg/cm² (1400h)**
718	5.34	5.94
CrNO by PVD	0.01	0.13
CrNO by PVD	-0.27	-0.25

Samples add after 1200h (total exposure of 800h)	
Samples add after 1200h	**mg/cm² (800h)**
Waspaloy	0.15
Waspaloy	0.17

Table 27 – Test at 550°C – Mass gain

At 550°C, in most cases, the mass gains were quite significant after just 600 hours of exposure, confirming the increased aggressiveness of the 80%CO_2+20%SO_2 mixture as the temperature rises. When considering the final mass gain value at 2000 hours, it became evident that the best performing alloys were, in order of importance, the two nickel superalloys G130 and Waspaloy, both characterized by a significant amount of Co in the alloy composition. The superior performance of these alloys when in contact with high-temperature mixtures containing SO_2 could be justified considering a dated study from the 1970s [164]. According to this study, sulfurization of cobalt in the presence of sulfur vapors follows a parabolic law, governed by the outward diffusion rate of cobalt ions. Specifically, the reaction rate of cobalt in sulfur-rich atmospheres is considerably lower than that of Ni and Fe. Furthermore, it was reported that the addition of Cr is beneficial in the presence of H_2S, while the addition of Al is detrimental. It is worth noting that the G130 alloy has a higher content of Co and Cr compared to the Waspaloy alloy. In summary, both G130 and Waspaloy gave good results. A direct comparison between the two alloys is quite difficult since the exposure times for the two samples were different. (2000 hours for G130 for and only 800 hours for Waspaloy). Anyway, the lower mass gain of G130 demonstrates its superior performance over Waspaloy. This result can be explained considering the higher content of Co and Cr of G130, as already mentioned in literature

As for the coatings, the most resistant ones, in order of significance, were **AlCrO by PVD and CrNO by PVD.**

The CrNO by PVD coating was considered less protective than the AlCrO by PVD coating because CrNO by PVD samples 1 and 2 exhibited heterogeneous behaviour. In particular, CrNO by PVD sample 2, after 1400 hours, showed a larger increase in weight gain (highlighted in red in Table 12), which, although still at low levels, was significantly higher than that observed for AlCrO by PVD samples after 2000 hours. Conversely, CrNO by PVD sample 1 maintained negative weight gains even after 1400 hours of exposure, suggesting the absence of interactions with the gaseous mixture. Furthermore, for clarity, it is worth emphasizing the superior performance of AlCrO by PVD coating compared to CrNO by PVD. This is highlighted by the

consistent behavior of bothsamples coated with AlCrO by PVD, unlike those coated in CrNO by PVD that showeddifferent behavior. This ambiguous result influenced the decision to avoid sectioning them at the end of the test, in order to prolong their exposure and better investigate their performance over time. Therefore, as indicated in the table, optical and SEM analyses for the CrNO by PVD coating are not reported. Both coatings are potentially valid; the final choice will require more in-depth analyses (as initially planned for the third test campaign).

Regarding the other samples, it is worth noting the acceptable performance of the IN725 alloy. However, also this case, the two IN725 samples exhibited different behaviour. Particularly, for the IN725 highlighted in red in Table 12, the corrosion rate seemed to increase in the 1200-2000 hour period instead of slowing down as expected. For this reason, these samples were subject to further investigation.

On the other hand, the corrosion resistance of the IN625 alloy produced by additive manufacturing with and without welding (IN625 additive and IN625 additive with weld) is scarce, especially in the case of the unwelded sample, which showed excessive weight gains after 2000 hours that did not tend to decrease. The differences in behaviour between these two samples (highlighted in red in Table 12) were investigated further.

The behaviour of the IN718 alloy samples produced by additive manufacturing with and without welding (IN718 additive and IN718 additive with weld) was quite peculiar. After an initial significant weight gain, particularly noticeable after 600 hours, they exhibited a slowdown in subsequent exposures at 1200 and 2000 hours. A similar behaviour was also observed for the forged IN718 alloy samples, although in this case, the initial gains were 4-5 times higher than those of the corresponding additive samples. Previous SEM-EDS analyses showed that corrosion in this alloy tends to initially appear in a localized form, that progressively extended to the whole surface, forming a continuous thick layer with a protective effect that slowed down the corrosion rate.

Lastly, the two surface treatments called Carbonitriding and Full SiO_2 Plasma showed negative performance.

To confirm the general conclusions drawn from the mass measurements, the samples tested at 550°C were observed under a stereoscopic microscope (Figure 63). A qualitative comparison of the images confirmed the presence of thick corrosion deposits in the case of samples that experienced the highest weight gains: IN625, IN718, and SiO2 by PECVD. In the case of the IN725 samples, corrosion appeared milder considering that the lines of the original surface finish are visible. Furthermore, it was confirmed that in the case of sample 725_2, the deposits on the surface were larger respect to the IN 725_1, but, at this stage, it could not be definitively attributed to corrosive phenomena but rather to residues from the decomposition of the gas mixture. Finally, as expected, for the G130, Waspaloy, AlCrO by PVD, and CrNO by PVD samples, the surfaces at the end of 2000 hours appeared largely intact, and at these magnifications, no substantial differences that could justify the differences in weight gain at 1400 hours between CrNO by PVD_1 and CrNO by PVD_2 samples had been identified.

Sample	Stereomicroscope images
625 additive 2000h	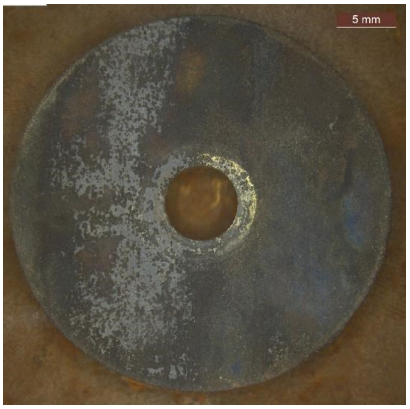 
625 additive with weld 2000h	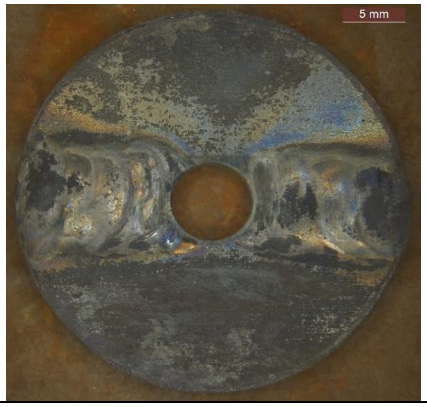 
718 2000h	 
718 1400h	 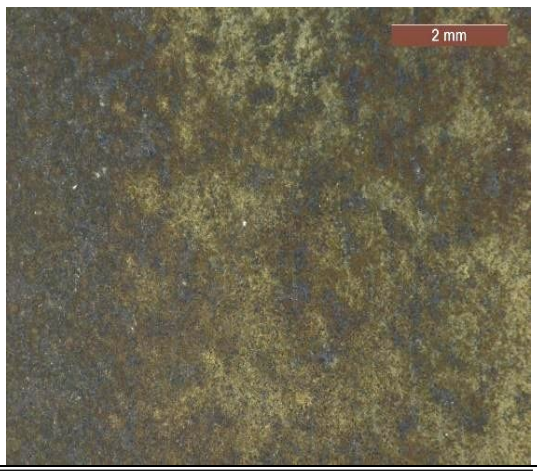

718 additive 2000h	 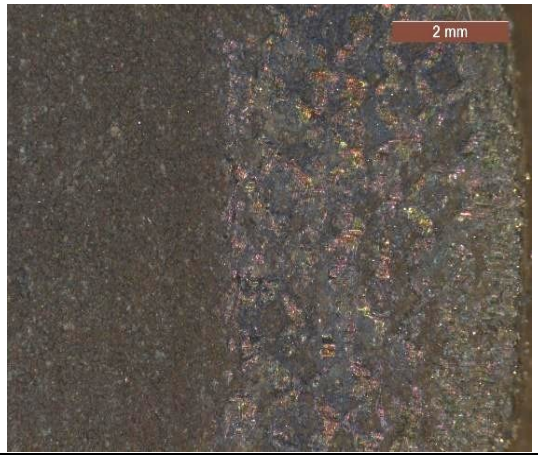
718 additive with weld 2000h	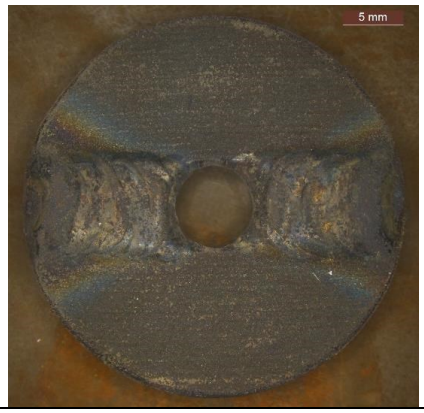 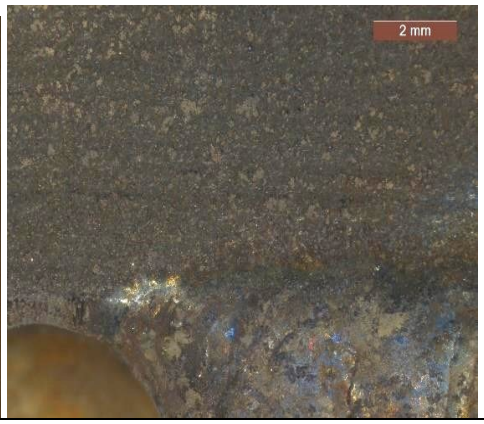
725 1 2000h	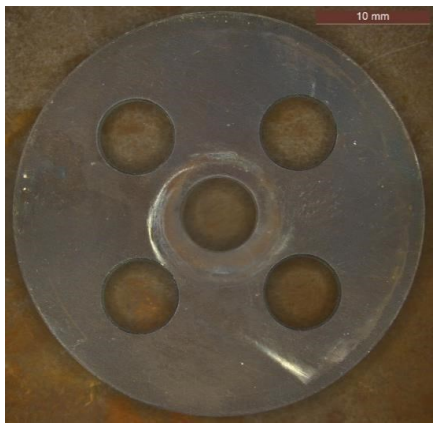 
725 2 2000h	 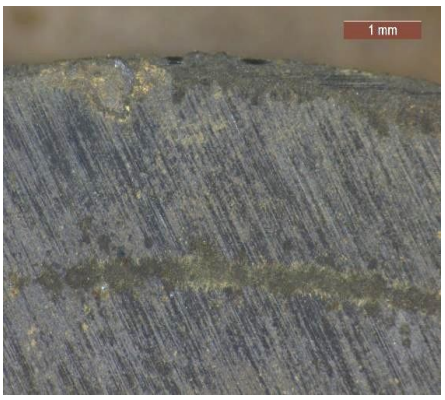

G130 2000h	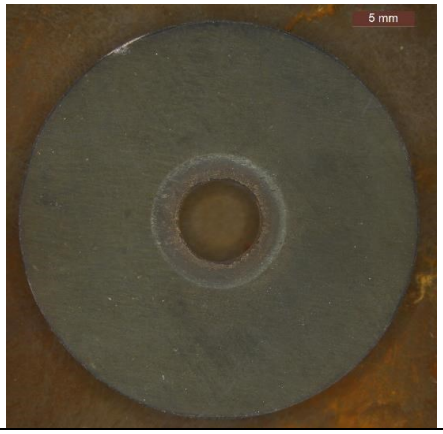
Waspaloy 800h	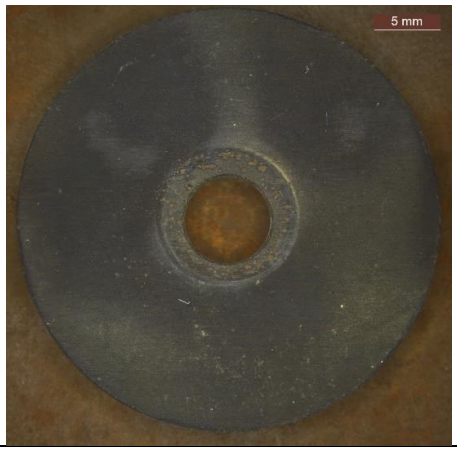 
SiO2 by PECVD 2000h	 
AlCrO by PVD 2000h	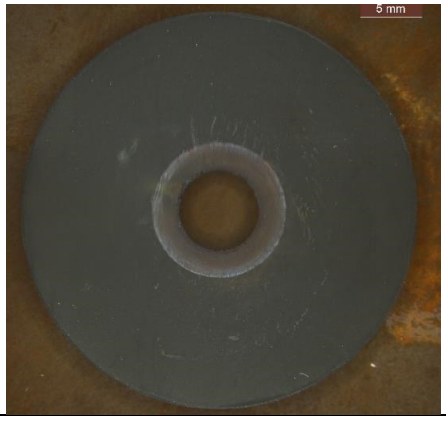 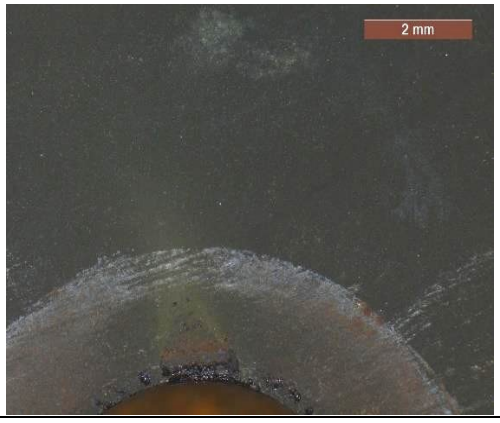

CrNO by PVD 1 1400h	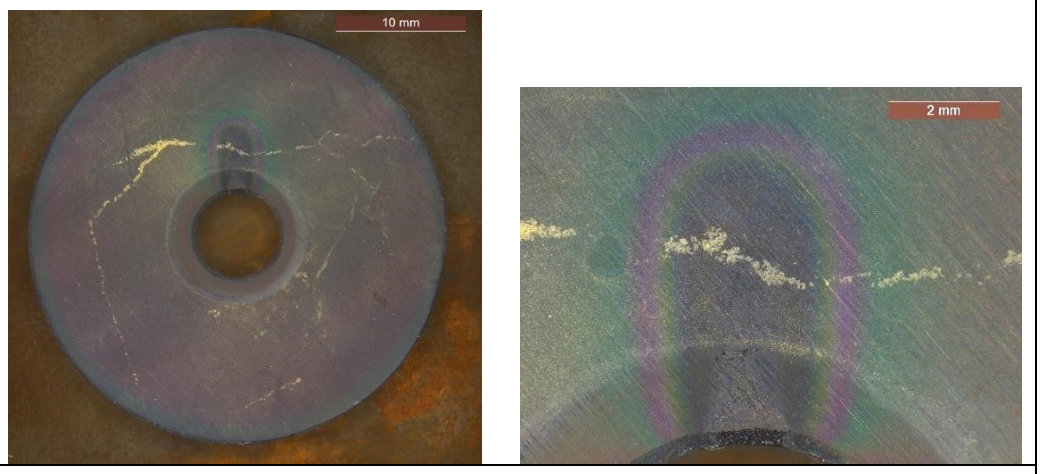
CrNO by PVD2 1400h	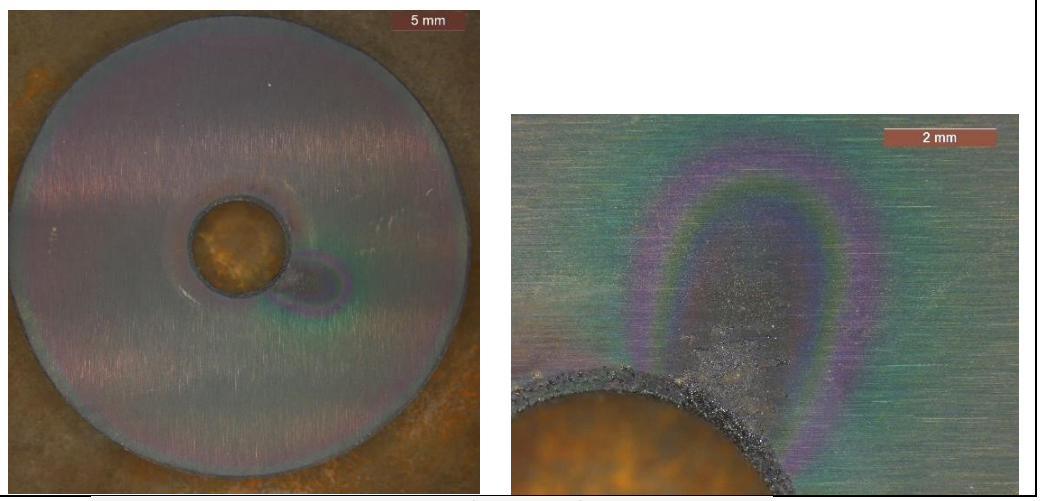

Figure 63 - Images under a stereomicroscope of the samples tested at 550°C

SEM-EDS analyses were conducted on all types of samples to verify the formation of corrosion products and identify their composition. The results of these analyses are presented in Figure 64.

In the case of **IN625** samples, a thick layer of corrosion products containing Ni, S, and O was observed, covering the surface quite uniformly. There were exceptions in some areas of the weld bead of sample **625 additive with weld**, where these deposits were largely absent. This difference could, partially justify the lower weight gain observed on these two samples.

For the **IN718** alloy, the forged sample exhibited localized corrosion phenomena, primarily aligned along the grooves of the initial surface finish. The corrosion products appeared coarse and consist of Ni, Fe, S, and O. The different surface finishing and/or the different microstructure of samples produced by additive manufacturing (**718 additive** and **718 additive with weld**) could explain the better performance respect to the forged ones. In particular, these samples had a surface characterized by round particles, resulting from the powder fusion process. In this case as well, the composition of the corrosion products was primarily composed of Ni, Fe, S and O.

In case of the **IN725** alloy, SEM analysis revealed different corrosion behaviours in the two samples (725_1 and 725_2), which could account for the variations in weight gain. Specifically, the two samples exhibited corrosion products with distinct morphology and composition. In sample 725_1, the corrosion products consisted mainly of Ni, Cr, Fe, S, and O, appearing in a massive form. On the other hand, sample 725_2 displayed needle-shaped corrosion products primarily composed of Ni, S and O.

For the **G130** alloy, the corrosion products formed a very thin interaction layer characterized by Cr, Ni, Co and O, with only low levels of S, which were slightly more abundant in coarser particles on the surface. Similar observations applied to the **Waspaloy** sample, confirming its similarities with the G130 alloy.

The sample coated with **SiO2 by PECVD** exhibited the formation of a continuous layer of iron oxide, consisting of coarse polygonal crystals, proving that this surface treatment was not able to effectively hinder oxidative phenomena induced by the gas mixture.

A different scenario was observed for the **AlCrO by PVD**-coated sample, which displayed a uniform and continuous layer, primarily composed of Al, Cr and O (AlCrO by PVD). Only in isolated areas, minor defects were noticeable in the coating, likely leading to the exposure of the substrate and the formation of corrosion deposits containing Fe, Cr, Al, O and traces of S.

The **CrNO by PVD** coating also demonstrated high performance, revealing the presence of a continuous and impermeable layer primarily composed of Cr and O on the surface. Despite variations in weight gain observed at 1400 hours, SEM-EDS analyses conducted on CrNO by PVD_1 and CrNO by PVD_2 samples did not confirm these differences. The need for further investigations will be considered.

<table>
<tr><th>Sample</th><th>SEM surface analysis</th></tr>
<tr><td>625 additive 2000h</td><td>
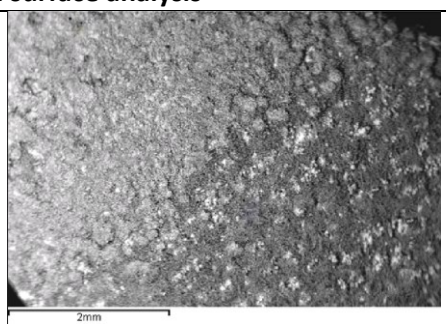

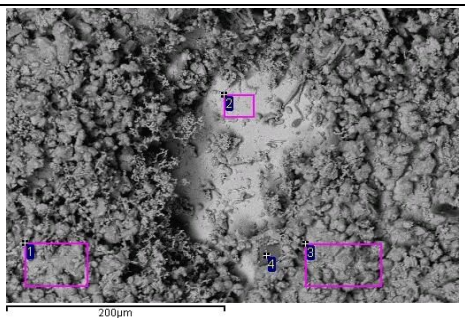

<table>
<tr><th></th><th>O</th><th>Al</th><th>Si</th><th>S</th><th>K</th><th>Ti</th><th>Cr</th><th>Fe</th><th>Ni</th><th>Mo</th></tr>
<tr><td>1</td><td>31.59</td><td></td><td></td><td>15.85</td><td></td><td></td><td>1.12</td><td>0.28</td><td>49.31</td><td>1.85</td></tr>
<tr><td>2</td><td>13.12</td><td>2.17</td><td></td><td>1.61</td><td></td><td>0.60</td><td>18.44</td><td>0.50</td><td>56.21</td><td>7.35</td></tr>
<tr><td>3</td><td>27.23</td><td></td><td></td><td>15.47</td><td></td><td></td><td>1.45</td><td>0.60</td><td>53.12</td><td>2.13</td></tr>
<tr><td>4</td><td>47.62</td><td>13.79</td><td>18.42</td><td>1.83</td><td>9.00</td><td>0.85</td><td></td><td>0.78</td><td>7.70</td><td></td></tr>
</table>
</td></tr>
<tr><td>625 additive with welding 2000h</td><td>
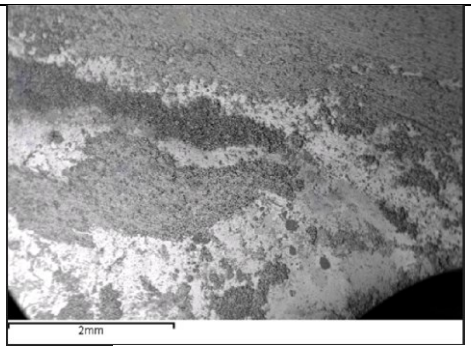

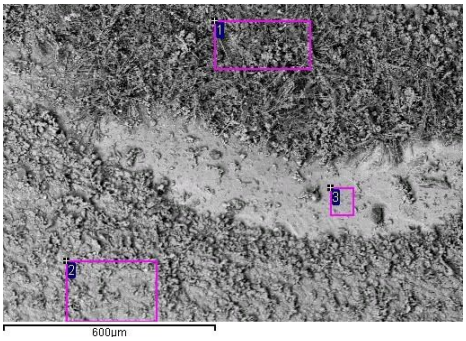

<table>
<tr><th></th><th>O</th><th>Mg</th><th>Al</th><th>S</th><th>Ti</th><th>Cr</th><th>Fe</th><th>Ni</th><th>Nb</th><th>Mo</th></tr>
<tr><td>1</td><td>28.11</td><td></td><td></td><td>15.14</td><td></td><td>1.02</td><td></td><td>55.73</td><td></td><td></td></tr>
<tr><td>2</td><td>41.15</td><td></td><td></td><td>17.74</td><td></td><td>0.81</td><td>0.38</td><td>39.11</td><td></td><td>0.82</td></tr>
<tr><td>3</td><td>33.38</td><td>2.07</td><td>4.39</td><td>1.35</td><td>0.41</td><td>11.28</td><td>0.40</td><td>32.30</td><td>6.32</td><td>8.10</td></tr>
</table>
</td></tr>
</table>

718 2000h

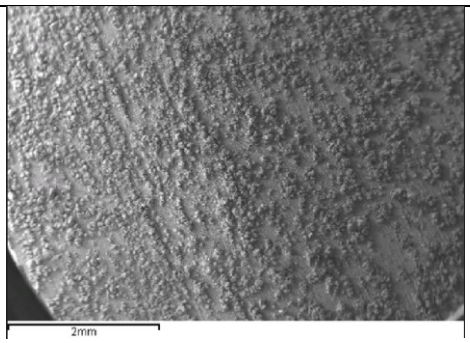

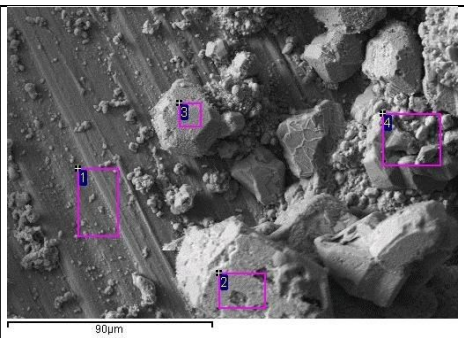

	O	Al	Si	S	Ca	Ti	Cr	Fe	Ni	Nb	Mo
1	34.81	1.01	0.06	0.50	0.16	1.13	21.81	10.04	23.84	4.01	2.63
2	17.17			24.05				2.22	53.02		3.55
3	17.57			27.36				1.41	50.51		3.16
4	25.52			16.61				14.52	43.35		

718 additive 2000h

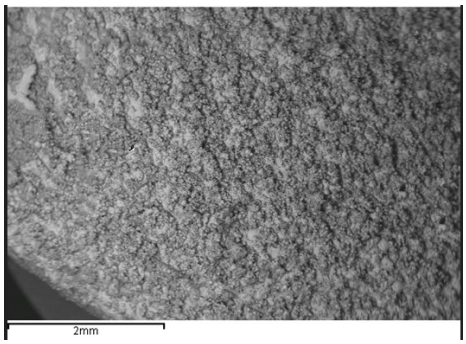

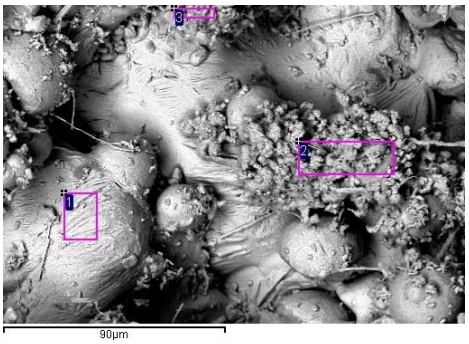

	O	Al	S	Ti	Cr	Fe	Ni	Nb	Mo
1	13.55	1.77	2.37	1.51	15.88	17.48	46.43		1.02
2	29.03		10.66	0.26	3.69	18.54	37.80		
3	29.53	0.44	9.61	0.15	2.47	9.77	45.48	1.26	1.29

718 additive with weld 2000h

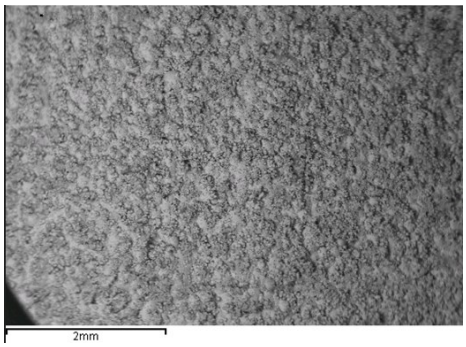

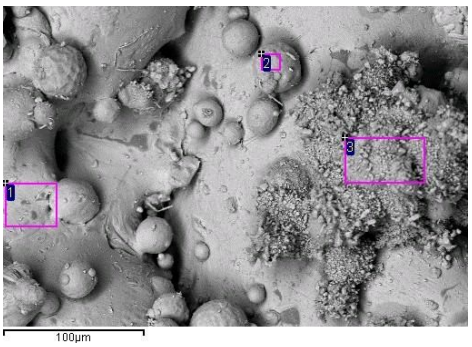

	O	Mg	Al	S	Ti	Cr	Fe	Ni	Nb	Mo
1	27.33		6.25		1.95	14.17	10.87	30.26	5.19	3.97
2	39.14	1.80	4.90	1.03	3.10	11.06	7.19	20.31	8.20	3.26
3	34.37		1.04	8.67	0.58	3.55	16.51	33.07	0.67	1.54

725 1 2000h

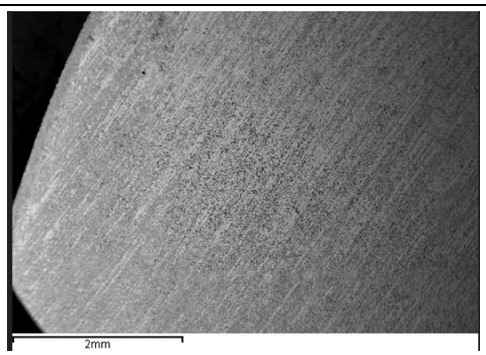

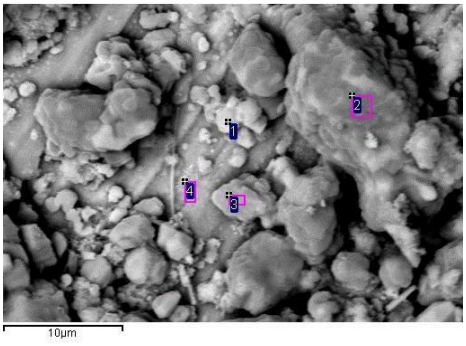

	O	S	Ti	Cr	Fe	Ni	Mo
1	16.65	28.85		5.01	2.34	45.34	1.81
2	24.63	22.51		0.79	1.44	47.90	2.72
3	41.70	17.21		1.73	9.49	27.13	2.75
4	18.97	2.85	1.48	26.81	10.20	33.84	5.86

725 2 2000h

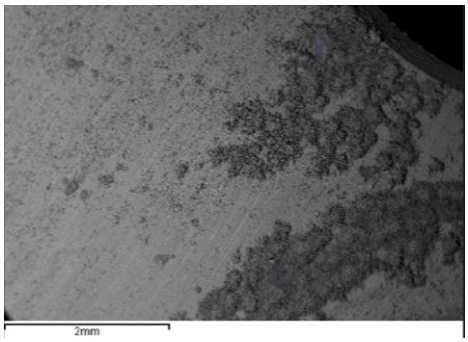

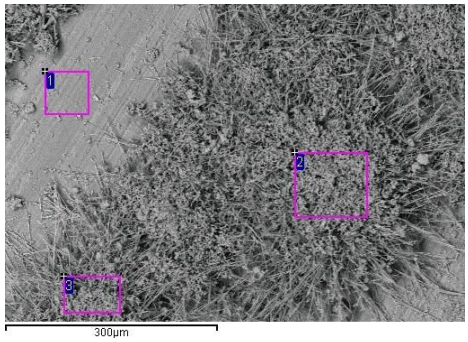

	O	Si	S	Ti	Cr	Fe	Ni	Nb	Mo
1	39.90	0.18		1.31	35.44	2.07	14.74	0.77	5.59
2	18.66		7.18			0.36	73.09		0.71
3	22.22		8.08		0.54	0.40	65.97		2.78

G130
2000h

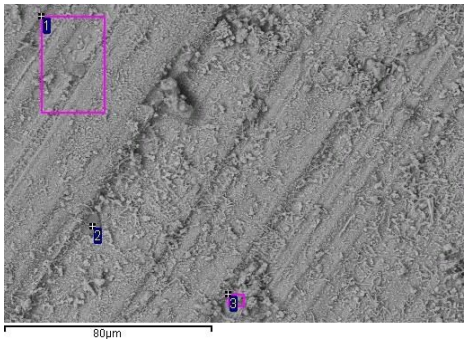

	O	Al	Si	S	Ti	Cr	Fe	Co	Ni
1	34.12	1.46	0.35	2.74	2.43	32.21	0.80	8.31	17.58
2	62.58		33.80			2.69			0.93
3	29.68	0.77		8.59	1.35	29.15	0.28	8.25	21.93

Waspaloy 800h

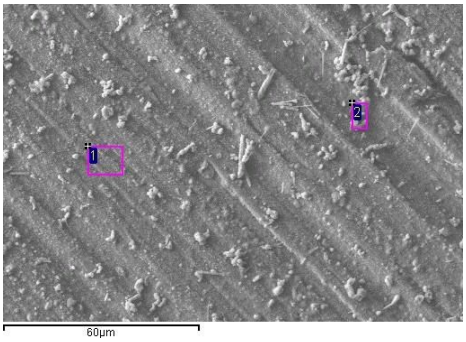

	O	Al	Si	S	Ca	Ti	Cr	Fe	Co	Ni	Mo
1	39.29	1.41	0.69	1.23	0.22	3.66	25.12	0.51	4.74	20.37	2.76
2	35.14	0.71	0.17	0.68	0.33	2.36	18.19	0.64	3.12	36.75	1.91

SiO2 by PECVD 2000h

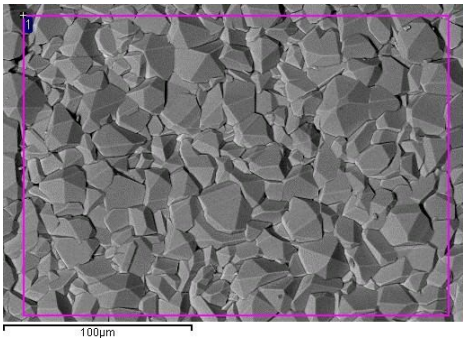

	O	Fe
1	39.26	60.74

AlCrO by PVD 2000h

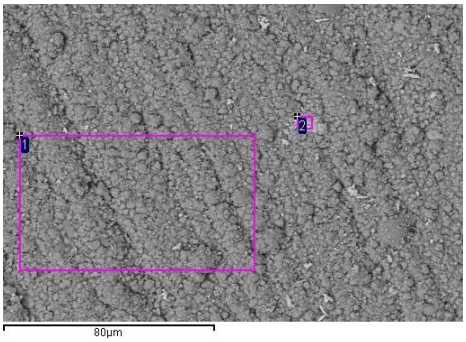

	O	Al	Si	S	Cr	Fe	Ni
1	52.28	28.56	0.72		17.74		0.69
2	41.80	4.06		0.87	14.56	38.71	

CrNO by PVD 1 1400h

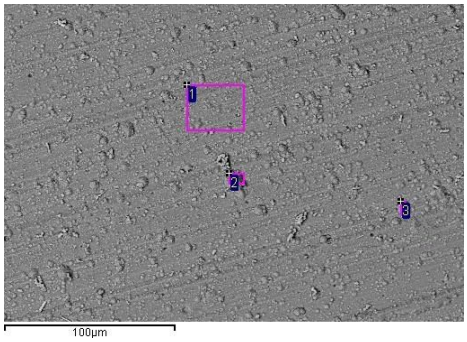

	O	Al	Si	S	Ca	Cr	Fe	Ni
1	35.63	0.28	0.23			62.06		1.80
2	37.47		0.27		0.33	53.85	0.62	7.46
3	39.45		0.77	0.27		56.41		3.10

CrNO by PVD 2 1400h

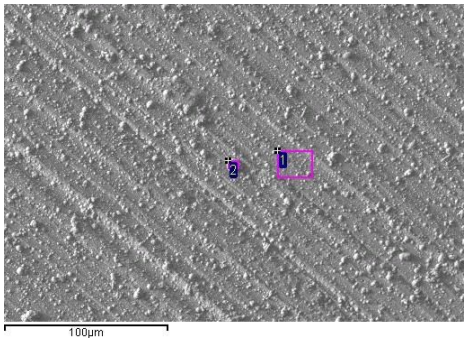

	O	S	Cr	Fe	Ni
1	36.42		63.58		
2	40.36	0.43	56.71	0.38	2.12

Figure 64 - Test at 550°C – SEM surface analysis (wt.%)

As previously mentioned, additional cross-section analyses were conducted using both optical and electron microscopy to investigate into the reasons for the differences in weight gain observed in **IN625 additive** and **IN725** samples.

Regarding the **IN625** alloy samples, the analysis results were presented in (Figure 65Figure 66). In both samples, the base metal was covered by a relatively dense, adherent and discontinuous interaction layer, often overlaid by a second layer with a powdery appearance (Figure 65), indicating incomplete protection. It was confirmed that in sample **625 additive with weld**, the welding zone, starting from the HAZ up to the melted zone, was nearly free of this interaction layer, partly explaining the lower weight gain compared to the unwelded sample. SEM-EDS analyses also suggested differences in the composition of the two materials. Particularly, sample **625 additive with weld** had a higher concentration of Ni and Mo, with lower Fe content compared to sample **625 additive** (Figure 65Figure 66). These chemical composition variations had led to significant differences in the element content within the interaction layer, which was richer in Mo and Cr in the welded sample. These differences might account for the improved corrosion resistance of the welded sample **625 additive with weld** compared to the unwelded one.

Regarding the **IN725** alloy samples, the analysis results were presented in Figure 67Figure 68. Unfortunately, the microscopic analysis of sample IN**725_2** did not reveal the expected presence of the interaction layer,

which might had been removed during the metallographic section preparation (Figure 67). This made challenging the comparisons with the sample **725_1**, where the interaction layer was present, albeit detached from the substrate due to resin shrinkage. The analysis of these deposits showed, as in the case of **IN625**, the presence of a compact and initially adherent interaction layer on the substrate, primarily composed of Cr, Mo, Ni, Nb and O, covered by a powdery layer based on Ni and S. In the case of sample **725_2**, the compact layer lacks Nb and had a lower Mo content. It remained to be clarified whether this difference was real or possibly due to an error in the EDS microprobe's element identification, influenced by the proximity of Nb, Mo and S spectral lines and the limited thickness of the remaining interaction layer on this sample.

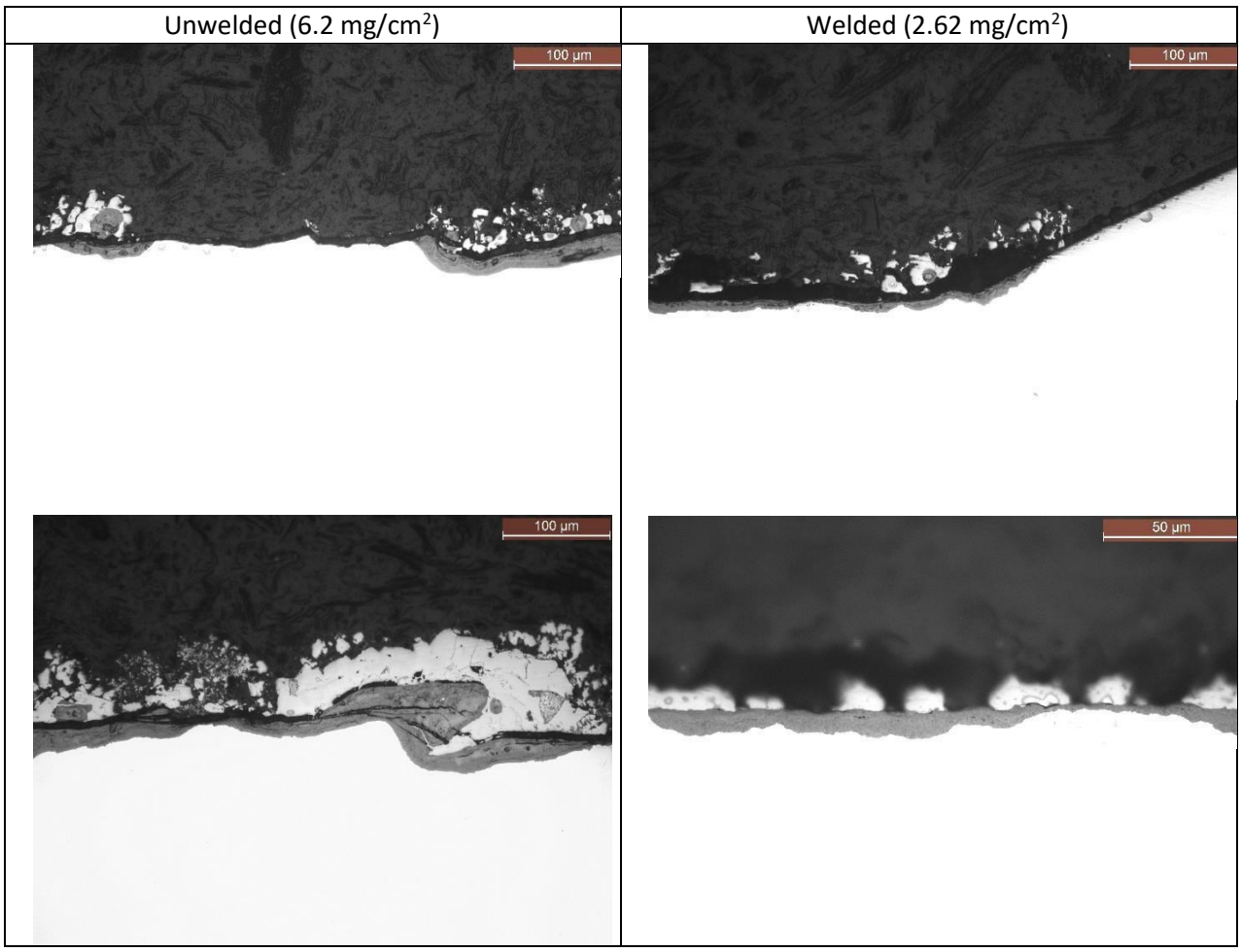

Figure 65 - Optical microscope images of sections of IN625 alloy samples

Unwelded (6.2 mg/cm^2)	Welded (2.62 mg/cm^2)

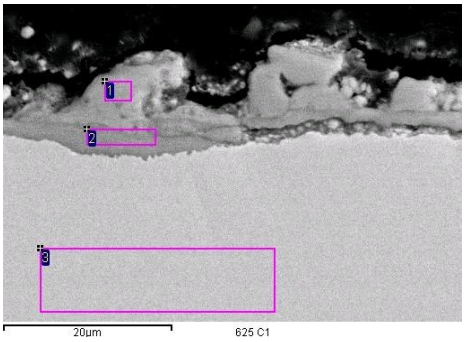

	O	S	Ti	Cr	Fe	Ni	Nb	Mo
1		41.81		1.26	0.99	55.94		
2	29.86	9.44	1.93	24.67	2.55	16.10	7.04	8.41
3			1.49	22.69	7.72	51.65	5.78	10.67

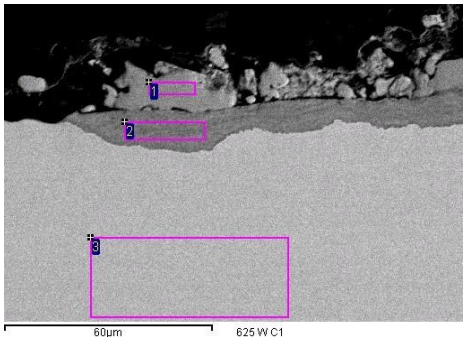

	O	S	Ti	Cr	Fe	Ni	Nb	Mo
1		40.12				59.88		
2	28.64	5.99		35.27	1.31	3.34	7.49	17.97
3			0.51	20.12	0.11	61.09	4.81	13.36

Figure 66 – SEM-EDS cross-section of IN625 alloy samples (wt.%)

725_1 (0.72 mg/cm^2)	725_2 (1.06 mg/cm^2)

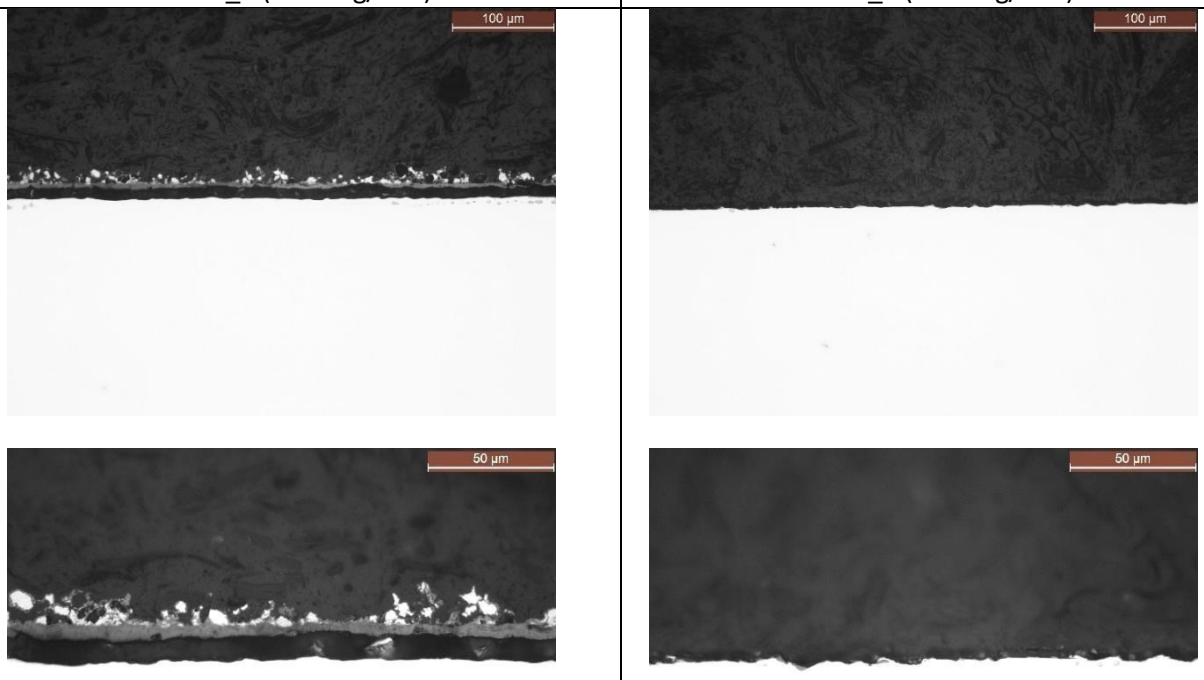

Figure 67 - Optical microscope images of sections of IN725 alloy samples

725_1 (0.72 mg/cm^2)

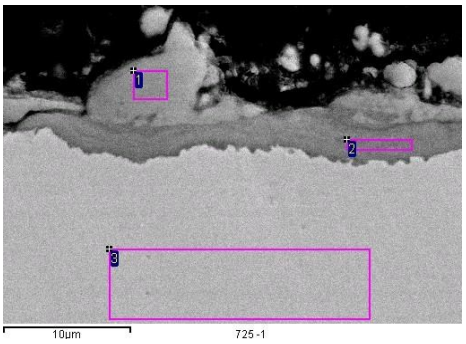

	O	S	Ti	Cr	Fe	Ni	Nb	Mo
1		43.63		0.65		55.71		
2	36.38	2.61	2.23	29.12	1.45	7.36	6.92	13.93
3			1.95	22.99	8.33	52.19	2.87	11.68

725_2 (1.06 mg/cm^2)

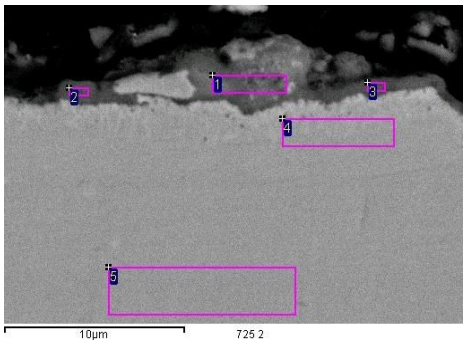

	O	S	Ca	Ti	Cr	Fe	Ni	Nb	Mo
1	34.74	5.04	0.57	0.67	41.12	2.89	9.75		5.22
2	34.97	4.91	1.65	0.58	52.89	0.70	4.29		
3	39.56		0.48	1.55	45.16	1.46	8.06		3.73
4				1.51	15.59	7.97	58.48	4.30	12.16
5				1.51	22.96	7.34	56.07		12.11

Figure 68 - SEM-EDS cross-section of IN725 alloy samples (wt.%)

To complete this characterization, the remaining samples were analysed by optical microscope and SEM.

The results of the **IN718 additive with weld and IN718 additive** cross- section analyses were shown in Figure 69Figure 70. In both samples, the surface, due to the manufacturing process, appeared to be very rough. In this case, the interaction was not uniformly distributed, but it was localized only on few areas, especially on the not fully melted particles at the surface, which had a different microstructure respect to the rest. In the IN718 additive with weld, only one short crack was found on the base metal (Figure 69). In the HAZ there was no presence of intergranular cracks. SEM analysis confirmed the presence of localized corrosion. There were two layers in the areas where the interaction occurs. For both materials EDS analysis suggested that the inner layer contained C, O, S, and Cr and a small amount of Fe, Mo, Nb; while the outer layer contained mainly S, O, Cr and Ni. In addition, inside the crack found in the base metal of the welded sample, there was no interaction products, suggesting that it might be pre-existing.

The **IN718** also showed localized corrosion, which was more diffused than in the samples made by additive. In this case, the interaction was in the form of pits on which an outer layer was formed (Figure 71). The elements of these two layers were the same as identified in the layers of the samples made by additive manufacturing (Figure 71-b). As already documented, this corrosion process will cause these pits to progressively merge into a single and uniform more protective layer.

IN718 as-built _ additive (1.24 mg/cm^2)	In718 welded _ additive (1.71 mg/cm^2)
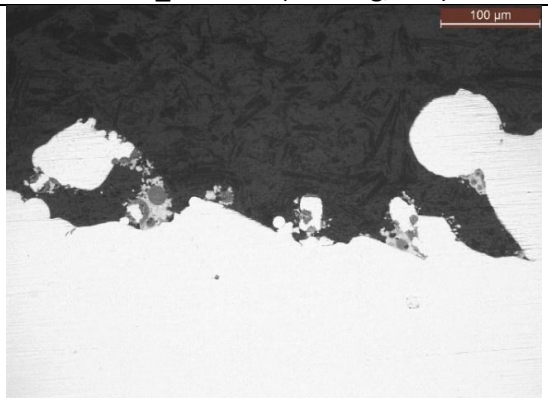	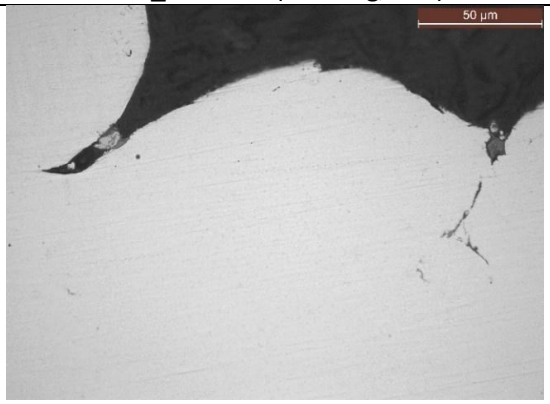 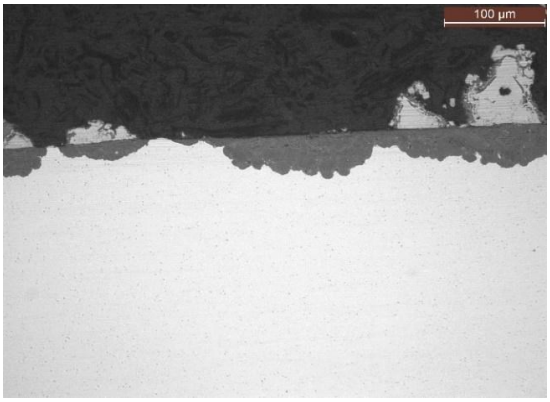

Figure 69 - Optical microscope images of IN718 welded_additive and as-built_additive (cross-sections)

IN718 additive (1.24 mg/cm^2)	IN718 additive with weld (1.71 mg/cm^2)
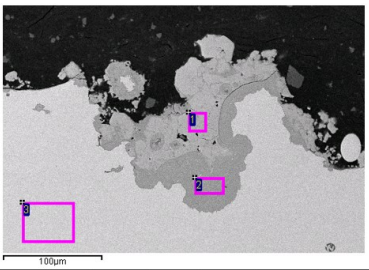	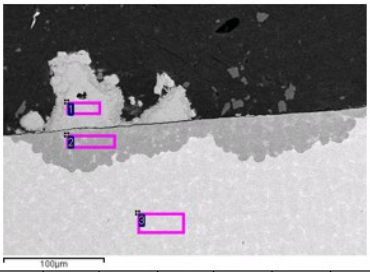 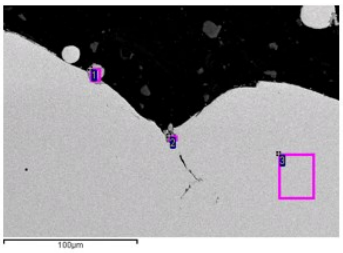

	C	O	Al	S	Ti	Cr	Fe	Ni	Nb	Mo
1	11.48	3.03		32.42			1.95	51.07		
2	7.91	31.47	0.74	5.45	1.57	27.46	8.75	3.21	8.62	4.81
3			0.75		1.07	19.40	16.43	51.72	6.34	4.3

	C	O	Al	Si	S	Ti	Cr	Fe	Ni	Nb	Mo
1	14.70	2.47			31.68		0.46	1.79	48.89		
2	6.29	33.54	0.68	0.13	7.24	1.27	22.71	6.79	7.37	7.12	6.87
3			0.60			1.07	18.30	19.50	49.01	7.30	4.22

	C	O	Al	S	Ca	Ti	Cr	Fe	Ni	Nb	Mo
1	7.5	15.68		22.63		0.64	9.66	3.36	33.32	2.97	4.23
2	14.8	25.92	1.02	7.58	0.29	1.35	23.13	5.54	7.8	7.1	5.46
3			0.39			1.08	19.59	17.13	51.38	6.34	4.09

Figure 70 - SEM-EDS analysis of IN718 welded_additive and as-built_additive (cross-section) (wt.%)

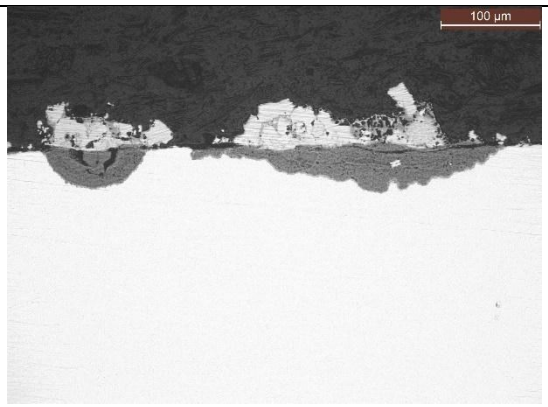

(a)

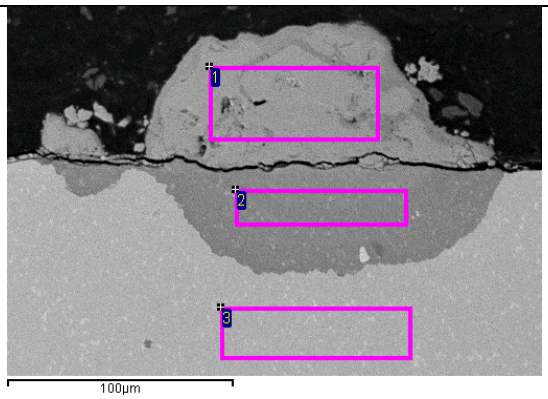

	C	O	Al	S	Ti	Cr	Fe	Ni	Nb	Mo
1	13.38	10.76		26.09		0.93	5.98	42.85		
2	7.43	31.18	0.79	7.05	1.19	22.78	7.37	9.22	8.15	4.84
3			0.90		1.26	19.28	17.92	50.57	5.88	4.18

(b)

Figure 71 - Optical microscope images (a) and SEM-EDS images (b) of IN718 (cross-section) (wt.%)

As evident from Table 26, one of the IN718 samples was extracted after only 600 h of exposure due to the notable difference in mass gain observed for the same material under similar conditions in the first test campaign. In particular, IN718 sample in second test campaign had a larger mass gain (4-5 times higher) compared to the first test campaign. The results of this sample for the second test campaign were illustrated in Figure 72. In the first test campaign, corrosion manifested in the form of pits, with a maximum thickness of approximately 25µm. In contrast, during the second test campaign, the corrosion appeared uniform and covered the entire surface, with a consistent thickness of 18 µm. Limited areas in the second campaign exhibited increased corrosion depth, reaching approximately 70 µm. There isn't a precise reason behind this divergent behaviour of the IN718 alloy in the two test campaigns. It appeared that in the case of the second test campaign, corrosion occurred after a shorter incubation time. Indeed, the interaction in the second test campaign was evidently at a more advanced stage. From these analyses, it was possible to suppose the potential corrosion mechanism of the IN718 alloy exposed to 80% CO_2 + 20% SO_2 at 550°C: it initiates in the form of pits, which, over time, merge to form a uniform corrosion layer. Optical microscope and SEM analyses had also confirmed the mass gain assessments.

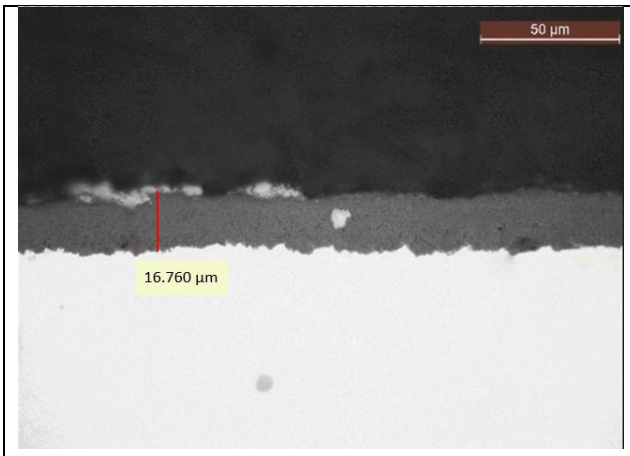

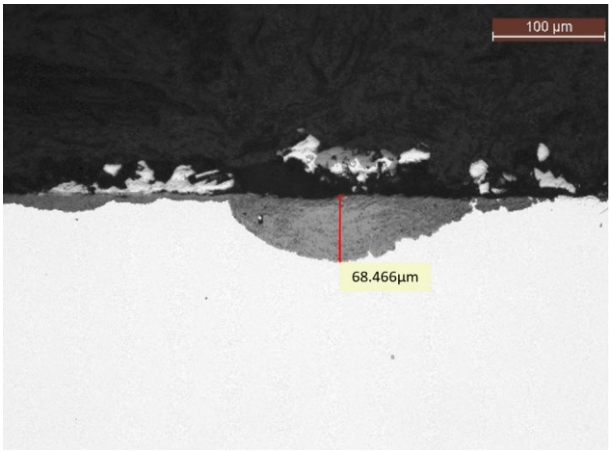

	O	Al	S	Ti	Cr	Fe	Ni	Mo
1	7.33		22.73		0.74	9.39	54.88	4.93
2	27.60	0.69	3.92	0.97	20.12	14.25	30.81	1.64
3	21.90	0.41	15.85		4.15	16.83	37.96	2.90

Figure 72 – Optical (a) and SEM (b) cross-section analysis of IN718 exposed at 80%CO_2+20%SO_2 for 600h (wt.%

The results of the cross-section of the **SiO2 by PECVD** sample had been reported below (Figure 73). Corrosion was uniform and intense, suggesting the low protectiveness of this layer. SEM analysis revealed three layers: the central one was the coating composed of O, Si and traces of S and Fe. Externally, a thick layer of iron oxide was formed, as the Fe diffused easily through the coating, while the innermost layer contained O, S, Cr, and Fe, and probably iron and chromium sulphides were formed.

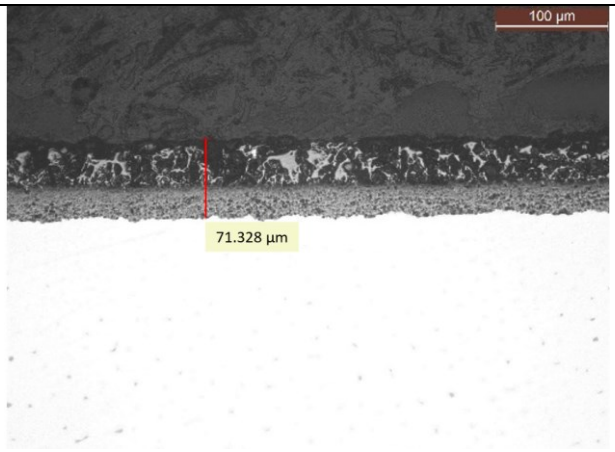

(a)

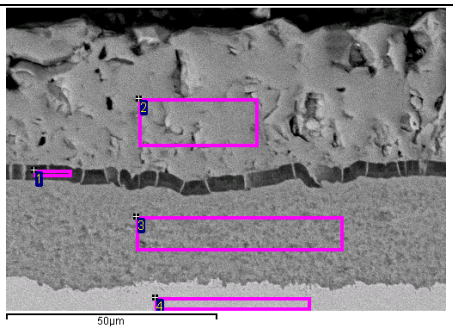

	O	Si	S	V	Cr	Fe	Ni	Mo
1	52.90	30.99	3.94		0.85	11.32		
2	36.51				0.57	62.92		
3	29.10	0.49	12.58	0.53	22.09	35.21		
4		0.14		0.66	12.17	84.60	0.79	1.64

(b)

Figure 73 – Optical (a) and SEM (b) cross-section analysis of the SiO2 by PECVD sample (wt.%)

By analysing the cross-section of **G130,** as shown in Figure 74, uniform interaction was observed over the entire sample surface, with the formation of a very thin protective oxide layer containing Cr, Ni, and Co. The content of sulphur was negligible, suggesting the good resistance of the alloy to the interaction with this element. Finally, several shrinkage porosities were detected in the section, some of them inter-connected with the surface. These pores of different sizes and shapes were already present in the alloy, being a consequence of the manufacturing process and seem to be evenly distributed throughout the alloy (Figure 75).

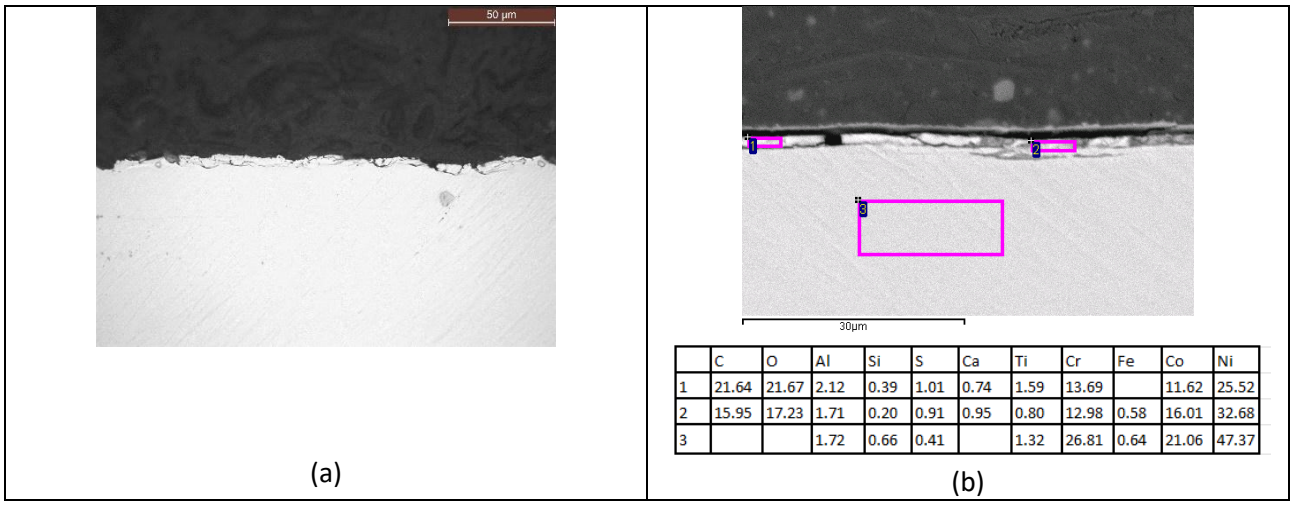

	C	O	Al	Si	S	Ca	Ti	Cr	Fe	Co	Ni
1	21.64	21.67	2.12	0.39	1.01	0.74	1.59	13.69		11.62	25.52
2	15.95	17.23	1.71	0.20	0.91	0.95	0.80	12.98	0.58	16.01	32.68
3			1.72	0.66	0.41		1.32	26.81	0.64	21.06	47.37

Figure 74 - Optical (a) and SEM (b) cross-section analysis of the G130 sample (wt.%)

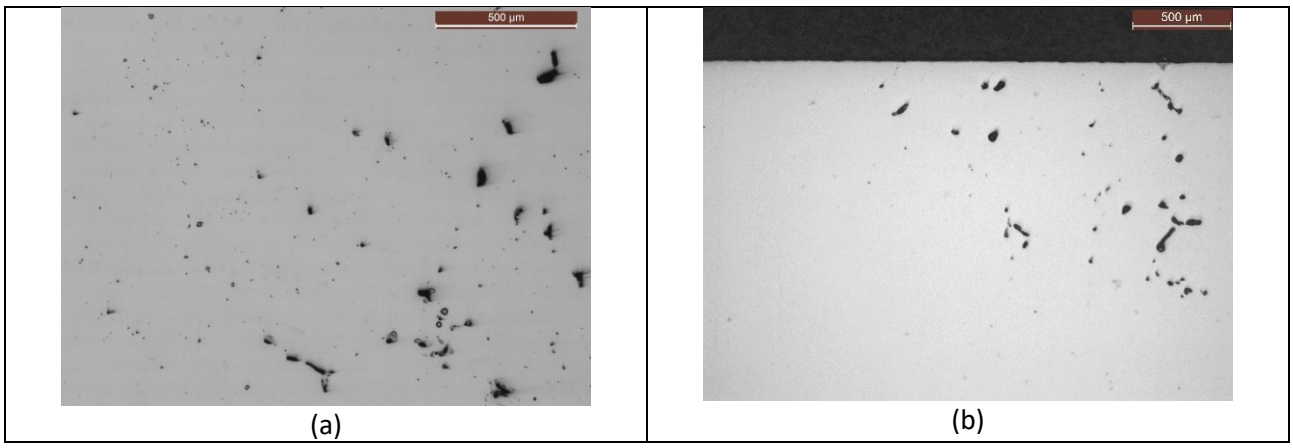

Figure 75- Shrinkage porosity identified on G130 at 2000 hours (a) and at 1200 hours (b).

In case of **Waspaloy**, SEM analysis confirmed but the presence of a limited interaction. As in the case of G130, the thin oxide layer formed at the surface contains Cr, Ti and Co and only small amounts of sulphur. Waspaloy also exhibited signs of porosity randomly distributed in the material (Figure 76Figure 77).

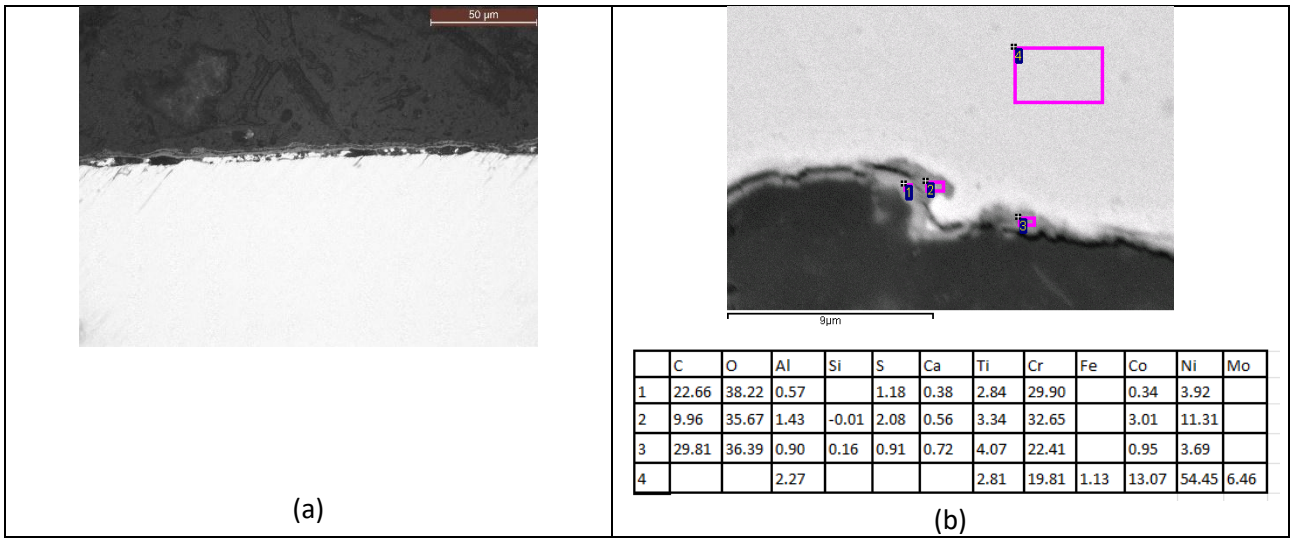

	C	O	Al	Si	S	Ca	Ti	Cr	Fe	Co	Ni	Mo
1	22.66	38.22	0.57		1.18	0.38	2.84	29.90		0.34	3.92	
2	9.96	35.67	1.43	-0.01	2.08	0.56	3.34	32.65		3.01	11.31	
3	29.81	36.39	0.90	0.16	0.91	0.72	4.07	22.41		0.95	3.69	
4			2.27				2.81	19.81	1.13	13.07	54.45	6.46

Figure 76 - Optical (a) and SEM (b) cross-section analysis of the Waspaloy sample (wt.%)

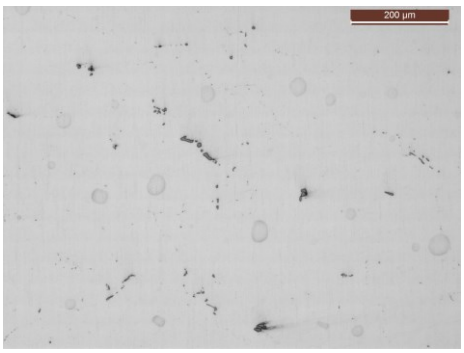

Figure 77 – Porosity identified on Waspaloy at 800h

In Figure 78 the analysis of the **AlCrO by PVD** sample cross-section showed a continuous, adherent coating of constant thickness. Since no interaction was visible, the coating appeared to be protective. However, SEM highlighted three layers: the outer one rich in O, Al, and Cr, the central one rich in Cr and with a little content of O, and the inner one rich in O, Cr and Fe. In some areas, internal sections of the material also exhibited rich concentrations of O, S, and Cr. Nevertheless, the coating appeared to be still protective.

In fact, generally, to address the issue of oxidizing-sulfurizing atmospheres, the most promising approach appears to involve pre-oxidizing an alloy to promote the formation of a flawless chromia or alumina layer, free of defects and well-adhered to the substrate [165]. In the absence of Al and with exclusive chromia presence, pre-oxidation retains its effectiveness against subsequent sulfurization. In such scenarios, pre-oxidation proves more effective against subsequent sulfurization when conditions prevent spinel formation, ensuring exclusive chromia formation. In fact, in the chromia/alloy interface, Cr serves as a sulphur getter, thereby minimizing the penetration of sulphur through an intact chromia layer [165]. It is noteworthy that the protective AlCrO by PVD coating contains oxygen, aluminum, and chromium. However, it has been observed that materials subsequently exposed to sulfurizing or sulfurizing-oxidizing atmospheres inevitably undergo catastrophic degradation due to sulphide corrosion. Consequently, after a certain incubation period, which extends proportionally with the quality and adhesion of the oxide layer, sulphur atoms or molecules diffuse inward, reaching the oxide-alloy interface where sulphides rapidly develop on the alloy surface. This results in the progressive breakdown of the protective oxide layer and the swift deterioration of the material due to sulphide corrosion [165]. In accordance with [166] sulphur penetration through oxide scales can occur through two mechanisms:

- Dissolution of sulphur within the oxide and subsequent diffusion through the bulk or along grain boundaries to reach the scale/metal interface.
- Transportation of sulphur-containing species through physical defects in the scale, such as pores or cracks.

However, specifically for chromia scales, the second penetration process becomes relevant. In fact, radiotracer techniques with ^{35}S demonstrated that sulphur solubility in chromia, both within the bulk and at grain boundaries, is negligible [167-168]. The observation of internal $Cr_{1-x}S$ precipitates at the scale-alloy interface, beneath the chromia layer, at least for ferritic alloys, had been frequently reported in literature. In this specific case, these precipitates are formed following the reaction:

$$\frac{7}{2}\,Cr\,(s)+\frac{3}{2}\,SO_2(g)\rightarrow\frac{3}{2}\,CrS(s)+Cr_2O_3(s)\quad con\ \Delta G^0=-735.9kJ\quad(spontaneous\ reaction)$$

Then, these sulphides were oxidated through the reaction:

$$2CrS(s)+\frac{3}{2}\,SO_2(g)\rightarrow\frac{7}{4}\,S_2(s)+Cr_2O_3(s)\quad con\ \Delta G^0=-173.4kJ\quad(spontaneous\ reaction)$$

The released sulphur tends to migrate inward, leading to the formation of internal $Cr_{1-x}S$ precipitates instead of escaping outward. This phenomenon, as noted by Choi and Stringer [169-170], explains the observed trend where the quantity and depth of internal $Cr_{1-x}S$ precipitates increased with reaction time in dry SO_2 gas.

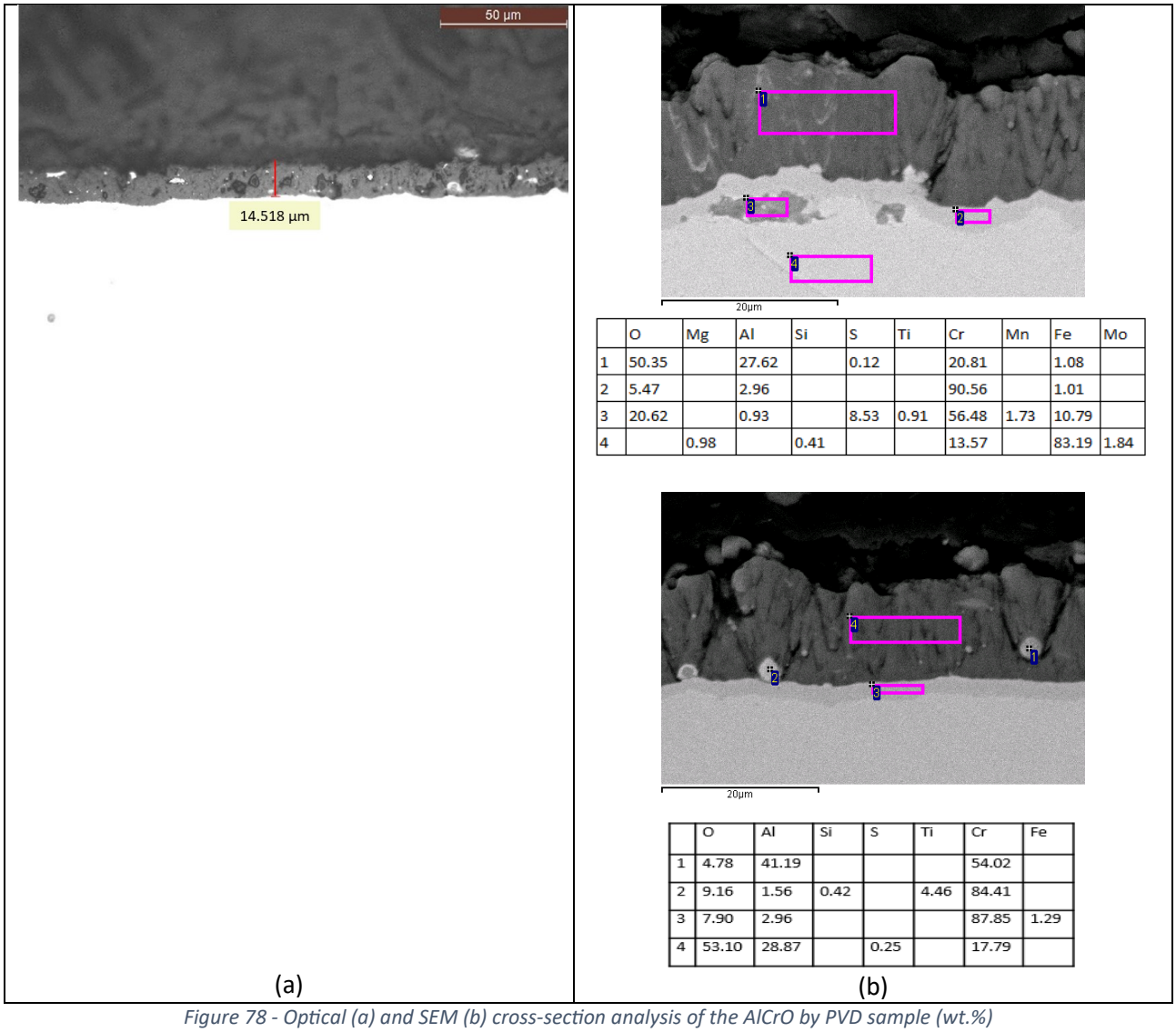

	O	Mg	Al	Si	S	Ti	Cr	Mn	Fe	Mo
1	50.35		27.62		0.12		20.81		1.08	
2	5.47		2.96				90.56		1.01	
3	20.62		0.93		8.53	0.91	56.48	1.73	10.79	
4		0.98		0.41			13.57		83.19	1.84

	O	Al	Si	S	Ti	Cr	Fe
1	4.78	41.19				54.02	
2	9.16	1.56	0.42		4.46	84.41	
3	7.90	2.96				87.85	1.29
4	53.10	28.87		0.25		17.79	

Figure 78 - Optical (a) and SEM (b) cross-section analysis of the AlCrO by PVD sample (wt.%)

In **conclusion**, the study showed that at 550°C the mixture 80%CO_2+20%SO_2 interacted to a greater or lesser extent with all the tested samples. The best performance among the metallic alloys was exhibited by G130 and Waspaloy, while among the coatings, AlCrO by PVD and CrNO by PVD behaved very well. All the metallic alloys were characterized by a higher content of Co associated with a high Ni content. Conversely, the worst performance was exhibited by the SiO2 by PECVD coating, which formed a thick interaction layer, demonstrating to be un-protective.

The mass gain of **Waspaloy** samples obtained after 800 hours of exposure remained consistent. Similarly, **G130** showed a comparable trend for both samples, exhibiting a slowdown in the corrosive phenomenon, contained throughout the exposure period. G130 and Waspaloy, both Ni-Cr-Co alloys, were not directly comparable due to different exposure times: 2000h for G130 and 800h for Waspaloy. However, some similarities were observed in both cases, showing good resistance to 80% CO_2 + 20% SO_2 atmospheres, where the interaction was mainly due to oxygen, with traces of sulphur. Moreover, the elements reported in the interaction layer were consistent: C, Co, Cr, Ni and both materials contained porosities. Their good performance was probably due to the presence of cobalt, known to enhance resistance to sulphur attack in nickel-based alloys with Cr values <30-35%.

Among the promising coatings, **CrNO by PVD** and **AlCrO by PVD** stood out**.** Considering the mass gain of the two samples, CrNO by PVD showed a divergence: one exhibited an increase in mass gain, while the other maintained negative values even after 1400 hours, indicating negligible interaction. In contrast, AlCrO by PVD displayed a coherent behaviour among the samples and a minimal mass gain growth over time. The positive performance of these coatings aligns with the previously mentioned effective procedure for countering sulfurization, involving peroxidation and formation of a well-adherent chromia or alumina scale, that are present in these coating. However, it is essential to note that, as some articles suggest, over time at elevated temperatures, sulphur ions could penetrate the alumina or chromia layer, reaching the alloy surface and reacting with Fe and Cr to form their respective sulphides.

Acceptable behaviour was exhibited by **IN718 additive**, with consistent and not excessively high mass gain values. Both samples appeared to have a very rough surface and the interaction layer was localized on few areas, mainly on the partially melted particles. On the contrary, **IN718** (forged) showed elevated mass gain values, with aligned behaviour and corrosion slowing down over time. IN718 sample also exhibited localized corrosion, although it was more intense compared to the samples made by additive manufacturing. This difference could be related to the different roughness of the samples (i.e., smooth for the forged and rough for the additive) and/or to the different microstructures.

Uncertain behaviour was exhibited by **IN725**, showing different corrosion trends in the two analysed samples. One sample exhibited an increased corrosion rate, while the other showed deceleration. Differences in the interaction layer composition may have explained this behaviour, influenced by analytical limitations. In one sample, there was an interaction layer primarily composed of Cr, Mo, Ni, Nb and O, with a top layer containing Ni and S. In contrast, the other sample exhibited a compact layer that had a lower Mo and Nb content in the interaction layer. However, it was essential to consider the possibility that this difference could be influenced by analytical limitations, such as spectral line proximity and the limited thickness of the remaining interaction layer on one of the two samples tested.

Another uncertain behaviour was exhibited by the **IN625 additive and IN625 additive with weld**, as indicated by the mass gain. These samples showed quite high mass gain after 2000h, and the corrosion growth appears to intensify over time. The interaction layer composition significantly differed between the two samples (additive and additive with weld) probably because of their different chemical compositions. In particular,

the interaction layer of the welded sample contained more Mo and Cr respect to the as built one. The lower corrosion level of the IN625_additive with weld sample respect to the additive one could be explained by this difference and the absence of any corrosion deposit in the welded area.

However, when comparing the alloys **IN625, IN725** and **IN718**, a similar interaction layer was observed. In each case, it was a bilayer with an overall thickness of tens of microns: the outer layer was notably rich in S and Ni, while the inner layer was rich in O, Cr, S, Nb and Mo. A noticeable distinction was that the interaction layer was continuous in the case of IN625 and more localized in the case of IN718. Considering IN625 and IN718 samples produced by additive manufacturing, the interaction layer was more widespread and pronounced in IN625. Similarly, the interaction of fluid with IN725 also produced a bilayer, where the outer layer was again nickel sulphide and the inner layer contained the same elements identified in other Inconel alloys but in different percentages. Specifically, compared to forged 718, the innermost interaction layer contained slightly more O, Cr, and Nb, and slightly less S, Ni, and Mo.

Finally, the SiO2 by PECVD coating also demonstrated a similar behaviour for both tested samples. However, in this case, the mass gain growth did not show any time-dependent deceleration. In fact, a thick layer of non-protective iron oxide had formed externally to the sample.

Conclusively, it was confirmed that no localized or intergranular corrosion was detected, and no cracks were identified in the HAZ of the welded samples (IN625 additive with weld and IN718 additive with weld) that could be related to the contact with 80%CO_2+20%SO_2 at 550°C.

Based on the results just presented and particularly noting the beneficial effect of a high quantity of Co and Ni, it had been decided to conduct a more in-depth analysis on alloys and coatings with high Co and Ni content in the same atmosphere.

CHAPTER 7 THIRD TEST CAMPAIGN RESULTS ON THE COMPATIBILITY PRIMARILY OF MIXTURES CONTAINING $80\%CO_2+20\%SO_2$

The third test campaign was carried out in the same way as the second one; however, after 118 hours at 550°C, an abnormal drop in pressure was recorded, leading to the termination of the test. The samples removed from the vessel appeared to be covered with a brittle dark deposit lining also the internal wall of the vessel (Figure 79Figure 80). In order to ascertain the cause of the pressure drop, some analyses were performed on the samples that appeared to be more severely damaged. The analysis was performed on samples before and after a gentle cleaning operation to remove the deposits.

Figure 79 – The appearance of the pressure vessel after 118 h at 550°C

Figure 80 – The appearance of rod, spacers and samples after 118 h at 550°C

Table 28 shows the mass gain of samples before and after cleaning.

Sample	Before cleaning mg/cm² (118h)	After cleaning mg/cm² (118h)	Percentage Change %
Nimonic	1.45	0.73	-49.6
L605	1.18	0.30	-74.2
740H	21.50	0.10	-99.5
740H	0.64	0.33	-47.5
Stellite Cladding 1	0.73	0.39	-46.9
Stellite Cladding 2	1.18		
Stellite cast 6	0.33	0.29	-13.7
MCrAlY PVD	1.66	0.79	-52.3
MCrAlY PVD	1.18	0.44	-62.2
L605 HVOF wasp	5.36	2.28	-57.4
CrCNiCr wasp HVOF 1	4.87	2.74	-43.8
CrCNiCr wasp HVOF 2	7.32	5.20	-29.0
CrC wasp base Co HVOF 1	5.54	4.01	-27.6
CrC wasp base Co HVOF 2	6.01	4.54	-24.5
G130	4.01	0.22	-94.4
AlCrO by PVD	0.51	0.18	-64.3
CrNO by PVD 1	0.23	-0.12	-154.4
CrNO by PVD 2	0.43	0.14	-67.1

Table 28 - Third test campaign - Mass gain values before and after cleaning and variation percentage

As expected, for all samples the mass gain values decreased after cleaning, especially in the case of samples **G130 C8, AlCrO by PVD C3, CrNO by PVD 1 and CrNO by PVD 2.**

The weight increments of these samples were extremely low, confirming the good results of the previous test campaign, i.e., their high corrosion resistance to the sCO_2-20%SO_2 blend.

On the other hand, the mass gain values of all HVOF-coated samples remained very high, regardless of the type of metal matrix or substrate considered. Therefore, the analysis focused on these samples. In particular, the analysis was carried out on the two worst cases:

- **CrC-NiCr WASP HVOF C2,**
- **CrC WASP BASE Co HVOF C2.**

The initial visual inspection of samples surfaces suggested that **stellite cladding** samples had experienced a strong interaction with the fluid, with the peeling of the coating and the formation of detached particles in form of fine “chips” (Figure 81). Therefore, this material was subjected to analysis.

Stellite Cladding (Sample1) **Stellite Cladding (Sample2)**

Figure 81- Appearance of stellite cladding after 118h at 550°C

The "peeled particles" on the surface were identified by using SEM. They were found to be a carbonaceous deposit containing O and S, which were the constituents of the gas, not related to the satellite cladding (Figure 82).

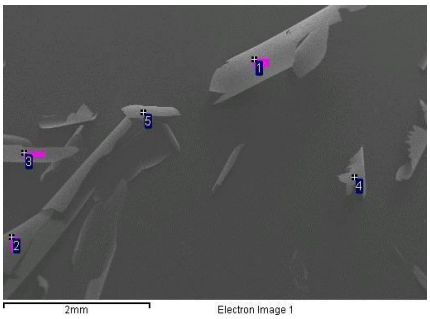

	C	O	S
1	82.74	12.76	4.50
2	89.57	5.27	5.15
3	83.26	13.59	3.15
4	78.14	18.44	3.42
5	87.56	9.38	3.06

Figure 82 – Chemical composition of curls on Stellite Cladding (wt.%)

The SEM-EDS analysis of the cross-section of the samples confirmed almost no interaction of fluid with the cladding (Figure 83). The one that remained attached to the sample was primarily chromium oxide with traces of C, S, Fe and Co. The other layer that detached contained S, C, Co, Cr and Fe. On the other side of the sample there was a single interaction layer primarily composed of C, O, S, Cr and Co.

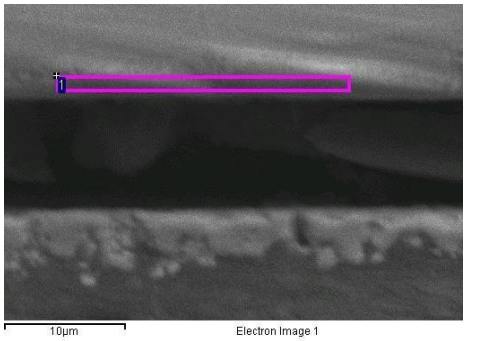

	C	O	Si	S	Cr	Fe	Co	W
1	5.37	24.77	1.31	5.42	36.87	9.98	11.42	4.85

(a)

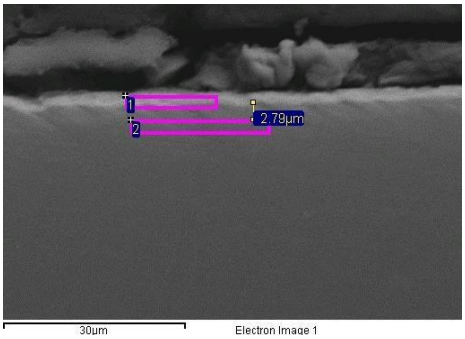

	C	O	Si	S	Ca	Cr	Fe	Co	W
1	33.57	27.77	0.61	7.96	0.39	15.62	1.18	10.48	2.42
2	14.23		1.43			28.86	2.43	47.80	5.25

(b)

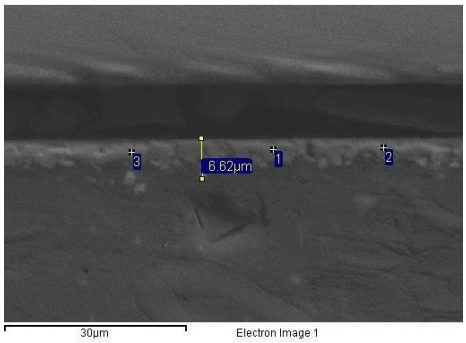

	C	S	Cr	Fe	Co
1	14.79	33.70	7.15	7.08	37.28
2	23.73	35.44	15.33	10.17	15.33
3	8.82	40.47	6.68	41.07	2.96

(a)

Figure 83 – SEM – EDS cross section of one side (a) and the other side (b) (wt.%)

In conclusion, the interaction was limited and these samples cannot be considered the cause of the gas interaction and degradation.

The SEM analysis of sample **CrC wasp base Co HVOF C2** is shown in Figure 84.

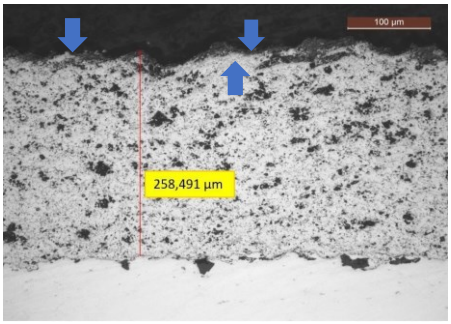

(a)

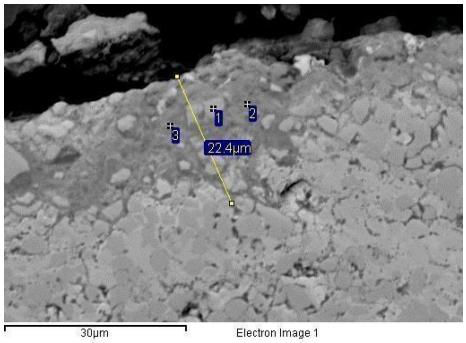

	C	O	Al	S	Cr	Co	Ni
1	23.09				76.91		
2	12.29	35.63	4.31	4.76	35.21	4.70	3.09
3	16.13	29.61	0.53		51.34	2.39	

(b)

Figure 84 -Optical (a) and SEM-EDS cross section analysis (b) of CrC wasp base Co HVOF C2 (wt.%)

The HVOF coating had a thickness of approximately 260 microns and appeared continuous, but very porous. On its external surface, there were some clear signs of interaction with the gas mixture (see the blue arrows in Figure 84). The interaction layer has a thickness of about 20 µm, but it could have been even thicker before the cleaning step. This altered layer is primarily composed of oxides, mainly chromium oxide, and some sulphides. Additionally, there are abnormal levels of aluminum and nickel that should not be present in the HVOF matrix (i.e., the matrix should contain only cobalt).

Despite thermodynamic calculations indicating that chromium carbides (CrC) can also interact with CO gas, a significant portion of them remain intact despite the matrix interaction.

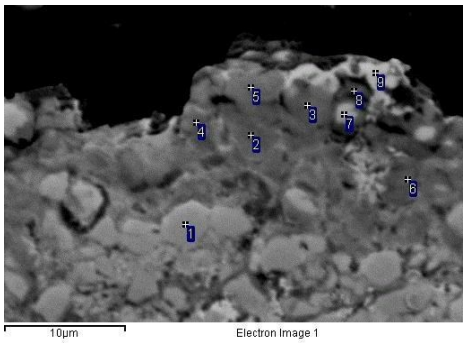

	C	O	Al	S	Cr	Co	Ni
1	23.86				76.14		
2	16.13	32.63		4.58	39.24	5.23	2.20
3	13.24	34.70	1.62	4.55	38.73	3.78	3.38
4	14.71	29.99		4.09	43.67	5.06	2.50
5	17.44	34.89		4.63	35.91	5.28	1.85
6	16.02	29.32			53.63	1.04	
7	23.62	8.30			68.08		
8	28.16	30.50	2.52	4.87	22.47	3.85	7.63
9	25.88			25.09	3.05	8.58	37.41

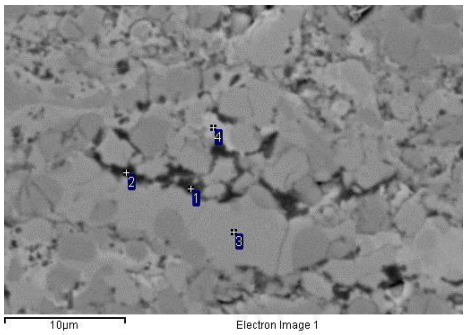

	C	O	Al	Cr	Co	Ni
1		20.73	36.89	34.42	5.69	2.27
2		11.45	31.79	45.56	7.91	3.28
3	16.04			63.25	15.04	5.67
4			5.08	10.47	27.27	57.18

Figure 85 – SEM-EDS cross-section - CrC wasp base Co HVOF C2 (wt.%)

Further analyses confirmed that the matrix was more easily attacked compared to the carbides. Moreover, some analyses carried out in the middle of the coating revealed that it contained Cr, Co and Ni instead of just Co (Figure 85). Moreover, some of what appeared to be porosities were aluminum oxides. To understand if these oxides were pre-existing in the coating or were the result of gas interaction that penetrated through the pores and reacted with the aluminum presented in the sample, SEM-EDS analyses were performed at various depths in the cross section.

The results did not show a clear oxidation gradient that could be a consequence of gas penetration from outside. Moreover, at the interface between the coating and substrate, coarse and angular particles of aluminum oxide were detected. These results confirmed that the aluminium oxides come from the sandblasting pretreatment based on the use of alumina particles to enhance the HVOF coating adhesion (Figure 86).

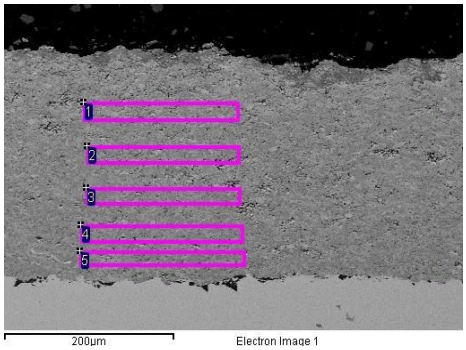

	C	O	Al	Cr	Co	Ni
1	15.57	4.95	3.36	56.61	9.80	9.71
2	15.91	4.13	2.99	59.50	8.88	8.59
3	16.40	4.33	3.00	58.82	9.14	8.31
4	15.00	2.90	3.59	59.67	10.05	8.79
5	16.13	3.91	2.92	59.23	9.14	8.66

(a)

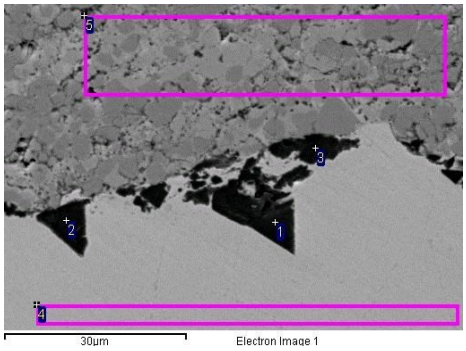

	C	O	Al	Ti	Cr	Fe	Co	Ni
1		47.96	50.52					1.52
2		47.03	52.97					
3		45.41	52.45		2.13			
4			2.40	3.17	20.83	1.27	13.48	58.85
5	14.03	3.60	3.07		60.42		10.13	8.75

(b)

Figure 86 - SEM-EDS cross-section - CrC wasp base Co HVOF C2 (wt.%)

Finally, the **CrC-NiCr WASP HVOF C2** sample has been analysed by optical microscope and SEM-EDS technique (Figure 87Figure 88).

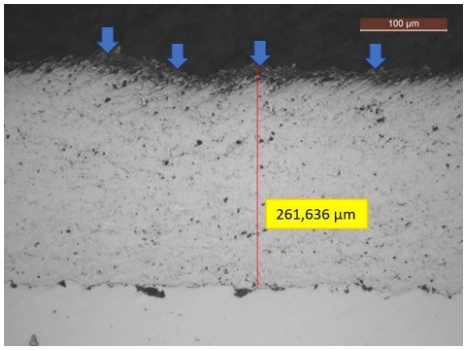

(a)

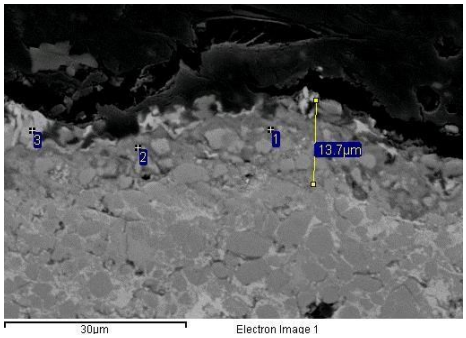

	C	O	S	Cr	Ni
1	13.81	39.97	2.51	42.33	1.38
2	13.84	37.66	2.67	44.01	1.82
3			34.16	4.34	61.50

(b)

Figure 87 - Optical (a) and SEM-EDS cross section analysis (b) of CrC-NiCr WASP HVOF C2 (wt.%)

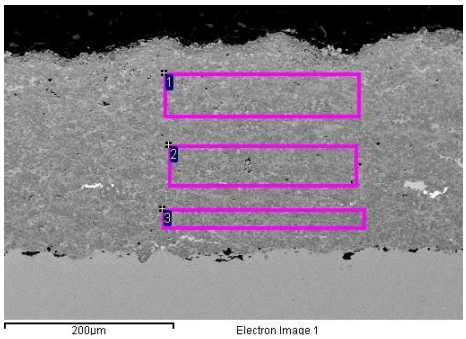

	C	O	Cr	Ni
1	16.49	4.53	58.36	20.62
2	15.77	3.07	60.69	20.46
3	17.22	3.12	59.98	19.68

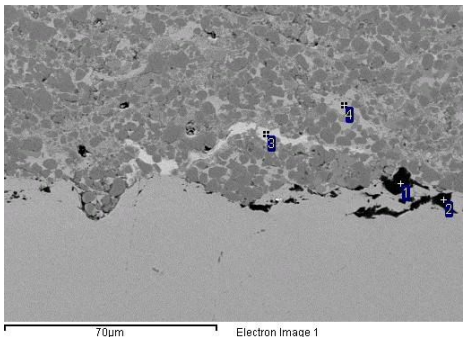

	C	O	Cr	Ni
1	16.49	4.53	58.36	20.62
2	15.77	3.07	60.69	20.46
3	17.22	3.12	59.98	19.68

Figure 88- SEM-EDS cross-section - CrC-NiCr WASP HVOF C2 (wt.%)

In this case as well, the coating had a thickness of approximately 260 microns and appeared continuous and porous, but less than the previous one. There were noticeable signs of interaction with the gas mixture on its external surface (see the blue arrows in Figure 87). The interaction layer had a slightly thinner thickness, approximately 15 µm (or more), probably because of the lower porosity.

It was primarily composed of oxides, mainly chromium oxide and some sulphides. Notably, nickel sulphides were mainly localized in the outermost layer. Once again, chromium carbides (CrC) appeared to resist the gas interaction better than the matrix, which in this case consisted of a Ni-Cr alloy as confirmed by the SEM-EDS analysis. Lastly, it's worth noting the sporadic presence of areas rich in Co and W within the coating, likely attributable to contamination from the powders used in the HVOF process.

In **conclusion,** this analysis revealed that both samples coated with the HVOF technique, particularly their metallic matrix, interacted with the mixture. Despite the confirmed interaction from cross-sectional analyses, the involved layer was limited and insufficient to fully explain the fluid decomposition. Conversely, the significant weight increases recorded, even after cleaning, could be attributed to the coating's porosity, potentially filled with decomposition products. Based on the results obtained, these samples emerge as a plausible factor contributing to the observed pressure drop Further assessments are needed for confirmation. However, future tests will be performed without this kind of samples.

CONCLUSIONS

In a scenario marked by the escalating global climate crisis, the shift from conventional to sustainable energy sources becomes imperative. Concentrated Solar Power (CSP) stands out as a promising solution, utilizing the concentration of solar energy to generate electricity. This approach effectively tackles the challenge of energy intermittency, ensuring a dispatchable electricity supply.

CSP encompasses various technologies, such as Parabolic Troughs, Linear Fresnel, Solar Towers and Parabolic Dish Systems, each with its unique features and advantages. Despite their potential, CSP technologies face challenges, prompting ongoing research to enhance their efficiency and economic viability. A significant breakthrough in this field occurred when supercritical carbon dioxide replaced steam as the working fluid.

This has enabled simplification of the design and cost reduction. However, challenges persist with this technology. In fact, with few exceptions in favourable regions, the Levelized Cost of Electricity (LCoE) currently stands at €150/MWh, significantly surpassing the target of €100/MWh. Additionally, issues arise with ambient temperatures. When the ambient temperature is higher or approaches 31°C, corresponding to the critical point of CO_2, the condensing cycle, which allows for a 10% efficiency increase compared to a non-condensing cycle, cannot be applied. Consequently, to address this issue, numerous research and projects propose raising the critical temperature of carbon dioxide by introducing specific dopants.

In this thesis, the primary aim was to explore novel, efficient and thermally stable dopants for blending with carbon dioxide. The selection of these dopants was not arbitrary; rather, it had to adhere to specific criteria: a critical temperature surpassing 50-100°C to enable a condensing cycle; thermal stability exceeding 550°C and a high binding energy to prevent technical issues in the components of the CSP power block; a low critical pressure to facilitate the design of mechanical components; solubility with carbon dioxide to form the mixture and high molecular complexity to minimize the difference in heat capacity between the two sides of the recuperator. Furthermore, careful consideration was given to NFPA 704, a safety labelling system used to identify the hazards of hazardous materials, ensuring that the selected dopants posed minimal possible risks. Six dopants were identified: $TiCl_4$, $SiCl_4$, SO_2, C_6F_6, C_4F_{10}, and Novec4710. However, $TiCl_4$ was promptly excluded due to its extreme reactivity.

Concerning the remaining dopants, their thermal stability was assessed through laboratory tests and the advantages in terms of power block efficiency compared to the pure supercritical CO_2 cycles were assessed through a preliminary simulation analysis carried out with Aspen Plus v12.0 Software. These analysis showed that the adoption of the considered CO_2 mixtures yields power block efficiencies comparable or even exceeding those of the state of the art technologies.

However, the stability of the mixtures can also be influenced by the materials they are in contact, eventually leading to interactions that induce adverse effects on the performance of power plants, especially in areas with higher temperatures. Therefore, it is important to address the challenge of material compatibility, particularly focusing on metallic materials, such as Fe and Ni-based alloys, in the presence of high-temperature CO_2 mixtures. In fact, while there are existing studies on material compatibility with steam and supercritical carbon dioxide in power plants, there is a noticeable lack of research regarding mixtures of supercritical carbon dioxide. The only exceptions were studies that considered the presence of CO_2 contaminants at very low percentages and lower temperatures than those typical of power plants.

For this reasons, high temperature corrosion tests have been performed on several materials in contact with the selected mixtures, in order to define most promising ones. In total, n°4 tests campaigns were performed, each with its specific procedure.

Preliminary tests were conducted on a welded pressure vessel made of different materials (IN625, AISI 316 and AISI 304) to assess the interaction of sCO_2 mixtures, particularly those containing fluorocarbons like C_6F_6 and C_4F_{10}, with the vessel's cylindrical body and welds at temperatures around 500-600°C for 300h. The metallographic analysis revealed that the introduction of fluorine-bearing gases (i.e. gas containing fluorine) into sCO_2 caused significant metal corrosion and interaction, characterized by a uniform pattern of intergranular corrosion influenced by temperature and different reactivity of the distinct fluorine compound present in the mixture. IN625 exhibited superior resistance to fluorine attack compared to AISI 316, but encountered significant issues in the weldments, developing long intergranular cracks in the Heat-Affected Zone (HAZ). AISI316, despite being in the sensitization range, did not exhibit this problem. AISI304 was exposed only a pure sCO_2 showing results consistent with existing scientific literature. Two additional sCO_2 mixtures containing $SiCl_4$ and SO_2 were examined and their interaction with the materials was limited, with no intergranular cracks or localized corrosion observed. The decision was made to further investigate these mixtures due to their favourable outcomes.

In the **first test campaign** the experimental setup was modified to analyse multiple samples simultaneously. IN625, IN718, IN725 and G130 alloys were tested in form of discs mounted on an alumina rod and placed inside two pressure vessels. The two promising mixtures (containing $SiCl_4$ and SO_2) were tested in pressure vessels made of IN625 at 550°C for about 600 hours and samples were weighed before and after the test for mass change calculations. In the **$SiCl_4$ mixture**, additive-manufactured IN625 demonstrated substantial mass gains, whereas IN718 and both forged and casted IN625 exhibited promising outcomes. Minimal interaction was observed in IN725 samples, whereas G130 experienced complete disintegration. Surface analyses revealed consistent composition in the interaction layers, spanning a few microns, across the various samples, characterized by the presence of O, Si, Cl, Ni and Cr. Noteworthy distinctions were observed in IN718, where a slight intergranular attack was identified beneath the interaction layer on the surface, and in G130, which underwent complete disintegration. In the **SO_2 mixture**, IN625_additive, IN725, IN718 and G130 exhibited reduced mass gains, contrasting with ASTM A494 CW6MC and forged IN625, which displayed higher mass gains. Despite variations in mass gain measurements, surface and cross-sections analysis revealed consistent features among all samples. Specifically, a double interaction layer with an overall thickness of a few tens of microns was observed in each case. This dual-layer structure included an outer layer rich in S and Ni and an inner layer rich in O, S, Cr, and Ni, with minor amounts of Nb and Mo. Notable distinctions were identified in IN718, where the interaction layer was localized only in areas where the protective layer had broken down, and in G130, which exhibited a single and thin interaction layer, demonstrating superior protective characteristics compared to the other samples. A further evaluation of the SO_2-containing mixture was deemed necessary, prompted by the noteworthy interaction observed in G130 exposed to $SiCl_4$. This decision was substantiated by the predominant emphasis on the SO_2 mixture within the existing scientific literature.

The **second test campaign**, began with a refined procedure to evaluate the corrosion kinetics of samples under CO_2+SO_2 mixture at 120°C and 550°C using a dismountable vessel. At **120°C**, minimal weight changes were observed for all the tested samples, indicating limited interaction.

Conversely, at **550°C**, significant mass gains were evident after 600 hours, suggesting increased mixture aggressiveness at elevated temperature. Alloys with **high cobalt and nickel content**, such as G130 and Waspaloy, performed well due to the parabolic sulfurization of cobalt and its slower reaction rate in sulfur-rich atmospheres compared to nickel and iron. For these alloys the interaction was primarily due to oxygen, with traces of sulfur, and some elements (C, Co, Cr, Ni) were present in the interaction layer, which contained porosities. **Coatings** like AlCrO by PVD and CrNO by PVD exhibited notable resistance, likely due to the presence of chromia or alumina layers, although sulfur ions could penetrate these layers over time forming sulphides. **IN725** showed acceptable performance. **IN625_additive** and IN718_additive displayed uncertain behavior, and **Carbonitriding and Full SiO_2** showed negative performance. Comparing IN625, IN725, and

IN718 alloys, a consistent bilayer interaction was identified, characterized by an outer layer enriched in S and Ni and an inner layer enriched in O, Cr, S and Mo, with variations in thickness. No localized or intergranular corrosion was detected in welded samples exposed to both mixtures. Based on these findings, a more in-depth analysis on alloys and coatings with high Co and Ni content in the same atmosphere was deemed necessary.

During the **third test campaign**, a noticeable pressure drop was observed after 118 hours of testing, leading to an investigation of the most implicated samples. **Stellite cladding** showed minimal interaction, as evidenced by cross-section analysis that revealed a thin double interaction layer rich in Cr, O, C; S and Fe inside and S, C, Co; Cr, Fe outside. On the contrary, the **HVOF-coated samples** displayed significant interaction featuring an interaction layer predominantly composed of chromium oxides and sulphides. The HVOF-coated samples were excluded from subsequent testing phases.

Consider that, starting from the second test campaign, the methodology used for the experiments aimed to align with the literature on pure supercritical CO_2. As previously mentioned, methodological discrepancies exist in these studies. Some studies use longer exposure times than those utilized in this thesis, others explore high pressures, while some approach use room conditions as, for most of the researches, pressure seems to have a negligible effect on material resistance in sCO_2 conditions. The majority of studies in the literature consider the presence of flow rate. However, in some of these studies, the flow rate is so low that it is explicitly stated that the described conditions approximate a static fluid. However, considering the innovative nature of this topic, a standardized testing procedure does not exist. Over time, improvements to the method may be possible. Certainly, enhancing fluid flow would represent a step towards, better approximating the actual operational conditions of a power plant, where the fluid is typically in motion. The current process for testing materials cannot be significantly accelerated because it must be carried out step by step. However, future technological progress and research in the field may lead to innovative and faster solutions.

Finally, as an appendix to the thesis, the design of a dismountable pressure vessel capable of withstanding 700°C and 100 bar was presented. These conditions exceeded the regulations outlined in SECTION VIII of the ASME Boiler and Pressure Vessel Code - Division 1, thus requiring and “ad hoc” design. The need for this design arose at the beginning of the PHD work when assessing possible test setups, recognizing the necessity for a dissassemblable pressure vessel as an alternative to another vessel commissioned from a company. However, due to the high manufacturing costs, the restricted number of components that would be commissioned and the precision required for aligning the vessel holes with the vessel-fluid connection apparatus made the actual construction of this component impractical.

Within this thesis, some critical aspects had come to light. A primary concern pertains to the test performed after 600 hours in the initial two test campaigns. When comparing similar materials under similar conditions, such as IN718, a disparity in mass gain values and heterogeneity in the observed interaction within the cross-section become evident in the form of markedly different interactions within the cross-section, with sporadic points in the first test campaign and a widespread formation of pits in the second campaign. It appears that the corrosive phenomenon is in a more advanced stage in the second test, although the reason for this difference remains unclear.

Significantly, the static nature of the tests is noteworthy, necessitating the refilling of barrels and the potential for residual gas decomposition on samples, leading to an overestimation of mass gain.

Therefore, considering these challenges, potential future developments could involve the utilization of a dynamic gas flow in the tests.

Furthermore, since a category of promising materials has been identified, it would be prudent to delve deeper into analyses of other materials and coatings sharing these specific characteristics to obtain more robust and informative results.

Analyzing the results of the initial testing campaign, it may be worthwhile to investigate the reason behind the G130 exhibiting such contrasting behaviors in response to exposure to SO_2 or $SiCl_4$- containing mixture.

Finally, upon examining the results of the IN718 samples produced through additive manufacturing and forging in the second test campaign, it would be intriguing to delve into the factors contributing to distinct production technologies yielding different behaviors, with additive manufacturing exhibiting superior performance.

APPENDIX: PRESSURE VESSEL DESIGN

In order to address the challenge of material compatibility, it is common practice to expose samples of various materials to supercritical blends within a pressure vessel. Thus, this PhD research not only focuses on investigating material compatibility but also involves the design of a novel openable pressure vessel that can withstand the high temperatures commonly encountered in power plants utilizing this particular working fluid.

I. OPENABLE PRESSURE VESSEL

After conducting an in-depth analysis of the existing literature on pressure vessels, an innovative openable pressure vessel capable of withstanding the high temperatures (700 °C) and pressures (100 bar) typical of such power plants was designed. The analysis was validated through both analytical calculations and finite element method.

i. CARACTERISTICS OF THE COMPONENT

The openable pressure vessel consists of a 177 mm long cylindrical body enclosed by two hemispherical ends, reaching approximately 211 mm in length. The wall thickness is uniform at 5 mm for both the cylindrical body and the ends. The outer diameter of the shell measures 48.14 mm, while the inner diameter is 38.14 mm (Figure 89). In this case as well, its dimensions are such that it can fit inside an oven with dimensions of 210x150x310 mm. Inside it, a sample holder will be placed to host the samples that will be tested.

Figure 89 – Openable pressure vessel

ii. SELECTION OF MATERIALS

The selection of a material suitable for high-temperature supercritical carbon dioxide environments began with an extensive literature review [171-172]. Ultimately, Nickel Alloy 625 (UNS N06625/W.Nr. 2.4856) was chosen due to its favorable characteristics: exceptional corrosion resistance, widespread availability, cost-effectiveness, high static and fatigue strength, corrosion resistance and creep resistance within a temperature range of -196°C to 982°C [173]. The alloy's strength is attributed to the presence of molybdenum

and niobium, which reinforce the nickel-chromium matrix. Moreover, alloy 625 is capable of withstanding various corrosive environments, including seawater, neutral salts, and alkaline media, thanks to its alloying elements. Nickel and chromium contribute to resistance against oxidizing environments, while nickel and molybdenum provide resistance in nonoxidizing environments, particularly against pitting and crevice corrosion. Niobium plays a role in preventing weld sensitization and the formation of intergranular cracks. Relevant properties of this nickel-based alloy, determined on hot-rolled bars or rods, are detailed in Table 29 at both room temperature and 760°C [173]. Given the high-temperature application, the material's performance at elevated temperatures will be considered in the sizing of the pressure vessel.

Material	Young Modulus (MPa)	Yield strength (MPa)	Poisson coefficient
Alloy 625 RT	207532	738	0.278
Alloy 625 760°C	160648	545	0.34

Table 29 – IN625 properties determined on hot-rolled bars or rods

iii. ANALYTICAL DESIGN

This part includes sizing and verifying the main components of the vessel. While fatigue can cause damage and failure, it's not a concern here due to the limited cycles and low usage frequency [174]. Instead, corrosion is a primary consideration, as it can lead to structural issues like lattice deformations, inclusions, and interstitial atoms promoting crack formation, especially in threaded elements. This corrosion-related event results in reduced load capacity due to section reduction and notch effects from pitting [175]. Additionally, also thermo-mechanical aspects are considered [176].

- **Cylinder and Ends sizing**. This part includes verifying the main components of the vessel at the operative conditions: 700°C and 100 bar. Pressure vessel sizing can be approached using two methods based on the thickness-to-diameter ratio. The small thickness sizing method applies when the thickness (s) is less than one-tenth (1/10) of the internal diameter (d) of the vessel. On the other hand, the large thickness sizing method is employed when the thickness (s) exceeds one-tenth (1/10) of the internal diameter (d) of the vessel. In this study, where the vessel thickness is 5 mm, which is close to the limit conditions, both sizing methodologies could be utilized for component sizing.

    - *Small thickness sizing*. The stresses acting on the cylinder are computed as follows:
      $\sigma_\theta = \frac{pd}{2s} \quad \sigma_z = \frac{pd}{4s} \quad \sigma_r = -p$
      Concerning those action on hemispherical ends, they can be calculated as follows:
      $\sigma_\theta = \sigma_z = \frac{pd_f}{4s} \quad \sigma_r = -p$
      Where p represents the internal pressure, d stands for the internal diameter of the pressure vessel, and s denotes the thickness. The three sigma values are depicted in the figure below (Figure 90).

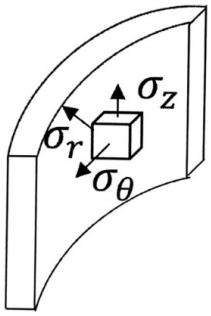

Figure 90 – Stresses

In both cases, the Guest-Tresca criterion is applied for verification.

- *Large thickness sizing*. It is necessary to solve a system obtained from the congruence equations (between the bottom and the shell of the pressure vessel)

$$\begin{cases} (w_{Q,c} + w_{Q,f})Q - w_{M,c}M = w_{p,c} \\ (\varphi_{M,c} + \varphi_{M,f})M - \varphi_{H,c}Q = \varphi_{p,f}p \end{cases}$$

Where all the parameters are best explained in Table 30:

		Cylinder	**Ends**
B	$[Nmm]$	$\frac{Es_c^3}{12(1-\nu^2)}$	$\frac{Es_f^3}{12(1-\nu^2)}$
β	$[N/mm^3]$	$\frac{Es_c}{R^2}$	$\frac{Es_f}{R^2}$
α	$[N/mm]$	$\sqrt[4]{\frac{Es_c}{4R^2B}}$	$\sqrt[4]{\frac{Es_f}{4R^2B}}$
W_p	$[mm]$	$\frac{R^2}{Es_c}$	0
φ_p		0	$\frac{R^3}{8B(1+\nu)}$
W_Q	$[mm]$	$\frac{2\alpha}{\beta}$	$\frac{R(1-\nu)}{Es_f}$
φ_Q		$\frac{2\alpha^2}{\beta}$	0
W_M	$[mm]$	$\frac{2\alpha^2}{\beta}$	0
φ_M		$\frac{4\alpha^3}{\beta}$	$\frac{R}{B(1-\nu)}$

Table 30 - Parameters

$w_{Q,c}$ *is* the parameter W_Q relative to the cylinder; $w_{Q,f}$ *is* the parameter W_Q relative to the ends, $w_{M,c}$ is the parameter W_M relative to the cylinder, $w_{p,c}$ is the parameter W_p relative to the cylinder; $\varphi_{M,c}$ is the parameter φ_M relative to the cylinder; $\varphi_{M,f}$ is the parameter φ_M relative to the ends; $\varphi_{H,c}$ is the parameter φ_Q; $\varphi_{p,f}$ is the parameter φ_p relative to the ends; Q is the radial internal action; M is the internal torsion; p is the pressure; s_c is the thickness of the cylinder and s_f the thickness of the ends. In the case of infinitely rigid ends, the elastic edge coefficients related to the ends are set to zero, resulting in a modification of the previously described system. Solving this modified system allows for the determination of the values of the bending moment, M, and the radial force, Q, at the junction point between the end and the cylinder. This information enables the deduction of the state of stress. By imposing the boundary conditions (x = 0 → M(0) = M0 and Q(0) = -Q0), the stresses can now

be calculated as x varies. Now, the Guest-Tresca resistance criterion can be applied for further verification.

- **Sizing of the bolted flange connection.**

First, the clamping force, Ns, must ensure complete gasket tightening. To ensure this, in consideration of the setup loading (Nset), dependent on the gasket type and material, it is imperative to maintain Ns greater than Nset. Nset is typically calculated as $Nset = Ag * \sigma sn$, where Ag represents the gasket area and σsn signifies the gasket material's yield stress, which is usually supplied by the manufacturer. Bolt tightening generates load through torque application, resulting in a tensile force on the screw stem. This torque Ms can be decomposed into two components: Ms', that operates between the nut and the top face of the flanges and Ms'', that acts on bolt threads, potentially causing torsional stress on the bolt stem. Under pressure, three forces come into play: B (tensile on the bolt), G (compression on the gasket) and P (pressure-induced opening force). Pressure p generates:

$$Ptot = p\,(\pi \frac{Dg^2}{4})$$

where Dg is the vessel section diameter. Assuming linear elastic bolt behavior, forces on bolt B and gasket G are calculated as follows:

$$B = Ns + P\,\frac{kb}{kb + kg} \quad \text{and} \quad G = Ns - P\,\frac{kg}{kg+kb},$$

where kb is bolt stiffness and kg is gasket stiffness.Increasing axial bolt force while decreasing gasket compression reduces opening force P. For a bolted connection with a gasket, two checks are needed during operation: bolt strength using the Guest-Tresca criterion for axial and shear stresses (σ and τ), and gasket sealing. Gasket compression, Gmin, can be conservatively estimated as $Gmin = 2.5 * P * Ag$ and to deem the seal as acceptable, it's essential to ensure that G exceeds the minimum required value, Gmin.

In addition to this theoretical approach, an assessment has been conducted using a procedure outlined in the ASME Section VIII code [177]. In the design of flange bolted connections, industry standards expect calculations under two specific conditions: operative and gasket seating. Operative conditions are considered at the design temperature to ensure that there is enough compression on the gasket to create a secure joint. This is crucial to withstand the pressure applied internally and prevent any leakage. The formula for determining the required bolt load under operative conditions is given as:

$$Wm1 = 0.785\,G^2P + (2b * 3.14\,GmP)$$

Where G represents the diameter at the point where the gasket load reaction occurs, P is the internal design pressure, b stands for the effective width of the gasket or joint contact surface and m is a gasket factor specified according to the gasket type mentioned in the standard.

Gasket seating conditions, on the other hand, come into play during the initial assembly at atmospheric temperature and pressure. The minimum initial bolt load needed for this purpose (Wm2) can be calculated with the following formula:

$$Wm2 = 3.14\,b\,G\,y$$

In this case y denotes the unit seating load for the gasket or joint-contact surface, which is determined by the gasket type specified in the standard.

The bolt load (W) is then determined as the maximum value between Wm1 and Wm2. Starting from this bolt load, it becomes possible to calculate the minimum bolt stress required to withstand the load, leading to the determination of the necessary bolt dimensions.

- **Sizing of the flanges.**
  For the verification of flange strength, it's usual to model them as fixed beams subjected to bending. By applying equilibrium considerations, the moment M can be calculated using the following equation:

$$M = n\,Ns\,l$$

Here, n represents the quantity of bolts, and l signifies the distance between the bolts and the gasket. As the moment M acts across the entire flange circumference, it is possible to assume the bending moment Mb to be equal to M divided by 2π (Mb = M / 2π). With the flange's geometric characteristics known, it becomes feasible to compute the stress value, σb. Subsequently, a comparison can be made with the yield value, σy, in order to confirm that σb remains less than σy.

iv. FINITE ELEMENT METHOD ANALYSIS USING THE THREE-DIMENSIONAL MODELING SOFTWARE SOLIDWORKS

A three-dimensional model of the component was generated, as illustrated in Figure 91.

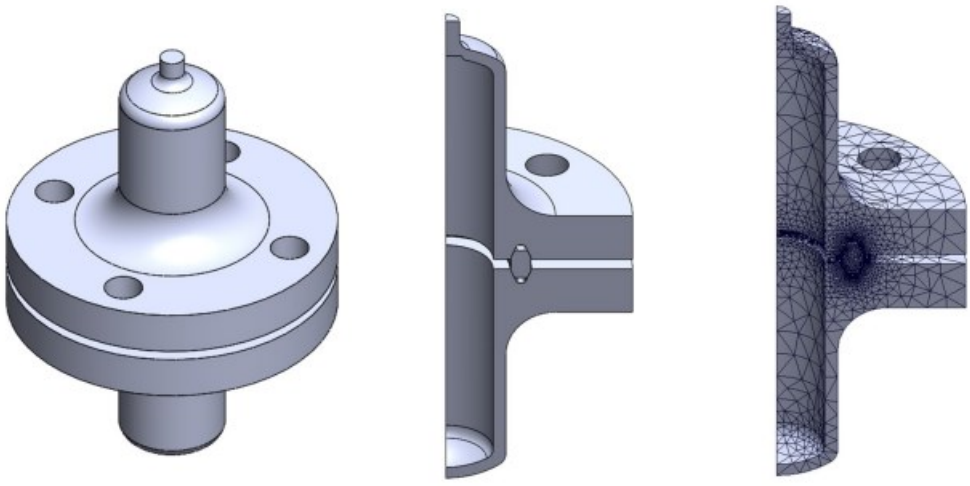

Figure 91 – The three-dimensional model of the openable pressure vessel

To simplify calculations, one-quarter of the pressure vessel was considered, considering its symmetrical characteristics. A mesh with variable densities was created, focusing on finer mesh elements in high-stress areas, particularly near the gasket, where mesh elements measured 0.5 mm and consisted of parabolic tetrahedral elements. For simulation purposes, material properties, applied loads, geometric constraints were defined (Figure 92) and alloy 625 material properties at 760°C, were employed. A uniform pressure of 100 bar was evenly applied to the entire internal surface of the component. A "fixed geometry" constraint was imposed at one end to ensure isostatic conditions. Additionally, symmetry constraints were enforced on the side walls to account for vessel axisymmetry. Finally, a bolt connection was introduced to secure the two

flanges together, utilizing the same material as the vessel. The bolt underwent axial preload calculations following the previously described analytical procedure.

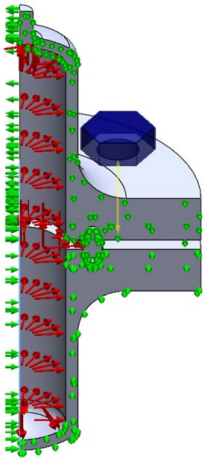

Figure 92 – Position of constraints and applied loads

Guest-Tresca's stress results from the simulation are displayed in Figure 93, while displacements are visualized in Figure 94. Calculation of the safety factor within SOLIDWORKS reveals that, in all regions of the vessel, the safety factor exceeds 2.4, indicating a substantial safety margin against failure and confirming the acceptability of the design.

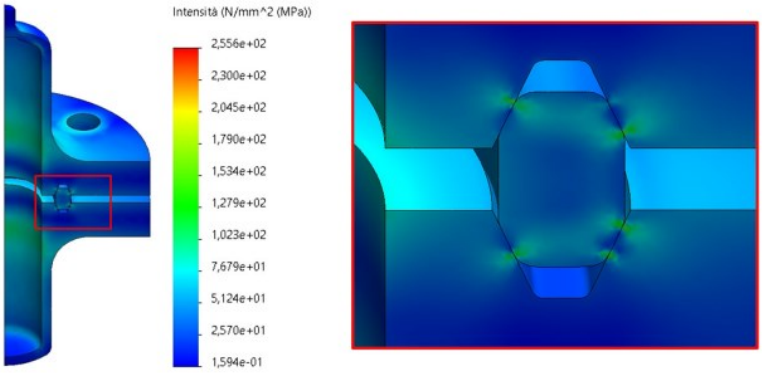

Figure 93 – Guest-Tresca stresses

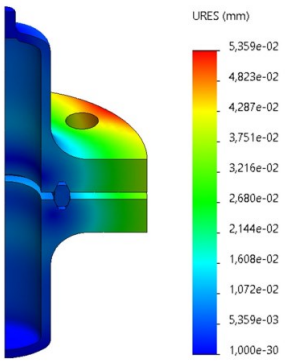

Figure 94 – Displacement

v. DISCUSSION AND CONCLUSION

Both analytical and simulation results confirm the component's acceptability. Finite element method (FEM) simulations provide more precise insights, revealing high-stress regions near the gasket that the analytical method misses. Despite this, the safety factor remains above 2.4 in all areas. The application falls outside ASME B&P Code Section VIII division 1, hence the need for FEM analysis. Developing an openable component is advantageous, with a quick return on investment. Although openable vessels require integrity checks and gasket replacements after each cycle, their environmental impact is lower.

This design can benefit other demountable pressure vessels facing high temperatures and pressures.

BIBLIOGRAPHY

[1] Website "What is Energy Transition?", 2020. URL: https://www.spglobal.com/en/research-insights/articles/what-is-energy-transition

[2] Website "Fossil fuels and climate change: the facts", 2022. URL:https://www.clientearth.org/latest/latest-updates/stories/fossil-fuels-and-climate-change-the-facts/

[3] Website "The greenhouse effect and climate change". URL: https://bio.libretexts.org/Bookshelves/Ecology/Environmental_Science_(Ha_and_Schleiger)/06%3A_Environmental_Impacts/6.03%3A_Climate_Change/6.3.01%3A_The_Greenhouse_Effect_and_Climate_Change

[4] Website "Energy Transition", 2023. URL: https://en.wikipedia.org/wiki/Energy_transition#:~:text=It%20is%20also%20called%20renewable,operate%20on%20low%20carbon%20electricity.

[5] Gielen D., Boshell F., Saygin D., Bazilian M.D., Wagner N. and Gorini R, 2019. "The role of renewable energy in the global energy transformation". Energy Strategy Reviews, 24, pp. 38-50. DOI: https://doi.org/10.1016/j.esr.2019.01.006.

[6] Hemderson J., 2021. "The Energy Transition: Key challenges for incumbent and new players in the global energy system". Oxford Institute for Energy Studies. OIES Paper: RT01.

[7] Website "Energy Transition", 2023. URL: https://www.iea.org/energy-system/energy-efficiency-and-demand/energy-efficiency

[8] Website "Electrification", 2023. URL: https://www.iea.org/energy-system/electricity/electrification

[9] Website "Grid-Scale Storage".2023. URL: https://www.iea.org/energy-system/electricity/grid-scale-storage

[10] Website "Carbon Capture, Utilisation and Storage", 2023. URL: https://www.iea.org/energy-system/carbon-capture-utilisation-and-storage

[11] Oliveira A.M, Beswick R.R and Yan Y., 2021. "A green hydrogen economy for a renewable energy society". Current Opinion in Chemical Engineering, 33, 100701. DOI: https://doi.org/10.1016/j.coche.2021.100701.

[12] Website "Smart Grids", 2023. URL: https://www.iea.org/energy-system/electricity/smart-grids

[13] Website "Renewables", 2023. URL: https://www.iea.org/energy-system/renewables

[14] Mor T., 2018, "Modelling of a Concentrated Solar Power Plant and a Case Study: Turkey". Master Graduation Thesis. URL: https://www.politesi.polimi.it/handle/10589/144160

[15] Website "We could power the entire world by harnessing solar energy from 1% of the Sahara", 2016. URL: https://www.forbes.com/sites/quora/2016/09/22/we-could-power-the-entire-world-by-harnessing-solar-energy-from-1-of-the-sahara/#f7b49e3d4406

[16] Matsuo Y., Yanagisawa A., Yamashita Y., 2013. "A global energy outlook to 2035 with strategic considerations for Asia and Middle East energy supply and demand interdependencies". Energy strategy review 2 (1), pp. 79-91. DOI: https://doi.org/10.1016/j.esr.2013.04.002

[17] Website, 2016. “New report on variable renewables: answers to the integration challenge”. URL: https://www.worldenergy.org/news-views/entry/new-report-on-variable-renewables-answers-to-the-integration-challenge

[18] Scheer H., 1998. “A Solar Manifesto: The Need for a Total Solar Energy Supply – and How to Achieve it”. Published by James and James (Science Publishers), London.

[19] Scheer H., 1999. “The Solar Economy: Renewable Energy for a Sustainable Global Future”. Published by Routledge, London. DOI: https://doi.org/10.4324/9781849773928.

[20] Mazzaferro C.A., 2017. “Life Cycle Assessment of Electricity production from concentrating solar thermal power plants”. URL: https://thesis.unipd.it/retrieve/33ae4d3f-a992-415f-a389-438663cb816e/Alberti_Mazzaferro_Cinzia_1131026.pdf

[21] Isalm R., Bhuiyan A.B.M.N., Ullah M.W., 2017. “An overview of concentrated solar power (CSP) technology and its opportunities in Bangladesh”. International Conference on Electrical, Computer and Communication Engineering (ECCE), Cox's Bazar, Bangladesh. pp. 844-849, DOI: 10.1109/ECACE.2017.7913020.

[22] Website “Concentrating Solar-Thermal Power Basics”. URL: https://www.energy.gov/eere/solar/concentrating-solar-thermal-power-basics#:~:text=CSP%20technologies%20use%20mirrors%20to,an%20engine%20to%20generate%20electricity.

[23] Alami A.H., Olabi A.G., Mdallal A., Rezk A., Radwan A., Rahman S.M.A., Shah S.K., Abdelkareem M.A., 2023. “Concentrating solar power CSP technologies: Status and analysis”. International Journal of Thermofluids, 18, 100340. DOI: https://doi.org/10.1016/j.ijft.2023.100340

[24] Adib R., 2022. “REN21_Renewables 2023 global status report”. URL: RENEWABLES 2023 GLOBAL STATUS REPORT (ren21.net)

[25] Hernandez R.R., Easter S.B., Murphy-Mariscal M.L., Maestre F.T., Tavassoli M., Allen E.B., Barros C.W., Belnap J., Ochoa-Hueso R., Ravi S, Allen M.F., 2014. “Environmental impacts of utility-scale solar energy”. Renewable and Sustainable Energy Reviews, 29, 766-779. DOI: https://doi.org/10.1016/j.rser.2013.08.041

[26] Moore-O’Leary K.A., Hernandez R.R., Johnston D.S., Abella S.R., Tanner K.E., Swanson A.C., Kreitler J., Lovich J.E., 2017. “Sustainability of utility-scale solar energy – critical ecological concepts”. Frontiers in ecology and the environment, 15 (7), 385-394. DOI: https://doi.org/10.1002/fee.1517

[27] Dhar A., Naeth M.A., Jennings P.D., Gamal El-Din M., 2020. “Perspectives on environmental impacts and a land reclamation strategy for solar and wind energy systems”. Science of the Total Environment, 718, 134602. DOI: https://doi.org/10.1016/j.scitotenv.2019.134602

[28] Amin A.Z, 2016. “The Power to Change: Solar and Wind Cost Reduction Potential to 2025", IRENA

[29] Website “Concentrating Solar Powe (CSP) Technologies”, 2023. URL: Concentrating Solar Power (CSP) Technology (anl.gov)

[30] Website “Concentrated solar power (CSP) Vs photovoltaic (PV): an in-depth comparison”,2023. URL: https://www.solarfeeds.com/mag/csp-and-pv-differences-comparison/#:~:text=In%20terms%20of%20energy%20storage%20and%20efficiency%2C%20CSP%20is%20superior,since%20they%20directly%20generate%20electricity.

[31] Website "Concentrated solar power (CSP) vs photovoltaic (PV)", 2019. URL: https://helioscsp.com/concentrated-solar-power-csp-vs-photovoltaic-pv/

[32] Lovegrove K. and Stein W., 2020. "Concentrating Solar Power Technology". DOI: https://doi.org/10.1016/C2018-0-04978-6

[33] Website "The solar project", 2022. URL: https://en.wikipedia.org/wiki/The_Solar_Project

[34] Yan H., Wang A., Chong D., Liu M., Liu J. and Yan J., 2020. "Review on performance analysis of power block in concentrated solar power plants". Energy technology, 9 (1), 2000621. DOI: https://doi.org/10.1002/ente.202000621

[35] Alva G., Lin Y. and Fang G., 2018. "An overview of thermal energy storage systems". Energy, (C), pp. 341-378

[36] Kuravi S., Trahan J., Goswami D. Y., Rahman M. M. and Stefanakos E.K., 2013. "Thermal energy storage technologies and systems for concentrating solar power plants". Progress in energy and combustion science, 39 (4), pp.285-319. DOI: https://doi.org/10.1016/j.pecs.2013.02.001

[37] Mao Q., 2016. "Recent developments in geometrical configurations of thermal energy storage for concentrating solar power plant". Renewable and Sustainable Energy Reviews, 59, pp.320-327. DOI: https://doi.org/10.1016/j.rser.2015.12.355

[38] Medrano M., Gil A., Martorell I., Potau X., Cabeza L.F., 2010. "State of the art on high temperature thermal energy storage for power generation. Part 1—Concepts, materials and modellization". Renewable and Sustainable Energy Reviews, 14, pp. 31-55. DOI: https://doi.org/10.1016/j.rser.2009.07.035

[39] Medrano M., Gil A., Martorell I., Potau X., Cabeza L.F., 2010. "State of the art on high temperature thermal energy storage for power generation. Part 2—Case studies". Renewable and Sustainable Energy Reviews, 14, pp. 56-72. DOI: https://doi.org/10.1016/j.rser.2009.07.036

[40] Mohan G., Venkataraman M.B., Coventry J., 2019. "Sensible energy storage options for concentrating solar power plants operating abobe 600°C". Renewable and Sustainable Energy Reviews, 107, pp. 319-337. DOI: https://doi.org/10.1016/j.rser.2019.01.062

[41] Alva G., Lin Y., Fang G., 2018. "An overview of thermal energy storage systems". Energy, 144, pp. 341-378. DOI: https://doi.org/10.1016/j.energy.2017.12.037

[42] Wu X., Shen J., Li Y., Lee K.Y., 2015. "Steam power plant configuration, design and control". Wiley Interdisciplinary Reviews: Energy and Environment, 4 (6), pp. 537-563. DOI: https://doi.org/10.1002/wene.161

[43] Li J., Bai Y., Li B., 2018. "Operation of air-cooled condensers for optimised back pressure at ambient wind". Appl Therm Eng, 128, pp. 1340-1350. DOI: https://doi.org/10.1016/j.applthermaleng.2017.09.122

[44] Yan H., Wang A., Liu D.C.M., Liu J. and Yan J., 2020. "Review on performance analysis of power block in concentrated solar power plants". Energy Technology, 9 (1), 2000621. DOI: https://doi.org/10.1002/ente.202000621

[45] Tchanche B.F., Lambrinos G., Frangoudakis A., Papadakis G., 2011. "Low-grade heat conversion into power using organic Rankine cycles – A review of various applications". Renewable and Sustainable Energy Reviews, 15, 3963-3979. DOI: https://doi.org/10.1016/j.rser.2011.07.024

[46] Alobaid F., Mertens N., Starkloff R., Lanz T., Heinze C., Epple B., 2017. "Progress in dynamic simulation of thermal power plants". Prog Energ Combust, 59, 79-162. DOI: https://doi.org/10.1016/j.pecs.2016.11.001

[47] Stein W.H., and Buck R., 2017. “Advanced power cycles for concentrated solar power”. Solar Energy, 152, pp. 91-105. DOI: https://doi.org/10.1016/j.solener.2017.04.054

[48] Website “Concentrating solar power projects operational”, 2020. URL: https://solarpaces.nrel.gov/by-status/operational

[49] Dunham, M.T., Iverson, B.D., 2014. “High-efficiency thermodynamic power cycles for concentrated solar power systems”. Renew. Sustain. Energy Rev. 30, pp. 758–770. DOI: https://doi.org/10.1016/j.rser.2013.11.010.

[50] Wright S.A., 2011. “Summary of the Sandia Supercritical CO2 Development Program”. Conference: SCO2 power cycle symposium. Boulder, Colorado, May 24-25. URL: https://www.osti.gov/servlets/purl/1108068

[51] Gini L., Maccarini S., Traverso A., Barberis S., Guedez R., Pesatori E., Bisio V., 2023. “A prototype recuperated supercritical co2 cycle: Part-load and dynamic assessment”. Applied thermal engineering, 225, 120152. DOI: https://doi.org/10.1016/j.applthermaleng.2023.120152

[52] Cho J., Shin H., Cho J., Choi B., Roh C., Lee B., Lee G., Ra H.S and Baik Y.J., 2019. Conference: 3rd European supercritical CO2 Conference, Paris, France, September 19-20. DOI: 10.17185/duepublico/48905

[53] Allison T.C., 2020. “STEP Pilot Plant Advances Supercritical CO2 Power Cycles for Gas-Fired Power Generation”. Southwest Research Institute, San Antonio, TX. URL: https://www.gti.energy/wp-content/uploads/2020/07/STEP-Demo-Advances-sCO2-Power-Cycle-for-Gas-Fired-Power-Generation-Article-Pipeline-Gas-Jrnl-Jul2020.pdf

[54] Moore J., Cich S., Day M., Allison T., Wade J., 2018. “Commissioning of a 1 MWe Supercritical CO2 Test Loop”. Conference: The 6th International Supercritical CO2 Power Cycles Symposium, Pittsburgh, Pennsylvania, March 27-29. URL: https://sco2symposium.com/papers2018/testing/076_Paper.pdf

[55] Rapp L.M., Stapp D., 2019. “Experimental testing of a 1MW sCO2 turbocompressor”. Conference: Experimental Testing of a 1MW sCO2 TurboCompressor. United State, April 1. URL: https://www.osti.gov/servlets/purl/1639901

[56] Invernizzi C.M., 2017. “Prospects of mixtures as working fluids in real-gas brayton cycles”. Energies, 10 (10), pp. 1649. DOI: 10.3390/en10101649

[57] Invernizzi, C.M., Van Der Stelt, T., 2012. “Supercritical and real gas Brayton cycles operating with mixtures of carbon dioxide and hydrocarbons”. Proc. Inst. Mech. Eng. Part A J. Power Energy 226, pp. 682–693. URL: https://doi.org/10.1177/0957650912444689

[58] Website “Concept and ambitions”. URL: https://www.scarabeusproject.eu/concept-and-ambitions/

[59] Website “Activities and dissemination”. URL: https://www.scarabeusproject.eu/

[60] Binotti, Marcoberardino G.D., Iora P., Invernizzi C., Manzolini G., 2020. “Supercritical carbon dioxide/alternative fluid blends for efficiency upgrade of solar power plants”. Conference: AIP Conf. Proc. 2303, 130002. December 11. DOI: https://doi.org/10.1063/5.0028799

[61] Ayub A., Invernizzi C.M., Marcoberardino G.D., Iora P., Manzolini G., 2020. “Carbon Dioxide Mixtures as Working Fluid for High-Temperature Heat Recovery: A Thermodynamic Comparison with Transcritical Organic Rankine Cycles”. Energies 2020, 13(15), pp. 4014. DOI: https://doi.org/10.3390/en13154014

[62] Haaron M., Ayub A., Sheikh N.A., Imran M., 2020. “Exergetic performance and comparative assessment of bottoming power cycles operating with carbon dioxide–based binary mixture as working fluid”. International Journal of Energy Research, 44(10), pp.7957-7973. DOI: https://doi.org/10.1002/er.5173

[63] Liu X., Xu Z., Xie Y., Yang H., 2019. “CO2-based mixture working fluids used for the dry-cooling supercritical Brayton cycle: Thermodynamic evaluation”. Applied thermal engeenering 162, 114226. DOI: https://doi.org/10.1016/j.applthermaleng.2019.114226.

[64] Guo J.Q., Li M.J., Xu J.L., Yan J.J., Wang K., 2019. “Thermodynamic performance analysis of different supercritical Brayton cycles using CO2-based binary mixtures in the molten salt solar power tower systems”. Energy 173, pp. 785-798. DOI: https://doi.org/10.1016/j.energy.2019.02.008.

[65] Shu G., Yu Z., Tian H., Liu P., Xu Z., 2018. “Potential of the transcritical Rankine cycle using CO2-based binary zeotropic mixtures for engine’s waste heat recovery”. Energy conversion and management, 174, pp.668-685. DOI: https://doi.org/10.1016/j.enconman.2018.08.069.

[66] Vesely L., Manikantachari K.R.V, Vasu S., Kapat J., Dostal V., Martin S., 2018. “EFFECT OF IMPURITIES ON COMPRESSOR AND COOLER IN SUPERCRITICAL CO2 CYCLES”. Journal of Energy Resources Technology. DOI: 10.1115/1.4040581

[67] Veseley L., Dostal V., 2017. “Effect of Multicomponent Mixtures on Cycles with Supercritical Carbon Dioxide”. Conference: Proceedings of ASME Turbo Expo 2017: Turbomachinery Technical Conference and Exposition. Charlotte, NC, USA, June 26-30. DOI: https://doi.org/10.1115/GT2017-64044.

[68] Baik S., Lee J.I., 2018. “Preliminary Study of Supercritical CO2 Mixed With Gases for Power Cycle in Warm Environments”. Conference: Proceedings of ASME Turbo Expo 2018. August 30. DOI: https://doi.org/10.1115/GT2018-76386.

[69] Manzolini G., Binotti M., Bonalumia D., Invernizzi C., Iora P., 2019. “CO2 mixtures as innovative working fluid in power cycles applied to solar plants. Techno-economic assessment”. Solar energy, 181, pp. 530-544. DOI: https://doi.org/10.1016/j.solener.2019.01.015

[70] Marcoberardino G.D., Morosini E., Bona D.D., Chiesa P., Invernizzi C., Iora P., Manzolini G., 2022. “Experimental characterisation of CO2 + C6F6 mixture: Thermal stability and vapour liquid equilibrium test for its application in transcritical power cycle”. Applied Thermal Engineering, 212, 118520. DOI: https://doi.org/10.1016/j.applthermaleng.2022.118520.

[71] Morosini E., Ayub A., Marcoberardino G.D., Invernizzi C.M., Iora P., Manzolini G, 2022. “Adoption of the CO2 + SO2 mixture as working fluid for transcritical cycles: A thermodynamic assessment with optimized equation of state”. Energy conversion and management, 255, 115263. DOI: https://doi.org/10.1016/j.enconman.2022.115263

[72] Yang L., Qian H., Kuang W., 2022. “Corrosion Behaviors of Heat-Resisting Alloys in High Temperature Carbon Dioxide”. Materials, 15(4), p.1331. DOI: https://www.mdpi.com/1996-1944/15/4/1331

[73] ISO 8044:2020 Corrosion of metals and alloys. URL: https://www.iso.org/standard/71134.html

[74] Garverick L., 1994. “Corrosion in the Petrochemical Industry”. ASM International. URL: https://www.amazon.com/Corrosion-Petrochemical-Industry-Linda-Garverick/dp/0871705052

[75] Hua, Y., Jonnalagadda, R., Zhang, L., Neville, A., Barker, R., 2017. “Assessment of general and localized corrosion behavior of X65 and 13Cr steels in water-saturated supercritical CO2 environments with SO2/O2”. Int. J. Greenh. Gas Control 64, pp.126–136

[76] Teeter L., Repukaitia R., Huerta N., Oleksak R.P., Thomas R.B., Dogana O.N., Moroza M.Z., Tucker J.D., 2019. “Effect of O2 on the long-term operation and corrosion of steel X65 inCO2-H2O environments for direct supercritical CO2 power cycle applications”. The journal of supercritical fluids, 12, 104520. DOI: https://doi.org/10.1016/j.supflu.2019.04.007

[77] Zhang Y.C., Pang X.L., Qu S.P., Li X., Gao K.W., 2011. “The relationship between fracture toughness of CO2 corrosion scale and corrosion rate of X65 pipeline steel under supercritical CO2 condition”. Int J Greenhouse Gas Control, 5, pp. 1643–1650. DOI: https://doi.org/10.1016/j.ijggc.2011.09.011

[78] Kang Y., Leng X., Zhao L., Bai B., Wang X., Chen H., 2023. “Review on the Corrosion Behaviour of Nickel-Based Alloys in Supercritical Carbon Dioxide under High Temperature and Pressure”. Crystals, 13(5), pp.725. DOI: https://doi.org/10.3390/cryst13050725

[79] Yang, H.; Liu, W.; Gong, B.; Jiang, E.; Huang, Y.; Zhang, G.; Zhao, Y., 2021. “Corrosion behavior of typical structural steels in 500 ℃, 600 ℃ and high pressure supercritical carbon dioxide conditions”. Corrosion Science, 192, 109801. DOI: https://doi.org/10.1016/j.corsci.2021.109801

[80] Bahadori A., 2014. “Corrosion and Materials Selection: A Guide for the Chemical and Petroleum Industries”. URL: https://onlinelibrary.wiley.com/doi/book/10.1002/9781118869215

[81] Meier G.H., Jung K., Mu N., Yanar N.M., Pettit F.S., Abellan J.P., Olszewski T., Hierro L.N., Quadakkers W.J., Holcomb G.R., 2010. “Effect of alloy composition and exposure conditions on the selective oxidation behavior of ferritic Fe-Cr and Fe-Cr-X alloys”. Oxid. Met. 74, pp. 319–340

[82] Di Pietro D., Imbimbo E., Notargiacomo S., 2019. “D3.10 – Materials selection, definition of samples and parameters for corrosion tests”. URL: https://ec.europa.eu/research/participants/documents/downloadPublic?documentIds=080166e5c5595acc&appId=PPGMS

[83] Pint, B.A., Keiser J.R., 2015. ”Initial assessment of Ni-base alloy performance in 0.1 MPa and supercritical CO2”. Jom, 67, pp.2615–2620. DOI: https://doi.org/10.1007/s11837-015-1661-8

[84] Pascal C., Parry V., Fedorova E., Braccini M., Chemelle P., Meyer N., Oquab D., Monceau D., Wouters Y., Mantel M., 2015. “Breakaway oxidation of austenitic stainless steels induced by alloyed sulphur”. Corrion Science, 93, pp.100-108. DOI: https://doi.org/10.1016/j.corsci.2015.01.007

[85] Nguyen, T.D.; Zhang, J.; Young, D.J., 2015. “Effects of cerium and manganese on corrosion of Fe–Cr and Fe–Cr–Ni alloys in Ar–20CO2 and Ar-20CO2-20H2O gases at 650 °C”. Corros. Sci., 100, pp.448-465. DOI: https://doi.org/10.1016/j.corsci.2015.08.012

[86] Oleksak R.P., Addou R., Gwalani B., Baltrus J.P., Liu T., Diulus J.T., Devaraj A., Herman G.S., Dogan O.N., 2021. “Molecular-scale investigation of the oxidation behavior of chromia-forming alloys in high-temperature CO2”. Material degradation, 5(46). URL: Molecular-scale investigation of the oxidation behavior of chromia-forming alloys in high-temperature CO2 | npj Materials Degradation (nature.com)

[87] Rouillard, F.; Moine, G.; Tabarant, M.; Ruiz, J.C., 2011. “Corrosion of 9Cr Steel in CO2 at Intermediate Temperature II: Mechanism of Carburization”. Oxid. Met. 2012, 77, pp. 57–70. URL: Corrosion of 9Cr Steel in CO2 at Intermediate Temperature II: Mechanism of Carburization | SpringerLink

[88] Olivares, R.I.; Young, D.J.; Marvig, P.; Stein, W., 2015. “Alloys SS316 and Hastelloy-C276 in Supercritical CO2 at High Temperature”. Oxid. Met., 84, pp. 585–606. URL: Alloys SS316 and Hastelloy-C276 in Supercritical CO2 at High Temperature | SpringerLink

[89] Subramanian, G.O.; Lee, H.J.; Kim, S.H.; Jang, C., 2018. “Corrosion and Carburization Behaviour of Ni-xCr Binary Alloys in a High-Temperature Supercritical-Carbon Dioxide Environment”. Oxid. Met., 89, pp.683–697. URL: Corrosion and Carburization Behaviour of Ni-xCr Binary Alloys in a High-Temperature Supercritical-Carbon Dioxide Environment | SpringerLink

[90] Oleksak, R.P.; Tylczak, J.H.; Holcomb, G.R.; Doğan, Ö.N., 2019. “90”. Corros. Sci., 157, pp. 20–30. DOI: https://doi.org/10.1016/j.corsci.2019.05.019

[91] Tien, J.K., Jarrett, R.N., 1982. “Effects of Cobalt in Nickel-Base Superalloys”. Springer, Dordrecht. DOI: https://doi.org/10.1007/978-94-009-7907-9_17

[92] Lehmusto, J.; Ievlev, A.V.; Cakmak, E.; Keiser, J.R.; Pint, B.A., 2021. “A Tracer Study on sCO2 Corrosion with Multiple Oxygen-Bearing Impurities”. Oxidation of metals, 96, pp. 571-587. DOI: https://doi.org/10.1007/s11085-021-10071-6

[93] McCarroll I.E., La Fontaine A., Nguyen T.D., Smith A.F., Zhang J., Young D.J., Cairney J.M., 2018. “Performance of an FeCrAl alloy in a high-temperature CO2 environment”. Corrosion Science, 139, pp.267-274. DOI: https://doi.org/10.1016/j.corsci.2018.05.007

[94]Birks N., Meier G.H., Pettit F.S, 2006. “High temperature oxidation of metals”. Cambridge University Press

[95] Olivares, R.I.; Young, D.J.; Marvig, P.; Stein, W., 2015. “Alloys SS316 and Hastelloy-C276 in Supercritical CO2 at High Temperature”. Oxid. Met., 84, pp. 585–606. URL: https://link.springer.com/article/10.1007/s11085-015-9589-5

[96] Johnston G.R., 1982. “Diffusion of chromium and silicon in nickel solid-solution alloys of the Ni-Cr-Si system”, High Temp. High Press 14, pp.695–707.

[97] Bates, H.G.A., 2017. “The Corrosion Behavior of High-Temperature Alloys During Exposure for Times up to 10,000 h in Prototype Nuclear Process Helium at 700 to 900 °C”. Nuclear technology, 66, pp.415-428. DOI: https://doi.org/10.13182/NT84-A33444

[98] Guo X., Liu Z., Li L., Cheng J., Su H., Zhang L., 2022. “Revealing the long-term oxidation and carburization mechanism of 310S SS and Alloy 800H exposed to supercritical carbon dioxide”. Materials characterization, 183, 111603. DOI: https://doi.org/10.1016/j.matchar.2021.111603

[99] Olivares, R.I.; Young, D.J.; Nguyen, T.D.; Marvig, P., 2018. “Resistance of High-Nickel, Heat-Resisting Alloys to Air and to Supercritical CO2 at High Temperatures”. Oxid. Met., 90, pp. 1–25.

[100] Mahaffey J., Brittan A., Anderson M.H., Arik M.N., 2016. “The 5 th International Supercritical CO2 Power Cycles Symposium Effect of Oxygen Impurity on Corrosion in Supercritical CO2 Environments”. Conference: The 5 th International Supercritical CO2 Power Cycles Symposium, March.

[101] He L.F., Roman P., Leng B., Sridharan K., Anderson M., Allen T.R., 2014. “Corrosion behavior of an alumina forming austenitic steel exposed to supercritical carbon dioxide”. Corrosion Science, 82, pp. 67-76. DOI: http://dx.doi.org/10.1016/j.corsci.2013.12.023

[102] Cao G., Firouzdor V., Sridharan K., Anderson M., Allen T.R., 2012. “Corrosion of austenitic alloys in high temperature supercritical carbon dioxide”. Corrosion science, 60, pp. 246-255. DOI: http://dx.doi.org/10.1016/j.corsci.2012.03.029

[103] Pint B.A., Pillai R., Lance M.J., Keiser J.R., 2020. “Effect of Pressure and Thermal Cycling on Long-Term Oxidation in CO2 and Supercritical CO2”. Oxidation of metals, 94, pp. 505-526. DOI: https://doi.org/10.1007/s11085-020-10004-9

[104] Walker M.S., Withey E.A., 2018. “Influence of CO2 Purity on the Corrosion of Structural Alloys for Supercritical CO2 Power Cycles”. Conference: The 6th International Supercritical CO2 Power Cycles Symposium. Pittsburgh, Pennsylvania. March 27-29.

[105] Lee, H.J., Subramanian, G.O., Kim, S.H., Jang, C, 2016. “Effect of pressure on the corrosion and carburization behavior of chromia-forming heat-resistant alloys in high-temperature carbon dioxide environments”. Corrosion science, 111, pp. 649-658. DOI: https://doi.org/10.1016/j.corsci.2016.06.004

[106] Sridharan K., 2013. “Corrosion in Supercritical Carbon Dioxide: Materials, Environmental Purity, Surface Treatments, and Flow Issues”. Project No. 10-872

[107] Pint B.A., Unocic K.A., 2018. “The Effect of CO2 Pressure on Chromia Scale Microstructure at 750°C”. JOM, 70, pp.1511-1519.

[108] Li Q.K., Kutana A., Penev E.S., Yakobson B.I., 2022. “Iron corrosion in the ‘‘inert’’ supercritical CO2, ab initio dynamics insights: How impurities matter ”. Matter, 5(2), pp.751-762. DOI: https://doi.org/10.1016/j.matt.2021.12.019

[109] Young, D.J.; Pint, B., 2006.. “Chromium Volatilization Rates from Cr2O3 Scales into Flowing Gases Containing Water Vapor”. Oxid. Met., 66, pp. 137–153.

[110] Quadakkers W.J., Olszewski T., Piron-Abellan J., Shemet V., Singheiser L., 2023. “Oxidation of Metallic Materials in Simulated CO2/H2O-rich Service Environments Relevant to an Oxyfuel Plant, Materials Science Forum”, Trans Tech Publ, pp. 194–199.

[111] Li K., Zeng Y., Luo J.L., 2021. “Corrosion of SS310 and Alloy 740 in high temperature supercritical CO2 with impurities H2O and O2/ Modelling of the degradation of martensitic stainless steels by the Boudouard reaction”. Corrosion science, 184, 109350. DOI: https://doi.org/10.1016/j.corsci.2021.109350

[112] Mahaffey J., Adam D., Brittan A., Anderson M., Sridharan K., 2016. “Corrosion of Alloy Haynes 230 in High Temperature Supercritical Carbon Dioxide with Oxygen Impurity Additions”. Oxidation of Metals, 86, pp. 567–580

[113] Li K., Zeng Y., Luo J.L., 2021. “Corrosion of SS310 and Alloy 740 in high-temperature supercritical CO2 with impurities H2O and O2”. Corrosion science, 184, pp.109350. DOI: https://doi.org/10.1016/j.corsci.2021.109350

[114] Li K., Zeng Y., Luo J.L., 2020. “Corrosion performance of candidate boiler tube alloys under advanced pressurized oxy-fuel combustion conditions / Steam Oxidation and Chromia Evaporation in Ultra-Supercritical Steam Boilers and Turbines”. Energy, 215(12), 119178

[115] Pint B.A., Lehmusto J., Lance M.J., Keiser J.R., 2019. “Effect of pressure and impurities on oxidation in supercritical CO2”. Materials an corrosion, 70(8), pp. 1400-1409. DOI: https://doi.org/10.1002/maco.201810652

[116] Li K.; Zeng Y.; Luo, J.L., 2021. “Corrosion performance of candidate boiler tube alloys under advanced pressurized oxy-fuel combustion condition”s. Energy, 215, 119178

[117] Otsuka N., 2013. “Carburization of 9% Cr steels in a simulated oxyfuel corrosion environment”. Oxid Metals, 80, pp.565-575.

[118] Mahaffey J., Schroeder A., Adam D., Brittan A., Anderson M., Couet A., Sridarian K., 2018. “Effects of CO and O2 Impurities on Supercritical CO2 Corrosion of Alloy 625”. Metallurgical and Materials Transactions A, 49, pp. 3703–3714

[119] Oleksak R.P., Tylczak J.H., Carney C.S., Holcomb G.R., Dogan O.N., 2018. “High-Temperature Oxidation of Commercial Alloys in Supercritical CO2 and Related Power Cycle Environments”. JOM, 70, pp. 1527–1534

[120] Oleksak R.P., Tylczak J.H., Holcomb G.R., Dogan O.M., 2020. “Temperature-Dependence of Corrosion of Ni-Based Superalloys in Hot CO2-Rich Gases Containing SO2 Impurities”. JOM, 72, pp. 1822–1829

[121] Huczkowski P., Young D. J., Olszewski T., Chyrkin A., Quadakkers W. J., 2017. “Effect of Sulphur on the Oxidation Behaviour of Possible Construction Materials for Heat Exchangers in Oxyfuel Plants in the Temperature Range 550–700 °C”. Oxidation of Metals, 89, pp. 651–681

[122] Nguyen, T.D.; Zhang, J.; Young, D.J., 2015. “Effects of cerium and manganese on corrosion of Fe–Cr and Fe–Cr–Ni alloys in Ar–20CO2 and Ar-20CO2-20H2O gases at 650 °C”. Corros. Sci., 100, pp. 448–465

[123] Brittan A.M., Mahaffey J., Anderson M., Sridharan K., 2018. “Effect of Supercritical CO2 on the Performance of 740H Fusion Welds”. Materials science and engineering:A, 742, pp.414-422. DOI: https://doi.org/10.1016/j.msea.2018.11.029

[124] Brittan A., Mahaffey J., Anderson M., 2019. “The performance of Haynes 282 and its weld in supercritical CO2”. Materials science and engineering: A, 759, pp.770-777. DOI: https://doi.org/10.1016/j.msea.2019.05.080

[125] Nguyen T.D., Peng X., Zhang J., Young D.J., 2017. “Corrosion resistance of chromised and aluminised coatings in wet CO2 gas at 650°C”. Surface and coatings technology, 316, pp. 226-238. DOI: https://doi.org/10.1016/j.surfcoat.2017.03.028

[126] Turchi C., 2014. “10 MW Supercritical CO2 Turbine Test”.

[127] Politecnico di Milano, Kelvion, Abengoa, “Scarabeus: Supercritical CARbon dioxide/Alternative fluids Blends for Efficiency Upgrade of Solar power plants”, 2019-2023, https://www.scarabeusproject.eu/

[128] Politecnico di Milano, “Desolination: DEmonstration of concentrated SOLar power coupled wIth advaNced desAlinaTion system in the gulf region”, 2021-2025, https://desolination.eu/, 10.3030/101022686

[129] Song Y., Li D., Cao F., Wang X., 2017. “Theoretical investigation on the combined and cascade CO2/R134a heat pump systems for space heating”, Applied Thermal Engineering, 124, pp.1457-1470, DOI: https://doi.org/10.1016/j.applthermaleng.2017.06.014

[130] Ayub A., Marcoberardino G., Invernizzi C., Iora P., 2021. “Advanced thermodynamic power cycles utilizing carbon dioxide based mixtures as working fluids for high temperature waste heat recovery”. Conference: The 4th European sCO2 Conference for Energy Systems, online, March 23-24. DOI: 10.17185/duepublico/73947

[131] Nascimento F.P., Paredes M.L.L., Bernardes A.P., Pessoa F.L.P., 2019. “Phase behavior of CO2/toluene, CO2/n-decane and CO2/toluene/n-decane: Experimental measurements and thermodynamic modeling with SAFT-VR Mie equation of state”, The Journal of supercritical fluids, 154, Paper No. 104634. DOI: https://doi.org/10.1016/j.supflu.2019.104634

[132] Putz Y., Grassberger L., Lindner P., Schweins R., Strey R., Sottmann T., 2015. “Unexpected efficiency boosting in CO2-microemulsions: a cyclohexane depletion zone near the fluorinated surfactants evidenced by a systematic SANS contrast variation study”, Phys. Chem. Chem. Phys., 17, pp. 6122-6134. DOI: 10.1039/C4CP05435K

[133] Zhang L., Xu S., Du P., Liu H., 2015. “Experimental and theoretical investigation on the performance of CO2/propane auto-cascade refrigerator with a fractionation heat exchanger”, Applied thermal engineering, 87, pp.669-677. DOI: https://doi.org/10.1016/j.applthermaleng.2015.05.016

[134] Sarkar J., Bhattacharyya S., 2009. “Assessment of blends of CO2 with butane and isobutane as working fluids for heat pump applications”, International journal of thermal sciences, 48, pp.1490-1465. DOI: https://doi.org/10.1016/j.ijthermalsci.2008.12.002

[135] Fiaschi D., Lombardi L., 2002. “Integrated Gasifier Combined Cycle Plant with Integrated CO2 – H2S Removal: Performance Analysis, Life Cycle Assessment and Exergetic Life Cycle Assessment”, International Journal of thermodynamics, 5 (1), pp.13-24. URL: https://dergipark.org.tr/en/pub/ijot/issue/5743/76624

[136] Salah S.I., White M.T., Sayma A.I, 2023. “A Comparison of Flow Path Designs for Axial Turbines Operating with Pure CO2 and CO2 Mixtures”. Conference: turbo expo power for land, sea and air, September 28. DOI: https://doi.org/10.1115/GT2023-101511

[137] Coquelet C., Neyrolles E., Valtz A., Chapoy A., 2022. “On the Phase Behaviour of the CO2 + N2O4 system at low temperatures”. Chemical Engineering Science, 258, DOI: 10.1016/j.ces.2022.117726

[138] Xia D., Xiong J., Zhu M., Chen Q., 2023. “The combined supercritical CO2-based binary mixture Brayton cycle/organic Rankine cycle: a thermodynamic parametric analysis”, Conference: International conference on mechatronics engineering and artificial intelligence. DOI: https://doi.org/10.1117/12.2672656

[139] Bonalumi D., Lasala S., Macchi E., 2020. “CO2-TiCl4 working fluid for high-temperature heat source power cycles and solar application”, Renewable energy, 147, pp.2842-2854. DOI: https://doi.org/10.1016/j.renene.2018.10.018

[140] Wu S., Li Y., Zhao J., Lu C., Wang Z., 2015. “Simultaneous CO2/SO2 adsorption performance of carbide slag in adsorption/desorption cycles”. The Canadian Journal of Chemical Engineering, 94 (1), pp. 33-40. DOI: https://doi.org/10.1002/cjce.22369

[141] Cabaco M.I., Danten Y., Tassaing T., Longelin S., Besnard M., 2005. “Raman spectroscopy of CO2–acetone and CO2–ethanol complexes”, Chemical physical letters, 413 (4-6), pp.258-262. DOI: https://doi.org/10.1016/j.cplett.2005.07.091

[142] Tsivintzelis I., Pavlidou E., Paanayiotou C., 2007. “Biodegradable polymer foams prepared with supercritical CO2–ethanol mixtures as blowing agents”, the journal of supercritical fluids, 42 (2), pp.265-272. DOI: https://doi.org/10.1016/j.supflu.2007.02.009

[143] Wang S., Jiang L., Cheng Z., Liu Y., Zhao J., Song Y., 2021. “Experimental study on the CO2-decane displacement front behavior in high permeability sand evaluated by magnetic resonance imaging”, 217, Paper No. 119433. DOI: https://doi.org/10.1016/j.energy.2020.119433

[144] Song Y.J., Cui X.J., Deng T.S., Zhang F.Q., Fan W.B., 2021. “Solvent effect on the activity of Ru-Co3O4 catalyst for liquid-phase hydrogenation of CO2 into methane”, Journal of fuel chemistry and technology, 49 (2), pp.178-185. DOI: https://doi.org/10.1016/S1872-5813(21)60013-0

[145] Ekambaram, R:, Rajasekaran M., 2023. “Recent Progress in Science and Technology Vol. 3”. URL: https://www.researchgate.net/profile/Chandan-Shaw-3/publication/367473588_Impact_of_Technology_on_the_Sports_Field/links/646dab3837d6625c002c7c8d/Impact-of-Technology-on-the-Sports-Field.pdf#page=71

[146] Favareto R., Pereira J.R:D:, Santana C.C:, Madureira H., Cabrail V.F:, Tavares F.W., Filho L.C., 2010. “High-pressure phase diagram of the drug mitotane in compressed and/or supercritical CO2”, the journal of chemical thermodynamics, 42 (2), pp.286-290. DOI: https://doi.org/10.1016/j.jct.2009.08.017

[147] Marcoberardino G. Di, Morosini E., Bona D. Di, Chiesa P., Invernizzi C., Iora P., Manzolin G., 2022, "Experimental characterisation of CO2 + C6F6 mixture: Thermal stability and vapour liquid equilibrium test for its application in transcritical power cycle", Applied Thermal Engineering, 212, Paper No. 118520, DOI: https://doi.org/10.1016/j.applthermaleng.2022.118520

[148] Invernizzi C., Iora P., Bonalumi D., Macchi E., Roberto R., Caldera M., 2016, "Titanium tetrachloride as novel working fluid for high temperature Rankine Cycles: Thermodynamic analysis and experimental assessment of the thermal stability", Applied Thermal Engineering, 107, pp. 21-27, DOI: 10.1016/j.applthermaleng.2016.06.136

[149] Chen L., Zhang B., Yang T., Deng Y., 2019, "Thermal decomposition characteristics and kinetic analysis of C4F7N/CO2 gas mixture", Journal of Physics D: Applied Physics, 53, Paper No. 055502, DOI: 10.1088/1361-6463/ab56a0

[150] Morosini E., Manzolini G., Di Marcoberardino G., Invernizzi C., Iora P., 2021. "Investigation of CO2 mixtures to overcome the limits of sCO2 cycles". E3S Web of Conferences 312, 08010. DOI: https://doi.org/10.1051/e3sconf/202131208010

[151] Morosini E., Villa E., Quadrio G., Binotti M., Manzolini G., 2023. "Solar tower CSP plants with transcritical cycles based on CO2 mixtures: A sensitivity on storage and power block layoits". Solar Energy, 262, 111777. DOI: https://doi.org/10.1016/j.solener.2023.05.054

[152] Aqel O.A, White M.T., Khader M.A., Sayma A.I., 2021. "Sensitivity of transcritical cycle and turbine design to dopant fraction in CO2-based working fluids". Applied thermal engineering 190, 116796. DOI: https://doi.org/10.1016/j.applthermaleng.2021.116796

[153] Salah S.I., Crespi F., White M.T., Munoz A., Paggini A., Ruggero M., Sanchez D., Sayma A.I., 2023. "Axial turbine flow path for concentrated solar power plants operating with CO2 blends". Applied thermal engineering 230, 120612. DOI: https://doi.org/10.1016/j.applthermaleng.2023.120612

[154] Sun J., Sun C., Wang Y., 2018. "Effects of O2 and SO2 on Water Chemistry Characteristics and Corrosion Behavior of X70 Pipeline Steel in Supercritical CO2 Transport System". Ind. Eng. Chem. Res, 5 (6), 2365-2375. DOI: https://doi.org/10.1021/acs.iecr.7b04870

[155] Hua, Y., Jonnalagadda, R., Zhang, L., Neville, A., Barker, R., 2017. "Assessment of general and localized corrosion behavior of X65 and 13Cr steels in water-saturated supercritical CO2 environments with SO2/O2". Int. J. Greenh. Gas Control 64, 126–136. DOI: https://doi.org/10.1016/j.ijggc.2017.07.012

[156] Farelas F, Choi YS, Nesic S., 2012. "Effect of CO2 phase change, SO2 content and flow on the corrosion of CO2 transmission pipeline steel". Corrosion 2012 conference and expo, 0001322. URL: http://www.icmt.ohio.edu/documents/NACE2012/C2012-0001322.pdf

[157] Teeter, R. Repukaitia, N. Huertaa, R.P. Oleksaka, R.B. Thomasa, Ö.N. Doˇgana, M. Ziomek-Moroza, J.D. Tuckerb, 2019. "Effect of O2 on the long-term operation and corrosion of steel X65 inCO2-H2O environments for direct supercritical CO2 power cycle applications". The journal of Supercritical fluids 152, 104520. DOI: 10.1016/j.supflu.2019.04.007

[158] Wang W., Kuiling S., Shang T., Ruiqing S., Trent P, Wang Q., 2019. "Synergistic effect of O2 and SO2 gas impurities on X70 steel corrosion in water-saturated supercritical CO2". Process Safety and Environmental Protection 130(4). DOI: 10.1016/j.psep.2019.07.017

[159] Li, Y.Y., Wang, Z.Z., Guo, X.P., Zhang, G.A., 2019. "Galvanic corrosion between N80 carbon steel and 13Cr stainless steel under supercritical CO2 conditions". Corros. Sci. 147, 260–272. DOI: 10.1016/j.corsci.2018.11.025

[160] Holcomb G.R, Carney C., Dogan O.N., 2016. “Oxidation of alloys for energy applications in supercritical CO2 and H2O”. Corrosion Science, 109. DOI: https://doi.org/10.1016/j.corsci.2016.03.018

[161] Mahaffey J., Anderson M., Adam D., Sridharan K., 2016. “Effect of Oxygen Impurity on Corrosion in Supercritical CO2 Environments”. The 5 th International Supercritical CO2 Power Cycles Symposium. URL: https://www.researchgate.net/publication/318280935_The_5_th_International_Supercritical_CO2_Power_Cycles_Symposium_Effect_of_Oxygen_Impurity_on_Corrosion_in_Supercritical_CO2_Environments

[162] Oleksak R.P., Tylczak J.H., Carney C.S, Holcomb G.R., Dogan O.N., 2018. “High-Temperature Oxidation of Commercial Alloys in Supercritical CO2 and Related Power Cycle Environments”. JOM, 70 (8). DOI: 10.1007/s11837-018-2952-7

[163] Zhu Z., Cheng Y., Xiao B., Khan H.I., Xu H., Zhang N., 2019. “Corrosion behavior of ferritic and ferritic-martensitic steels in supercritical carbon dioxide”. Energy, 175, 1075-1084. DOI: https://doi.org/10.1016/j.energy.2019.03.146

[164] Coutsouradis D., Davin A., Lamberigts M., 1987 "Cobalt-based Superalloys for Applications in Gas Turbines". Materials science and engineering, 88, pp.11-19. DOI: https://doi.org/10.1016/0025-5416(87)90061-9

[165] Mrowec S., 1995 “The problem of sulfur in high-temperature corrosion”. Oxidation of Metals, 44, pp. 177–209. URL: https://link.springer.com/article/10.1007/BF01046727

[166] Stott F.H., 1989. “The role of active elements in the oxidation behaviour of high temperature metals and alloys”. Springer, Netherlands, Lang E. (editor). DOI: 10.1007/978-94-009-1147-5

[167] Grabke H.J., 2016. “Fundamental aspects of oxidation, sulfidation, chloridation and carburization in the gasifier environment”. Materials at high temperatures, 11 (1-4), pp.23-29. DOI: 10.1080/09603409.1993.11689435

[168] Lobnig R.E., Grabke H.J., 1990. “Mechanisms of simultaneous sulfidation and oxidation of Fe Cr and Fe Cr Ni alloys and of the failure of protective chromia scales”. Corrosion Science, 30 (10), pp. 1045-1071. DOI: https://doi.org/10.1016/0010-938X(90)90211-M

[169] Sha C., Yang L., Cairney J.M., Zhang J., Young D.J., 2023. “Sulphur diffusion through a growing chromia scale and effects of water vapour”. Corrosion science 222, Paper No. 111410. DOI: https://doi.org/10.1016/j.corsci.2023.111410

[170] Hansel M., Quadakkers W., Young D., 2023. “Role of water vapor in chromia-scale growth at low oxygen partial pressure”, Oxid. Met. 59 (3), pp.285–301. URL: https://link.springer.com/article/10.1023/A:1023040010859

[171] Jung Lee, H., Jang, C., Kim, H., J., and Lee, H., 2014, “Compatibility of Candidate Structural Materials in High-Temperature s-CO2 Environment,” The 4th International Symposium - Supercritical CO2 Power Cycles Conference, Pittsburgh, PA, Sept. 9–10, pp. 1–9.

[172] Pint, B. A., Keiser, J. R., and Brese, R. G., 2016, “The Effect of Temperature and Pressure on Supercritical CO2 Compatibility of Conventional Structural Alloys,” Conference: The 5th International Symposium - Supercritical CO2 Power Cycles, San Antonio, TX, Mar. 28–31, Article No. #056.

[173] Special Metals, “INCONEL VR Alloy 625,” Special Metals Corporation, New Hartford, NY.

[174] Mazzoni, A., and Solazzi, L., 2022, “Experimental Field Test on a Multipiece Steel Wheel and Influence of the Material Properties on Its Fatigue Life Evaluation,” Eng. Fail. Anal., 135, Paper No. 106106.

[175] Solazzi, L., Scalmana, R., Gelfi, M., and Vecchia, G. M. L., 2012, “Effect of Different Corrosion Levels on the Mechanical Behavior and Failure of Threaded Elements,” J. Fail. Anal. Prev., 12(5), pp. 541–549.

[176] Mohammadzadeh, A. R., and Haidar, S. M., 2022, “Thermo-Mechanical Stresses in the Design and Analysis of Thick-Walled Pressure Vessels,” ASME Paper No. IMECE2021-66582

[177] ASME, 2019, SECTION VIII ASME Boiler and Pressure Vessel Code - Division 1, ASME, New York

MODULO DI EMBARGO DELLA TESI
(da compilare solo se si richiede un periodo di segretazione della tesi)

La sottoscritta PUTELLI LORENZA,
nata il 6 OTTOBRE 1994, a ISEO provincia di BRESCIA
Dottorato di Ricerca in INGEGNERIA MECCANICA E INDUSTRIALE

DICHIARA

- che il contenuto della tesi **non può essere immediatamente consultabile per il seguente motivo**
BREVETTO

La motivazione deve essere dettagliata e controfirmata obbligatoriamente dal Primo Supervisore di tesi (Brevetto, segreto industriale, motivi di priorità nella ricerca, motivi editoriali, altro)

- che il testo completo della tesi potrà essere reso consultabile dopo:

□ 6 mesi dalla data di conseguimento titolo
☑ 12 mesi dalla data di conseguimento titolo

- che sarà comunque consultabile immediatamente l'abstract della tesi, che viene caricato in Esse3, profilo studente.

Luogo e Data 14/11/2023

Firma del Dichiarante

Lorenza Putelli

Controfirma del Primo Supervisore di tesi per la motivazione di embargo e il periodo.